NORTHWESTERN UNIVERSITY

Coupled Quantum, Molecular, and Continuum Studies of Graphitic Nanofracture

A DISSERTATION

SUBMITTED TO THE GRADUATE SCHOOL

IN PARTIAL FULFILLMENT OF THE REQUIREMENTS

for the degree

DOCTOR OF PHILOSOPHY

Field of Mechanical Engineering

By

Roopam Khare

EVANSTON, ILLINOIS

June 2008

ABSTRACT

Coupled Quantum, Molecular, and Continuum Studies of Graphitic Nanofracture

Roopam Khare

We present several multiscale quantum mechanical (QM), molecular mechanical (MM), and continuum mechanical (CM) schemes to study the strength properties of carbon nanotubes (CNTs) and graphene sheets. A bridging domain method based on overlapping domain-decomposition schemes using the Lagrange multipliers field is developed to couple an atomistic domain with a finite element domain. The ONIOM is used to couple the quantum mechanical model with the molecular mechanical model. We have also developed a minimal overlap QM/MM coupling scheme, where the part of the region that is treated by quantum mechanics does not require MM calculations, which makes the method suitable for systems containing localized regions that cannot be modeled by available empirical potentials. This method is called quantum to molecular mechanical overlapping domain (QtMMOD) method.

In these methods, we have scaled the MM potential by a scaling factor which depends on the applied strain and matches the MM energy to the QM energy to avoid certain unphysical behavior and match the QM and MM models more closely. Fracture properties of CNTs with large defects have been calculated and it is suggested that these large defects were the reason behind the low experimental strengths of CNTs. It was found that even at nanoscale, the fracture strengths of materials decrease as the flaw size increases and agree relatively well with the Griffith theory. We have also developed an extended-finite element method for studying dislocation motion in CNTs to model the super-plasticity phenomenon observed experimentally at high strain and temperatures.

Acknowledgements

It is a great pleasure for me to thank many people who have helped me during my PhD and even before that.

First and foremost I would like to thank my advisor Professor Belytschko, whose continuous encouragement, enthusiasm and inspiration had me going for last four and a half years. Even with his busy schedule, he always gave me enough time to go through my research problems, whether I am stuck somewhere or in coming up with new ideas for a project and I can not thank him enough for that.

I would like to thank Dr. Sulin Zhang, who during his pos-doctoral research here at Northwestern taught me all his codes and concepts of molecular dynamics. I would like to thank Dr. Steven Mielke and Dr. Jeffrey Paci from Chemistry department for teaching me the fundamentals of Quantum Chemistry and helping me in all the relating problems.

I would like to thank all my colleagues in our group. We have a great atmosphere in our research group and all the labmates have been very helpful. I would like to thank Dr. Chandu Parimi, who was like my mentor. I would like to thank all the previous colleagues: Dr. Harold Park, Dr. Joe Block, Dr. Cahal McVeigh, Dr. Yaling Liu, Dr. Qiang Lu and the current ones: Dr. Hongwu Wang, David Ferrell, Robert Gracie, Jeong

Song, Mei Xu, Jay Oswald, Adrian Kopacz, etc. for making the research work fun with their company.

I would like to thank all my friends here who have made the non-academic life fun for me. A very special thanks to Supinda Watcharotone who has been a great company for last three years. My roommate for last four and a half years, Manish Agarwal, has been a great friend of mine. I have made a few other special friends: Deepak, Ravindra, Ravi, Robin, Sabrina, Aniket, Sayantan and Anup.

I would like to thank the committee members to be part of my thesis examination. I would like to thank all the staff in the ME department for helping me in many ways.

I want to thank all of my family members for always being there for me and for supporting all my decisions.

I gratefully acknowledge the grant support from the NASA University Research, Engineering and Technology Institute on Bio Inspired Materials (BIMat) under award No. NCC-1-02037 and the support of the Army Research Office under Grant No. W911NF-0510049.

Table of Contents

List of Tables

List of Figures

CHAPTER 1

Introduction

Since their discovery by Iijima [1], carbon nanotubes (CNTs) have generated great interest due to their exceptional properties. Their excellent mechanical [2, 3, 4], chemical [5, 6], electrical [7, 8, 9] and thermal [5, 10, 11] properties offer exciting possibilities in various applications.

CNTs are single molecules without any grain boundaries, which makes them interesting for the study of fracture as it involves only bond breaking. We have studied the fracture behavior of CNTs, both brittle and plastic, containing defects such as holes, slits and dislocations. We have made similar studies on graphene sheets, which possess similar bonding and properties as CNTs and are more convenient to model.

We have developed coupled quantum mechanics (QM), molecular mechanics (MM), and continuum mechanics (CM) methods to study the strength of CNTs and graphene sheets, particularly with defects. A single method is not sufficient to estimate the mechanical properties of systems with large defects. The MM and CM methods are computationally cheap but do not predict the bond breaking phenomenon correctly [4, 12, 13]. QM electronic structure calculations are very accurate but are computationally very expensive. A large system is required for the study of defected materials, because a defect influences the electronic structure and the mechanical response over a large neighborhood.

In the multiscale schemes, the more accurate methods (QM or MM) are used over the defected region and the faster methods (MM or CM) are applied in the rest of the system.

In the following, some of the literature on multiscale coupling methods is briefly reviewed. More methods are given in the introduction of the chapters. Then the chapters are summarized.

Substantial previous work has been done in multiscale MM/CM models. Abraham et al. [14] and Rudd and Broughton [15] developed the concurrent coupled length scale methods to couple finite element, molecular dynamics and tight binding models, based on "handshake" domain methods. In the handshake domain the energy is equipartitioned among the overlapping models; however, the treatment of the constraints, which was not described, includes a coupling energy. Xiao and Belytschko [16], in their development of the bridging domain method, showed that if the coupling is by a Lagrange multiplier method, then the corresponding coupling energy must vanish. Xu and Belytschko [17] have shown that the energy and the momentum are conserved in the bridging domain method. E et al. [18] used heterogeneous multiscale methods to couple atomistic and continuum length scales, where continuum is solved first and the required continuum information such as the constitutive laws is obtained by performing local simulations of the atomistic models by constraining them to be compatible with the local continuum state of the system. Liu and coworkers used a two-scale decomposition of displacements in the bridging scale method [19, 20]. The method coupling atomistic and discrete dislocation plasticity [21] and the homogenization [22] technique are some other methods developed

recently. Differences in the available coupling methods are the specifics of the coupling strategies, which have been extensively reviewed elsewhere [23, 24, 25].

Most of these models are applicable only to dynamics studies. In a pioneering work on coupling static equilibrium MM and CM models, Tadmor et al. [26] developed a quasicontinuum method for static calculations where compatibility between the coarse scale model and fine scale model is obtained by selective representation of atomic degrees of freedom. The energy of representative atom is calculated either by empirical potentials or a local approximation such as the Cauchy-Born rule. The density of these representative atom is varied in a continuous fashion from the fine scale to the coarse scale model. However when coupling a finite element mesh with a discrete lattice it is required that the finite element nodes match the lattice structure in the transition region, which is inconvenient.

The bridging domain method of Xiao and Belytschko [16] was extended [27] (this work is part of the thesis) for static equilibrium calculations that couples the atomistic models with the continuum mechanics models using Lagrange multipliers. An efficient version of the method is developed for cases where the continuum can be modeled as a linear elastic material and thus augmented Lagrange multiplier scheme is not required to obtain the stationary point of the energy [16]. In this method, the finite element mesh is present everywhere and the discrete atomic lattice is only used in important regions. The double counting of energy is avoided by use of proper weight functions. The method

does not require finite element nodes to match the atomic lattice in the coupling region, unlike the quasicontinuum methods [26, 28].

The QM/MM coupling methods can be broadly classified into two classes based on their treatment of boundary atoms: the link atoms based methods [29, 30, 31, 32, 33, 34, 35, 36] and the hybrid orbitals methods [37, 38, 39, 40, 41, 42, 43, 44]. The main difficulty in implementation of any QM/MM method appears when the QM/MM boundary separating QM and MM regions cuts covalent bonds between atoms and various methods differ in their treatment of boundary atoms.

In the hybrid orbital methods, the bonds between QM and MM fragment atoms are essentially represented by localized bond orbitals. Thery et al. [37] proposed a local-self consistent field (LSCF) method to treat the QM/MM boundary using a hybrid orbital technique where the boundary atoms of the QM fragment, called frontier atoms, are assumed to have only s and p orbitals in their valence shell. The two electrons of the covalent bond across the boundary are represented by a linear combination of two hybrid orbitals, each defined on both atoms involved in the bond. The molecular orbitals of the electrons of the quantum fragment are then built with these atomic orbitals. Gao et al. [39] developed a generalized hybrid orbital (GHO) method, which does not need to be reparametrized every time a new system is studied unlike the LSCF method. In this method two sets of hybrid orbitals are used as basis functions on the boundary atoms of the MM fragment and only one set is optimized with all the other atomic orbitals of the QM fragment in the SCF calculations, thus avoiding the calculations of

any parameters for every new system. Other hybrid orbital methods to be mentioned are [38, 40, 41, 42, 43, 44].

In the link atom method, which we use here, the valencies of the boundary QM fragment atoms are satisfied by adding hydrogen atoms, which are called link atoms. The link atoms may also be pseudo-halogen atoms as in the HYPERCHEM software to mimic the properties of removed MM fragment atom. Roughly speaking link-atom methods differ in the following aspects: a) whether the link atom is geometrically optimized, b) whether the link atom is included in MM calculation or QM calculations and c) whether the hydrogen atoms or the halogen atoms are used as the link atoms.

Singh and Kollman [29] proposed a method of linking boundary QM fragment atoms with hydrogen atoms to satisfy their valencies. In this method, the entire molecule was first energy optimized by MM. The energy of the QM fragment with the valency satisfied by the hydrogen atoms was then calculated by holding the remaining atoms frozen. The MM energy was added to the QM energy and the combined energy was optimized to obtain the stable configuration. Another widely used link-atom based QM/MM method is IMOMM [30], where the coordinates of the MM fragment atoms bonded to the QM fragment atoms were written in terms of the pure QM atoms and the link atoms to reduce the number of degrees of freedom to be optimized. The total energy was written as the sum of the QM fragment energy and the MM energy of the entire molecule. In the Addremove link based QM/MM model [35], the position of the link atom is calculated based on the positions of real atoms involved in the bond without introducing any degrees

of freedom to the system. Das et al. [34] developed a double link atom method where an extra link atom was bonded to the MM fragment boundary atom, which was involved in all the electrostatic energy terms with the MM atoms, but the classically bonded terms involving the extra link atom and the QM atoms are excluded.

In chapter 2, we have developed the bridging domain method for static equilibrium calculations. The discrete equations are derived and an efficient algorithm for the linear elastic continuum models is described. The method is applied to calculate the energetics of CNTs and the fracture strengths of graphene sheets with defects and is compared to the pure MM calculations. A method for computing strain in atomistic models and handshake domains is formulated based on a moving least square approximation. The method gives exact constant strain for a linear displacement field when a linear basis is used. We also derive the virial stress expression for an empirical potential containing a three-atom pair terms. It is shown that the forces due to the angle bending term can be decomposed into two-atom terms, which allows the stress expression to be written in the standard virial stress form.

Applications of these methods to the fracture of defected single-layer atomic sheets and nanotubes are given. Strain and stress contours are calculated for a coupled model of graphene sheet with crack and results are compared to the elasticity solution.

In chapter 3, we have used a link-atom based coupled QM/MM method, ONIOM [32], to study the effects of large defects and cracks on the mechanical properties of carbon nanotubes and graphene sheets. ONIOM is a widely-used method for coupling in

QM/MM calculations due to its simplicity of implementation. It is a general framework that combines layers of computational methods of different levels of accuracy. The positions of the link atoms are calculated based on the interface atoms and they are not involved in the geometry optimization. The semi-empirical method PM3 is used to treat the QM subdomains and a Tersoff-Brenner potential is used for the molecular mechanics; some of the QM calculations are also done using density functional theory (DFT). The Tersoff-Brenner potential is scaled so that the modulus and overall stress-strain behavior of the QM and MM model matches quite closely, is also used to obtain meaningful coupled calculations of the mechanical properties.

In chapter 4, strategies for coupling QM, MM, and CM methods are described. For QM/MM coupling, we have developed a new minimal-overlap scheme denoted as the "quantum to molecular mechanical overlapping domain" (QtMMOD) method, where the part of the region that is treated by quantum mechanics does not require MM calculations, which makes the method suitable for systems containing localized regions that cannot be modeled by available empirical potentials. We describe how the QtMMOD method can in turn be coupled to a finite element model by the bridging domain method, another overlapping domain method, yielding a QM/MM/CM model. We also show how the QtMMOD scheme can be used to couple a finite element model directly with a QM model. These coupling methods are used to calculate the fracture properties of graphene sheets containing defects. An extension of an atomistic strain calculation method based on a

moving least squares scheme, which is applicable to the treatment of material interfaces, is given.

Chapter 5 presents a study of dislocations in CNTs using extended finite element method (XFEM). In XFEM [45, 46, 47] the finite element displacement field is enriched based on a known local feature solution of the given problem under local partition of unity framework [48]. Problems such as crack propagation [45, 47], shear band [49], two phase flows [50] etc. have been modeled using XFEM without the requirement of remeshing [45, 46, 47].

In a continuum framework, dislocation problems are usually studied based on the superposition of infinite domain solutions [51, 52, 53], which limits these models to small strains and makes applications to shells difficult. Moreover the linear anisotropic models are computationally untractable due to lack of a Green's function. We have used a new technique of using XFEM for dislocations, which was recently developed [54, 55, 56] for two dimensional models. We have implemented this method for thin cylindrical shells based on Kirchhoff-Love theory for modeling CNTs. The energetics of dislocation climb and glide are compared to molecular mechanics simulations of nanotubes using a modified Tersoff-Brenner potential.

In chapter 6 the main conclusions of the thesis are given.

CHAPTER 2

A bridging domain and strain computation method for coupled atomistic–continuum modeling of solids

2.1. Introduction

Modeling of material failure often involves phenomena simultaneously occurring at multiple length scales. On the one hand, such behavior cannot be described by continuum mechanics without resorting to phenomenological descriptions since fracture is intrinsically a bond breaking phenomenon. On the other hand, computational costs limit atomistic simulations to small subdomains relative to realistic specimens, even for specimens such as nanotubes and nanorods. It is thus desirable to develop multiscale material modeling approaches coupling continuum and atomistic models.

Extensive work has been done in the development of multiscale modeling approaches for linking atomistic with macroscopic models. Among them are the coupled length scale method [15, 14], the bridging method [19, 20], the bridging-domain method [57, 16], the method coupling atomistic and discrete dislocation plasticity [21], and homogenization methods [22]. Despite different treatments in the coupling strategy, these methods share basic principles, and typically have three components: a finite element

representation for continuum subdomains where the deformation field is smooth and homogeneous; a molecular mechanics/dynamics description for atomistic subdomains in which bond breaking is expected; a strategy to couple these two representations. Differences in the available coupling methods are the specifics of the coupling strategies, which have been extensively reviewed elsewhere [23, 24, 25].

We here present extensions of the bridging-domain method of Belytschko and Xiao [57] and an analysis of some of its properties. We have developed an algorithm for the finding the stationary point of the total energy of the system when the continuum response is linear, which is faster than the augmented Lagrange scheme used in [57]. Dhia et al.[58] originated this method for the purpose of joining finite element meshes and called it the Arlequin method. These methods are essentially overlapping domain decomposition methods; they are called "handshake" methods in [14], but in these original methods the coupling in the handshake domain was rather ad hoc, so it is unclear how continuity was enforced between subdomains.

For many nanoscale fracture problems, a large portion of the computational domain undergoes homogeneous deformation, and bond forming/breaking takes place only within a small subdomain. The primary function of the continuum domain is to provide the appropriate boundary conditions for the atomistic subdomain and to suppress the surface effects. The aim of the proposed multiscale method is to solve coupled molecular mechanics/continuum mechanics efficiently. This method offers atomistic resolution of

deformation in subdomains encompassing defects such as vacancies, interstitials, dislocations, and crack tips, and treats the remainder of the domain with crystal elasticity. Displacement compatibility conditions are imposed in the overlapping subdomain by the Lagrange multiplier method. The resulting governing equations are coupled through the internal forces corresponding to Lagrange multipliers. The governing equations can further be simplified provided that the continuum subdomain is linear elastic. This method matches the corresponding results of a fully atomistic model with reasonable accuracy, and greatly reduces the computational cost.

A nice feature of the method is that it does not require the finite element mesh to match the lattice spacing of the atomic model. Thus, it is easy to link various atomistic models, even models of amorphous solids, with finite element models. Furthermore, the approach allows finite element models to be replaced by atomistic models wherever it is needed by zeroing the material properties of the target subdomain of finite element mesh and overlaying the atomistic model on the desired subdomain.

Although the methodology is simple in principle, several issues in the implementation needed to be addressed. The one that is considered here is the relationship of the atomistic model discretization to the continuum discretization. It shall be seen that certain restrictions must be imposed on the element size relative to the lattice spacing. This issue is discussed in section 2.2.

In addition, a method is presented for obtaining continuous strain fields for discrete atomistic models. So called "atomistic strains" have previously been developed by Mott

et al. [59] based on Voronoi tessellations, but they were only defined at the positions of nuclei. Here we employ a moving least square (MLS) approximation to compute the atomistic strain. It is shown that this method gives the exact constant strain when the nuclear positions are specified by a linear displacement field.

We also derive the virial stress expression for an empirical potential containing a three-body or angle bending term. It is shown that the forces arising due to the angle bending term can be decomposed into two-atom terms, which allows us to write the stress expression in the standard virial stress form.

The chapter is organized as follows. Section 2.2 describes the MM/CM coupling scheme. In particular, discrete equations are obtained and an algorithm for solving these equations is developed. The MLS strain formulation and the virial stress derivation for empirical potentials with two-atom and three-atom pair terms are given in Section 2.3. In Section 2.4, numerical examples are given. Fracture stresses are calculated using the coupled scheme and the MM method for a graphene sheet containing vacancy defects. Stress and strain contours are calculated for a graphene sheet with a crack and results are compared to the elasticity solution. Energy and stress of a coupled model for a CNT are also calculated as the applied strain is varied and compared to the MM calculations. Conclusions are given in section 2.5.

2.2. Method

The coupled method consists of three components: the atomistic model, the continuum model, and the coupling strategy. Both the atomistic and continuum framework we adopt here are taken from the literature. Therefore, we will focus on the coupling of the two models, which is described in the following subsections. For clarity, we use Greek indices (α, β, γ) to denote atoms, capital indices (I, J, K) to denote the finite element nodes, and lower-case indices (i, j, k) to denote the components of vectors and tensors.

2.2.1. Coupling

Consider a solid body subjected to prescribed traction $\bar{\mathbf{t}}^0$ on the undeformed surface Γ_0^{t}, and prescribed displacement $\bar{\mathbf{u}}$ on Γ_0^{u}. The entire domain is decomposed into three subdomains: an atomistic subdomain Ω_0^{A} ; a continuum subdomain, Ω_0^{C}, and the overlapping subdomain, $\Omega_0^{\mathrm{H}} = \Omega_0^{\mathrm{A}} \cap \Omega_0^{\mathrm{C}}$, where the atomistic and continuum models overlap, which is frequently called the handshake domain. The superscripts "C" (continuum) and "A" (atomistic) identify the associated variables. We assume that Γ_0^{t} is restricted to the boundary of the continuum subdomain and the atomistic subdomain is traction free. Under external loading, each material point $\mathbf{X} \in \Omega_0^{\mathrm{C}}$ in the initial, undeformed configuration moves to its current position $\mathbf{x}$ according to a deformation map: $\mathbf{x} = \boldsymbol{\phi}(\mathbf{X}, t)$. The initial position of atom α is denoted by $\mathbf{X}_\alpha$, and its current position is denoted by $\mathbf{x}_\alpha$. The total free energy (E_{total}) is sum of the strain energy of the continuum subdomain (E_{CM}), and the potential energy of atomistic subdomain (E_{MM}), minus the external work (E_{ext}) on

both subdomains:

$$E_{\text{total}} = E_{\text{MM}} + E_{\text{CM}} - E_{\text{ext}}, \tag{2.1}$$

where

$$E_{\text{MM}} = \sum_{\alpha \in \Omega_0^{\text{A}}} \left[\sum_{\beta > \alpha} w^{\text{A}} \left(\frac{1}{2}(\mathbf{X}_\alpha + \mathbf{X}_\beta) \right) V_{\alpha\beta} \right], \tag{2.2}$$

$$E_{\text{CM}} = \int_{\Omega_0^{\text{C}}} w^{\text{C}}(\mathbf{X}) W(\mathbf{F}(\boldsymbol{\phi}(\mathbf{X}))) \mathrm{d}\Omega_0, \tag{2.3}$$

and

$$E_{\text{ext}} = \int_{\partial\Omega_{\text{t}}^{\text{C}}} w^{\text{C}}(\mathbf{X}) \bar{\mathbf{t}}^0 \cdot \mathbf{u} \mathrm{d}\Gamma_0. \tag{2.4}$$

In the above expressions, $V_{\alpha\beta}$ is the atomistic interaction potential between atoms α and β, W is the strain-energy density function, $\partial\Omega_{\text{t}}^{\text{C}}$ is the portion of the boundary of Ω_0^{C} where the traction $\bar{\mathbf{t}}^0$ is applied, $\mathbf{u} = \boldsymbol{\phi} - \mathbf{X}$ is the displacement vector, and $\mathbf{F}$ is the deformation tensor given by

$$\mathbf{F} = \frac{\partial \boldsymbol{\phi}}{\partial \mathbf{X}} = \mathbf{I} + \frac{\partial \mathbf{u}}{\partial \mathbf{X}}, \tag{2.5}$$

and $\mathbf{I}$ is the identity tensor. It should be noted that, in order to avoid double counting the the atomistic and the continuum energies in the handshake domain, these energy terms are weighted based on the positions at which these values are evaluated. The weight functions, w^{C} and w^{A}, vary linearly across the handshake domain

$$w^{\mathrm{C}}(\mathbf{X}) = 1 - w^{\mathrm{A}}(\mathbf{X}) = \begin{cases} 1 & : \quad \mathbf{X} \in \Omega_0^{\mathrm{C}} \backslash \Omega_0^{\mathrm{H}}, \\ \|\mathbf{X} - \mathbf{X}_{\mathrm{B}}\|/L & : \quad \mathbf{X} \in \Omega_0^{\mathrm{H}}, \\ 0 & : \quad \mathbf{X} \in \Omega_0^{\mathrm{A}} \backslash \Omega_0^{\mathrm{H}}. \end{cases} \tag{2.6}$$

We assume that the atomistic domain is convex and sufficiently regular so that the parameter w^{C} can be uniquely determined by the nearest point projection of $\mathbf{X}$ onto the boundary of Ω_0^{C}, denoted by $\mathbf{X}_{\mathrm{B}}$. The variable L is the distance between the inner and outer boundaries of the handshake domain along the vector $\mathbf{X} - \mathbf{X}_{\mathrm{B}}$. The boundary $\partial\Omega_{\mathrm{t}}^{\mathrm{C}}$ that is overlapped by the atomistic model is a traction-free boundary ($\bar{\mathbf{t}} = 0$).

Coupling of the atomistic and continuum models is achieved by approximately enforcing compatibility in the handshake domain by Lagrange multipliers, so the total energy functional is

$$\Pi = E_{\mathrm{total}} + \sum_{\alpha \in \Omega_0^{\mathrm{H}}} \int_{\Omega_0} \boldsymbol{\lambda}(\mathbf{X}) \cdot [\boldsymbol{\phi}(\mathbf{X}) - \mathbf{x}_\alpha] \, \delta(\mathbf{X} - \mathbf{X}_\alpha) \mathrm{d}\Omega_0, \tag{2.7}$$

where $\boldsymbol{\lambda}$ is the vector of Lagrange multipliers that enforce the constraints and $\delta(\mathbf{X} - \mathbf{X}_\alpha)$ is Dirac delta function. We leave the above in an integral form because the Lagrange multipliers will be approximated by fields.

Equation (2.7) can be written in the following form, which is generally adopted in so called "handshake" methods[14, 23],

$$E = E_{\text{total}} + E_{\text{MM/CM}}, \tag{2.8}$$

where $E_{\text{MM/CM}}$ is a coupling energy that corresponds to the second term in Eq. (2.7). Note that by the well-known property of constrained minimization problems, the Lagrange multiplier term vanishes at the stationary point, so the coupling energy vanishes provided that the constraints are enforced exactly. In the method described here, the constraints are usually not satisfied exactly because as will be seen, we use an approximate Lagrange multiplier field rather than discrete multipliers. This gives rise to a residual interaction energy in the overlapping domain. The equilibrium configuration of the coupled model is obtained by determining the stationary point of the total energy functional Π in terms of $\boldsymbol{\phi}$, $\mathbf{x}_\alpha$, and $\boldsymbol{\lambda}$, as will be detailed in the next section.

2.2.2. Numerical Implementation

The continuum domain is discretized by approximating the continuum deformation field and the Lagrange multiplier field by finite element interpolants with *nel* elements. Each element is mapped from the undeformed configuration to the current configuration

through $\boldsymbol{\phi}^e$. The deformed configuration for element e is expressed by

$$\boldsymbol{\phi}^e(\mathbf{X}) = \sum_I N_I(\mathbf{X})\boldsymbol{\phi}_I, \tag{2.9}$$

where $N_I(\mathbf{X})$ is the nodal shape function of node I, and $\boldsymbol{\phi}_I$ denotes the current nodal position. Similarly, the Lagrange multiplier field in the handshake domain is approximated by *mel* elements, with

$$\boldsymbol{\lambda}^e = \sum_J N_J^{\lambda}(\mathbf{X})\boldsymbol{\lambda}_J, \tag{2.10}$$

where $N_J^{\lambda}(\mathbf{X})$ is the shape function of the Lagrange multiplier field, and $\boldsymbol{\lambda}_J$ is the nodal value. Substituting the above equations to Eq. (2.7) yields the discretized energy

$$\begin{aligned}\Pi = &\sum_{\alpha\in\Omega_0^{\mathrm{A}}}\left[\sum_{\beta>\alpha} w^{\mathrm{A}}\left(\frac{1}{2}(\mathbf{X}_\alpha+\mathbf{X}_\beta)\right)V_{\alpha\beta}\right] + \int_{\Omega_0^{\mathrm{C}}} w^{\mathrm{C}}(\mathbf{X})W(\mathbf{F}(\boldsymbol{\phi}))\mathrm{d}\Omega_0 \\ &- \int_{\partial\Omega_{\mathrm{t}}^{\mathrm{C}}} w^{\mathrm{C}}(\mathbf{X})\bar{\mathbf{t}}\cdot\mathbf{u}\mathrm{d}\Gamma_0 + \sum_{\alpha\in\Omega_0^{\mathrm{H}}}\sum_J N_J^{\lambda}(\mathbf{X}_\alpha)\boldsymbol{\lambda}_J\cdot\left[\sum_I N_I(\mathbf{X}_\alpha)\boldsymbol{\phi}_I - \mathbf{x}_\alpha\right].\end{aligned} \tag{2.11}$$

Taking derivatives of the function with respect to $\mathbf{x}_\alpha$, $\boldsymbol{\lambda}_{\mathrm{J}}$, and $\boldsymbol{\phi}_{\mathrm{I}}$ yields the stationary condition for Π, which correspond to the equilibrium equations and the constraint:

$$\frac{\partial\Pi}{\partial\boldsymbol{\phi}_I} = 0, \quad I = 1\cdots n_{\mathrm{C}}, \tag{2.12}$$

$$\frac{\partial \Pi}{\partial \boldsymbol{\lambda}_J} = 0, \quad J = 1 \cdots n_\lambda, \tag{2.13}$$

$$\frac{\partial \Pi}{\partial \mathbf{x}_\alpha} = 0, \quad \alpha = 1 \cdots n_{\mathrm{A}}, \tag{2.14}$$

where n_{C} is the number of finite element nodes, n_λ is the number of Lagrange multiplier nodes, and n_{A} is the number of the atoms in the coupled system. The resulting equations are

$$\mathbf{f}_I^{\mathrm{int}} + \sum_{J=1}^{n_\lambda} \mathbf{G}_{JI} \boldsymbol{\lambda}_J = \mathbf{f}_I^{\mathrm{ext}}, \quad I = 1 \cdots n_{\mathrm{C}}, \tag{2.15}$$

$$\sum_{J=1}^{n_{\mathrm{C}}} \mathbf{G}_{IJ} \mathbf{u}_J = \mathbf{f}_I^{\lambda}, \tag{2.16}$$

$$\sum_{\alpha \in \Omega_0^{\mathrm{A}}} \left[\sum_{\beta > \alpha} w^{\mathrm{A}} \left(\frac{1}{2} (\mathbf{X}_\alpha + \mathbf{X}_\beta) \right) \frac{\partial V_{\alpha\beta}}{\partial \mathbf{x}_\alpha} \right] - \sum_{\alpha \in \Omega_0^{\mathrm{H}}} \sum_J N_J^\lambda (\mathbf{X}_\alpha) \boldsymbol{\lambda}_J = 0, \tag{2.17}$$

where

$$\mathbf{f}_I^{\mathrm{int}} = \int_{\Omega_0^{\mathrm{C}}} w^{\mathrm{C}}(\mathbf{X}) \frac{\partial W}{\partial \mathbf{F}} \frac{\partial \mathbf{F}}{\partial \boldsymbol{\phi}_I} \mathrm{d}\Omega_0^{\mathrm{C}}, \tag{2.18}$$

$$\mathbf{G}_{IJ} = \sum_{\alpha \in \Omega_0^{\mathrm{H}}} N_I^{\lambda}(\mathbf{X}_\alpha) N_J(\mathbf{X}_\alpha), \tag{2.19}$$

$$\mathbf{f}_I^{\mathrm{ext}} = \int_{\partial\Omega_{\mathrm{t}}^{\mathrm{C}}} w^{\mathrm{C}}(\mathbf{X}) N_I(\mathbf{X}) \bar{\mathbf{t}} \mathrm{d}\Gamma_0, \tag{2.20}$$

$$\mathbf{f}_I^{\lambda} = \sum_{\alpha \in \Omega_0^{\mathrm{H}}} N_I^{\lambda}(\mathbf{X}_\alpha) \mathbf{u}_\alpha. \tag{2.21}$$

where $\mathbf{u}_\alpha$ denotes the atomic displacement. The continuum forces can be expressed in terms of the first Piola-Kirchhoff stress $\mathbf{P}$ by noting that

$$\mathbf{P} = \frac{\partial W}{\partial \mathbf{F}}, \tag{2.22}$$

and that

$$\frac{\partial \mathbf{F}}{\partial \boldsymbol{\phi}_I} = \frac{\partial N_I}{\partial \mathbf{X}}, \tag{2.23}$$

which enables us to write Eq. (2.18) as

$$\mathbf{f}_I^{\mathrm{int}} = \int_{\Omega_0^{\mathrm{C}}} w^{\mathrm{C}}(\mathbf{X}) \mathbf{P} \frac{\partial N_I}{\partial \mathbf{X}} \mathrm{d}\Omega_0^{\mathrm{C}}. \tag{2.24}$$

If the corresponding continuum model remains linear, the solution of Eqs. (2.15) to (2.17) can be simplified. We consider the case where $N_I^{\lambda}(\mathbf{X}) = N_I(\mathbf{X})$ in Ω^{H}. Let $\mathbf{d}_{\mathrm{C}}$ be the continuum displacements in the subdomain exclusive of the handshake domain, $\mathbf{d}_{\mathrm{H}}$ the

continuum nodal displacements in the handshake domain, $\mathbf{d}_{\mathrm{A}}$ the atomic displacements, i.e.

$$\mathbf{d}_{\mathrm{C}} = \{\mathbf{u}_1, ..., \mathbf{u}_I, ..., \mathbf{u}_{n^{\mathrm{C}}}\}^{\mathrm{T}} \quad I \in \Omega_0^{\mathrm{C}} \setminus \Omega_0^{\mathrm{H}}, \tag{2.25}$$

$$\mathbf{d}_{\mathrm{H}} = \{\mathbf{u}_1, ..., \mathbf{u}_I, ..., \mathbf{u}_{n^{\mathrm{H}}}\}^{\mathrm{T}} \quad I \in \Omega_0^{\mathrm{H}}, \tag{2.26}$$

$$\boldsymbol{\lambda}^{\mathrm{T}} = [\boldsymbol{\lambda}_1, \cdots \boldsymbol{\lambda}_{n^{\mathrm{H}}}], \tag{2.27}$$

$$\mathbf{d}_{\mathrm{A}} = \{\mathbf{x}_1 - \mathbf{X}_1, ..., \mathbf{x}_\alpha - \mathbf{X}_\alpha, ..., \mathbf{x}_{n^{\mathrm{A}}} - \mathbf{X}_{n^{\mathrm{A}}}\}^{\mathrm{T}}. \tag{2.28}$$

For a linear continuum model, we can write

$$\mathbf{f}^{\mathrm{int}} = \begin{Bmatrix} \mathbf{f}^{\mathrm{C}} \\ \mathbf{f}^{\mathrm{H}} \end{Bmatrix} = \begin{bmatrix} \mathbf{K}_{\mathrm{C}} & \mathbf{K}_{\mathrm{CH}} \\ \mathbf{K}_{\mathrm{CH}}^{\mathrm{T}} & \mathbf{K}_{\mathrm{H}} \end{bmatrix} \begin{Bmatrix} \mathbf{d}_{\mathrm{C}} \\ \mathbf{d}_{\mathrm{H}} \end{Bmatrix}, \tag{2.29}$$

where $\mathbf{K}_{\mathrm{C}}$, $\mathbf{K}_{\mathrm{CH}}$ and $\mathbf{K}_{\mathrm{H}}$ are submatrices of the stiffness matrix $\mathbf{K}$ partitioned according to the partitioning of $\mathbf{d}$ (nodal displacement vector) into $\mathbf{d}_{\mathrm{C}}$ and $\mathbf{d}_{\mathrm{H}}$. Similary, $\mathbf{f}^{\mathrm{ext}}$ is partitioned into $\mathbf{f}_{\mathrm{C}}^{\mathrm{ext}}$ and $\mathbf{f}_{\mathrm{H}}^{\mathrm{ext}}$. We assume that there is no external force applied in handshake

region. In a the similar way $\mathbf{G}_{\mathrm{C}}$ and $\mathbf{G}_{\mathrm{H}}$ are obtained from $\mathbf{G}$, where $\mathbf{G}_{\mathrm{C}} = 0$. Thus the system of Eqs. (2.15-2.17) can be written as

$$\begin{bmatrix} \mathbf{K}_{\mathrm{C}} & \mathbf{K}_{\mathrm{CH}} & 0 & 0 \\ \mathbf{K}_{\mathrm{CH}}^{\mathrm{T}} & \mathbf{K}_{\mathrm{H}} & 0 & \mathbf{G}_{\mathrm{H}}^{\mathrm{T}} \\ 0 & 0 & 0 & \mathbf{G}_{\mathrm{A}}^{\mathrm{T}} \\ 0 & \mathbf{G}_{\mathrm{H}} & \mathbf{G}_{\mathrm{A}} & 0 \end{bmatrix} \begin{Bmatrix} \mathbf{d}_{\mathrm{C}} \\ \mathbf{d}_{\mathrm{H}} \\ \mathbf{d}_{\mathrm{A}} \\ \boldsymbol{\lambda} \end{Bmatrix} = \begin{Bmatrix} \mathbf{f}_{\mathrm{C}}^{\mathrm{ext}} \\ 0 \\ -\mathbf{f}_{\mathrm{A}}^{\mathrm{int}} \\ 0 \end{Bmatrix}, \tag{2.30}$$

where $\mathbf{G}_{\mathrm{A}_{J\alpha}} = -N_J^{\lambda}(\mathbf{X}_\alpha)$ and

$$\mathbf{f}_{\mathrm{A}}^{\mathrm{int}} = \sum_{\alpha \in \Omega_0^{\mathrm{A}}} \left[\sum_{\beta > \alpha} w^{\mathrm{A}} \left(\frac{1}{2}(\mathbf{X}_\alpha + \mathbf{X}_\beta) \right) \frac{\partial V_{\alpha\beta}}{\partial \mathbf{x}_\alpha} \right]. \tag{2.31}$$

The nodal displacements $\mathbf{d}_{\mathrm{H}}$ can be found from the Schur complement of $\mathbf{K}_{\mathrm{H}}$, denoted by $\bar{\mathbf{K}}_{\mathrm{H}}$. The result is obtained by a simple rearrangement of the first two rows of Eq. (2.30)

$$\mathbf{d}_{\mathrm{H}} = \bar{\mathbf{K}}_{\mathrm{H}}^{-1}(\mathbf{K}_{\mathrm{CH}}^{\mathrm{T}}\mathbf{K}_{\mathrm{C}}^{-1}\mathbf{f}_{\mathrm{C}}^{\mathrm{ext}} + \mathbf{G}_{\mathrm{H}}^{\mathrm{T}}\boldsymbol{\lambda}), \tag{2.32}$$

$$\bar{\mathbf{K}}_{\mathrm{H}} = \mathbf{K}_{\mathrm{CH}}^{\mathrm{T}}\mathbf{K}_{\mathrm{C}}^{-1}\mathbf{K}_{\mathrm{CH}} - \mathbf{K}_{\mathrm{H}}. \tag{2.33}$$

Nodal displacements $\mathbf{d}_{\mathrm{C}}$ can be found in terms of $\mathbf{d}_{\mathrm{H}}$, using first row of Eq. (2.30) which gives

$$\mathbf{d}_{\mathrm{C}} = \mathbf{K}_{\mathrm{C}}^{-1}(\mathbf{f}_{\mathrm{C}}^{\mathrm{ext}} - \mathbf{K}_{\mathrm{CH}}\mathbf{d}_{\mathrm{H}}). \tag{2.34}$$

Substituting Eq. (2.32) into the last row of Eq. (2.30) gives

$$\mathbf{A}\boldsymbol{\lambda} = \mathbf{f}^{\boldsymbol{\lambda}}, \tag{2.35}$$

where

$$\mathbf{A} = \mathbf{G}_{\mathrm{H}}\bar{\mathbf{K}}_{\mathrm{H}}^{-1}\mathbf{G}_{\mathrm{H}}^{\mathrm{T}}, \tag{2.36}$$

$$\mathbf{f}^{\lambda} = -(\mathbf{G}_{\mathrm{H}}\bar{\mathbf{K}}_{\mathrm{H}}^{-1}\mathbf{K}_{\mathrm{CH}}^{\mathrm{T}}\mathbf{K}_{\mathrm{C}}^{-1}\mathbf{f}_{\mathrm{C}}^{\mathrm{ext}} + \mathbf{G}_{\mathrm{A}}\mathbf{d}_{\mathrm{A}}). \tag{2.37}$$

For any given atomic configuration, $\{\mathbf{d}_{\mathrm{A}}\}$, $\mathbf{f}^{\lambda}$ can be calculated using Eq. (2.37). The Lagrange multipliers $\boldsymbol{\lambda}$, and hence the continuum displacement field $\mathbf{u}$ can be determined by Eqs. (2.35) and (2.34), respectively.

For the coupled system under consideration, due to the constraints of the Lagrange multipliers, the system is not positive definite anymore and the solution is a saddle point. This makes many iterative methods inappropriate. Here we use a quasi-Newton method

BFGS(Broyden-Fletcher-Goldfarb-Shanno) [60] to determine the stationary point. Since the atomistic domain is free of any displacement constraint, a floating-domain problem is encountered when the calculated internal forces $\boldsymbol{\lambda}$ are not self-balanced, i.e., in equilibrium, see Farhat et al. [61, 62]. To overcome this difficulty, the following iteration procedure is used.

(1) Guess $\mathbf{d}_{\mathrm{A}}^{n}$, for $n = 1$.

(2) Solve Eq. (2.35) for $\boldsymbol{\lambda}^{n}$.

(3) Update the finite element nodal positions using Eqs. (2.34).

(4) Search along the minimum direction of Π and update $\mathbf{d}_{\mathrm{A}}$ and Π.

(5) Check the convergence criterion $||\Pi^{n+1} - \Pi^{n}|| < \epsilon_{\Pi}$ and $||\partial\Pi/\partial\mathbf{d}_{\mathrm{A}}||_2 < \epsilon_d$. If both are satisfied, an adequate equilibrium configuration has been obtained, otherwise, repeat from step (2).

We determine next the sufficient conditions for the regularity of $\mathbf{A}$ when $N_I^{\lambda}(\mathbf{X}) = N_I(\mathbf{X})$. Note that the rank of matrix product is given by

$$\mathrm{rank}(\mathbf{A}) \leq \mathrm{rank}(\mathbf{G}_{\mathrm{H}})\mathrm{rank}(\bar{\mathbf{K}}_{\mathrm{H}}). \tag{2.38}$$

We assume that the stiffness matrix $\bar{\mathbf{K}}_{\mathrm{H}}$ is regular, since this is a standard property of finite elements. The matrix $\mathbf{G}_{\mathrm{H}}$ is assembled from element matrices $\mathbf{G}_{\mathrm{H}}^{\mathrm{e}}$ given by

Eq.(2.19), so

$$\mathbf{G}_{\mathrm{H}}^{\mathrm{e}} = \sum_{\alpha=1}^{n_{\alpha}^{\mathrm{e}}} \mathbf{N}^{\mathrm{T}}(\mathbf{X}_{\alpha})\mathbf{N}(\mathbf{X}_{\alpha}), \tag{2.39}$$

where n_{α}^{e} is the number of atoms in element e and $\mathbf{N} = [N_I]$. From the above, it follows that

$$(\mathbf{Z}_{\mathrm{e}})^{\mathrm{T}}\mathbf{G}_{\mathrm{H}}^{\mathrm{e}}\mathbf{Z}_{\mathrm{e}} \equiv \sum_{\alpha=1}^{n_{\alpha}^{\mathrm{e}}} \mathbf{Z}_I^e \mathbf{N}_I(\mathbf{X}_{\alpha})\mathbf{N}_J(\mathbf{X}_{\alpha})\mathbf{Z}_J^{\mathrm{e}} = \sum_{\alpha=1}^{n_{\alpha}^{\mathrm{e}}} \mathbf{Z}^2(\mathbf{X}_{\alpha}). \tag{2.40}$$

The above can vanish for $\mathbf{Z}^{\mathrm{e}} \neq 0$ only if there exists a $\mathbf{Z}^{\mathrm{e}}$ such that

$$\sum_{I=1}^{n_{\mathrm{N}}^{\mathrm{e}}} N_I(\mathbf{X}_{\alpha})\mathbf{Z}_I^{\mathrm{e}} = 0 \qquad \alpha = 1 \text{ to } n_{\alpha}^{\mathrm{e}}, \tag{2.41}$$

where $n_{\mathrm{N}}^{\mathrm{e}}$ is the number of nodes in element e. If $n_{\alpha}^{\mathrm{e}} \geq n_{\mathrm{N}}^{\mathrm{e}}$, this can occur only if the locations of the points are degenerate, e.g. for a set of collinear points in a triangular element. Therefore it follows that

$$(\mathbf{Z}_{\mathrm{e}})^{\mathrm{T}}\mathbf{G}_{\mathrm{H}}^{\mathrm{e}}\mathbf{Z}_{\mathrm{e}} > 0 \qquad \forall \mathbf{Z}_{\mathrm{e}} \neq 0. \tag{2.42}$$

Therefore, all eigenvalues of $\mathbf{G}_{\mathrm{H}}^{\mathrm{e}}$ must be positive and by the element eigenvalue inequality [63], the eigenvalues of $\mathbf{G}_{\mathrm{H}}$ are positive. Thus the rank must equal its dimension, and $\mathbf{A}$ must be regular.

Note that when the number of atoms in an element is less that the number of nodes or the positions of atoms are degenerate, the regularity of **A** is not ensured.

2.3. Stress and Strain in the Coupled System

In coupled continuum-molecular models based on overlapping decomposition methods, the stress and strain at the interface require careful definitions for consistency of the energy and smoothness. Mott el al. [59] used Voronoi tessellations to calculate strain field in the discrete lattice structure. Here we present a method for computing strain that provides a smooth strain field at the interface. We include both extensional and angle-bending terms. A method based on homogenization was recently presented by Chen and Fish [22].

The method is based on MLS approximation [64] of the displacement. In the MLS approximation, the displacement $\mathbf{u}(\mathbf{X})$ at any point $\mathbf{X}$ is approximated in the domain by

$$\mathbf{u}(\mathbf{X}) = \sum_{i=1}^{m} p_i(\mathbf{X})\mathbf{a}_i(\mathbf{X}), \tag{2.43}$$

where m is the number of terms in the basis $p_i(\mathbf{X})$ and $\mathbf{a}_i(\mathbf{X})$ are vector coefficients to be determined as described subsequently. The basis used here are polynomial so

$$[p_i(\mathbf{X})] = [1, X, Y] \qquad \text{for a linear basis,} \tag{2.44}$$

$$[p_i(\mathbf{X})] = [1, X, Y, X^2, XY, Y^2] \quad \text{for a quadratic basis,} \tag{2.45}$$

$$\mathbf{a}_i = [a_{1i}, a_{2i}] = [a_{xi}, a_{yi}]. \tag{2.46}$$

The coefficients $\mathbf{a}$ at any point $\mathbf{X}$ are found by minimizing the weighted L_2 norm $q(\mathbf{X})$ given by

$$q(\mathbf{X}) = \sum_{\alpha \epsilon S_{\mathbf{X}}} (p_i(\mathbf{X}_\alpha)\mathbf{a}_i(\mathbf{X}) - \mathbf{u}_\alpha)^{\mathrm{T}} w^{\mathrm{mls}}(\mathbf{X}_\alpha - \mathbf{X})(p_j(\mathbf{X}_\alpha)\mathbf{a}_j(\mathbf{X}) - \mathbf{u}_\alpha), \tag{2.47}$$

where a sum is implied over the repeated indices i and j, $w^{\mathrm{mls}}(\mathbf{X}_\alpha - \mathbf{X})$ is a weight function of compact support and $S_{\mathbf{X}}$ is the set of nodes within the support of $w^{\mathrm{mls}}(\mathbf{X}_\alpha - \mathbf{X})$. Various choices can be made for the weight functions (see [65]). We have chosen a cubic spline

$$w^{\mathrm{mls}}(r) = \begin{cases} \frac{2}{3} - 4r^2 + 4r^3 & \text{for } r \leq \frac{1}{2}, \\ \frac{4}{3} - 4r + 4r^2 - \frac{4}{3}r^3 & \text{for } \frac{1}{2} < r \leq 1, \\ 0 & \text{for } r > 1, \end{cases} \tag{2.48}$$

where $r = ||\mathbf{X} - \mathbf{X}_\alpha||/R_0$ and R_0 is the radius of the support circle centered at point $\mathbf{X}$. The radius of support depends on lattice constant; we have used $R_0 = 4l_0$, where l_0 is the equilibrium bond length (lattice constant).

The coefficients $\mathbf{a}_i(\mathbf{X})$ are found by minimizing $q(\mathbf{X})$ in Eq. (2.47), which can be accomplished by finding the stationary point of $q(\mathbf{X})$. To develop these equations, we first adopt the more compact notation $p_{i\alpha} \equiv p_i(\mathbf{X}_\alpha)$, $w_\alpha \equiv w^{\mathrm{mls}}(\mathbf{X} - \mathbf{X}_\alpha)$, so Eq. 2.47

becomes

$$q(\mathbf{X}) = \sum_{\alpha \epsilon \mathrm{S}_{\mathbf{X}}} (p_{i\alpha}\mathbf{a}_i - \mathbf{u}_\alpha)^{\mathrm{T}} w_\alpha (\mathbf{X}_\alpha - \mathbf{X})(p_{j\alpha}\mathbf{a}_j - \mathbf{u}_\alpha). \tag{2.49}$$

The stationary point of the above is then given by

$$0 = \frac{\partial q}{\partial \mathbf{a}_k} = \sum_{\alpha \epsilon \mathrm{S}_{\mathbf{X}}} p_{k\alpha} p_{j\alpha} w_\alpha \mathbf{a}_j - \sum_{\alpha \epsilon \mathrm{S}_{\mathbf{X}}} p_{k\alpha} w_\alpha \mathbf{u}_\alpha = 0, \tag{2.50}$$

which is a set of linear equations for $\mathbf{a}_j$. We note that the coefficient matrix of the left-hand side is the Gram matrix [66] M_{kj} (also called the moment matrix) given by

$$M_{kj} = \sum_{\alpha \epsilon \mathrm{S}_{\mathbf{X}}} p_{k\alpha} p_{j\alpha} w_\alpha. \tag{2.51}$$

If we define

$$\mathbf{b}_k = \sum_{\alpha \epsilon \mathrm{S}_{\mathbf{X}}} p_{k\alpha} w_\alpha \mathbf{u}_\alpha, \tag{2.52}$$

then Eq. (2.50) can be written as

$$M_{kj}\mathbf{a}_j = \mathbf{b}_k. \tag{2.53}$$

For a two dimensional problem with a linear polynomial basis, the above is two systems of three equations in three unknowns.

The deformation gradient is then given by using its definition in conjunction with Eqs. (2.43) and (2.44). For a linear basis

$$\mathbf{F} = F_{ij} = \begin{bmatrix} 1 + a_{x2} & a_{x3} \\ a_{y2} & 1 + a_{y3} \end{bmatrix}. \tag{2.54}$$

The Green strain can be computed by the standard formula

$$\mathbf{E} = \frac{1}{2}(\mathbf{F}^{\mathrm{T}}\mathbf{F} - \mathbf{I}). \tag{2.55}$$

A noteworthy attribute of the MLS strain is that for a linear displacement of the atoms, the MLS strain gives the correct constant strain state. This may be seen as follows. Suppose that the displacements of the atoms are given by

$$\mathbf{u}_\alpha = \mathbf{u}(\mathbf{X}_\alpha) = p_i(\mathbf{X}_\alpha)\bar{\mathbf{a}}_i. \tag{2.56}$$

Then substituting the above expression into the right hand side of Eq. (2.53) and using Eq. (2.52) gives

$$M_{kj}\mathbf{a}_j = \mathbf{b}_k = \sum_{\alpha \epsilon \mathrm{S}_{\mathbf{X}}} p_{k\alpha} w_\alpha p_{i\alpha} \bar{\mathbf{a}}_i. \tag{2.57}$$

By Eq. (2.51), the expression on right hand side of Eq. (2.57) is equal to $M_{ki}\bar{\mathbf{a}}_i$, so that $\mathbf{a}_i = \bar{\mathbf{a}}_i$ is followed. It can be followed from Eqs. (2.54) and (2.55) that $\mathbf{E}$ also has the correct value. This is often called a reproducing condition: the MLS strain reproduces the strain associated with any displacements of the atoms derived from a linear field. Similarly, the MLS strain will reproduce the correct strain for any atomic displacements corresponding to a quadratic field.

In the handshake domain, the strains are obtained by weighing the atomistic strains and the continuum strains according to the weights in the energetics, Thus

$$\mathbf{E}(\mathbf{X}) = w^{\mathrm{C}}(\mathbf{X})\mathbf{E}^{\mathrm{C}}(\mathbf{X}) + w^{\mathrm{A}}(\mathbf{X})\mathbf{E}^{\mathrm{A}}(\mathbf{X}). \tag{2.58}$$

The atomic stress is obtained in terms of doublets and triplets for the extensional and angle bending potentials; the nomenclature is shown in Fig. 2.1 (we depart temporarily from convention of Greek letters for atoms). The total potential W of the atomistic model is given by:

$$W = \sum_{\substack{i,j \\ i>j}} W_{\mathrm{E}}^{ij} + \sum_{\substack{i,j,k \\ i>j>k}} W_{\mathrm{B}}^{ijk}, \tag{2.59}$$

where W_{E}^{ij} is the extensional bond energy of the bond connecting atoms i and j and W_{B}^{ijk} is the bending energy of the triplet of atoms i, j and k

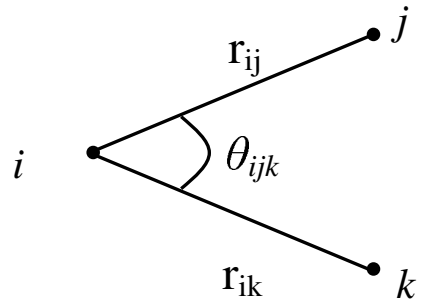

Figure 2.1. A triplet of atoms showing the bonds and bond angle.

For a hexagonal lattice, a representative unit cell consists of three inequivalent bonds and two inequivalent nuclei. The strain energy density of a representative unit cell can be written as

$$\overline{W} = \frac{1}{2\Omega_0^n}\left[\sum_{j\epsilon S^n} W_{\mathrm{E}}^{ij}(r^{ij}) + \frac{1}{2}\sum_{\substack{j,k\epsilon S^n \\ j\neq k}} W_{\mathrm{B}}^{ijk}(\theta^{ijk})\right], \tag{2.60}$$

where S_n is a set of nearest neighbors of atom i in the unit cell. In the above r^{ij} is the length of bond between atoms i and j and θ^{ijk} is the angle subtended between bonds $\overline{ij}$ and $\overline{ik}$. In a hexagonal planar lattice, $\Omega_0^n = 3\sqrt{3}r_0^2 t/4$ is the volume occupied by each atom in the unit cell, where r_0 is the bond length (lattice constant) in the unstressed configuration and $t = 3.4$ Å is nominal thickness of graphene sheet. Note that the factor half on the right hand side of the above equation appears due to the fact that the total energy is divided into two inequivalent nuclei. The other factor of half on the second term of the right hand side appears due to the double counting on the indices j and k.

Within the framework of hyperelasticity, the first Piola-Kirchhoff stress $\mathbf{P}$ can be written in terms of the continuum strain energy density W^{C} as

$$\mathbf{P} = \frac{\partial W^{\mathrm{C}}}{\partial \mathbf{F}} = \overline{W}_{,\mathbf{F}}\,, \tag{2.61}$$

The Cauchy stress $\boldsymbol{\sigma}$ will then be obtained by a standard transformation

$$\boldsymbol{\sigma} = \frac{1}{\det(\mathbf{F})}\mathbf{P}\mathbf{F}^{\mathrm{T}}. \tag{2.62}$$

The Cauchy-Born rule [67] gives the following relation for any lattice vector $\mathbf{r}$ in terms of its value in the unstressed configuration $\mathbf{r}_0$:

$$\mathbf{r} = \mathbf{F}\mathbf{r}_0. \tag{2.63}$$

Using (2.60), (2.61) and (2.63), we now develop expressions for $\mathbf{P}$ in terms of the extensional and bending potentials. For this purpose, we use a simplified notation $\mathbf{a} = \mathbf{r}^{ij}$ and $\mathbf{b} = \mathbf{r}^{ik}$. The extensional forces can be written as

$$\mathbf{f}_{\mathrm{E}}^{ij} = W_{\mathrm{E}}^{ij}{}_{,\mathbf{a}} = W_{\mathrm{E}}^{ij}{}_{,a}\, a_{\mathbf{a}} = f^{ij}\frac{\mathbf{a}}{a}, \tag{2.64}$$

where $f^{ij} = W_{\mathrm{E}}^{ij}{}_{,a}$; a is the length of the vector $\mathbf{a}$ and $\mathbf{a}/a$ is the unit vector that is collinear with that bond.

The angle bending forces are given by

$$\mathbf{f}_{\mathrm{B}}^{ij} = W_{\mathrm{B}}^{ijk}{}_{,\mathbf{a}} = W_{\mathrm{B}}^{ijk}{}_{,C}\, C_{,\mathbf{a}}\,, \tag{2.65}$$

$$\mathbf{f}_{\mathrm{B}}^{ik} = W_{\mathrm{B}}^{ijk}{}_{,\mathbf{b}} = W_{\mathrm{B}}^{ijk}{}_{,C}\, C_{,\mathbf{b}}\,, \tag{2.66}$$

where $C = \cos\theta$ and we have assumed the usual dependence of the angle bending potential on the cosine of the angle θ between the bonds. From the formula for the scalar product $ab\cos\theta = \mathbf{ab}$ it follows that

$$C_{,\mathbf{a}} = \frac{1}{ab}\left(\mathbf{b} - \frac{\mathbf{a}\cdot\mathbf{b}}{a^2}\mathbf{a}\right), \tag{2.67}$$

$$C_{,\mathbf{b}} = \frac{1}{ab}\left(\mathbf{a} - \frac{\mathbf{a}\cdot\mathbf{b}}{b^2}\mathbf{b}\right). \tag{2.68}$$

From (2.60), (2.61) and the chain rule we obtain

$$\mathbf{P} = \frac{1}{2\Omega_0^n}\left[\sum_{j\epsilon S^n} W_{\mathrm{E}}^{ij}{}_{,\mathbf{a}}\,\mathbf{a}_{,\mathbf{F}} + \frac{1}{2}\sum_{\substack{j,k\epsilon S^n \\ j\neq k}}\left(W_{\mathrm{B}}^{ijk}{}_{,\mathbf{a}}\,\mathbf{a}_{,\mathbf{F}} + W_{\mathrm{B}}^{ijk}{}_{,\mathbf{b}}\,\mathbf{b}_{,\mathbf{F}}\right)\right]. \tag{2.69}$$

From (2.63) it follows that

$$\mathbf{a}_{,\mathbf{F}} = \mathbf{I}\otimes\mathbf{a}_0, \mathbf{b}_{,\mathbf{F}} = \mathbf{I}\otimes\mathbf{b}_0. \tag{2.70}$$

Using (2.64-2.66), we can rewrite (2.69)as

$$\mathbf{P} = \frac{1}{2\Omega_0^n}[\sum_{j\epsilon S^n}\mathbf{f}_{\mathrm{E}}^{ij}\otimes\mathbf{a}_0 + \frac{1}{2}\sum_{\substack{j,k\epsilon S^n \\ j\neq k}}(\frac{1}{ab}W_{\mathrm{B}}^{ijk}{}_{,C}\,(\mathbf{b}-\frac{\mathbf{a}\cdot\mathbf{b}}{b^2}\mathbf{a})\otimes\mathbf{a}_0 + \frac{1}{ab}W_{\mathrm{B}}^{ijk}{}_{,C}\,(\mathbf{a}-\frac{\mathbf{a}\cdot\mathbf{b}}{a^2}\mathbf{b})\otimes\mathbf{b}_0)]. \tag{2.71}$$

Using Eqs. (2.62,2.65-2.68), and the transformation $\Omega^n = \Omega_0^n\det(\mathbf{F})$, where Ω^n is the volume occupied by atom in the representative unit cell in current configuration and replacing $\mathbf{a}$ by $\mathbf{r}^{ij}$, $\mathbf{b}$ by $\mathbf{r}^{ik}$

$$\boldsymbol{\sigma} = \frac{1}{2\Omega^n}\left[\sum_{j\epsilon S^n}\mathbf{f}_{\mathrm{E}}^{ij}\otimes\mathbf{r}^{ij} + \frac{1}{2}\sum_{\substack{j,k\epsilon S^n \\ j\neq k}}(\mathbf{f}_{\mathrm{B}}^{ij}\otimes\mathbf{r}^{ij} + \mathbf{f}_{\mathrm{B}}^{ik}\otimes\mathbf{r}^{ik})\right]. \tag{2.72}$$

The two terms in the second summation on the right hand-side of the above equation can be combined into one, as

$$\boldsymbol{\sigma} = \frac{1}{2\Omega^n}\left[\sum_{j\epsilon S^n} \mathbf{f}_{\mathrm{E}}^{ij} \otimes \mathbf{r}^{ij} + \sum_{j\epsilon S^n} \mathbf{f}_{\mathrm{B}}^{ij} \otimes \mathbf{r}^{ij}\right], \tag{2.73}$$

which can be seen as the standard virial stress form. As in the computation for the strain, a continuous stress field in the atomistic subdomain can be constructed using the MLS interpolation. The stress is computed by same weighting as the energetics in the handshake domain

$$\boldsymbol{\sigma}(\mathbf{X}) = w^{\mathrm{A}}(\mathbf{X})\boldsymbol{\sigma}^{\mathrm{A}}(\mathbf{X}) + w^{\mathrm{C}}(\mathbf{X})\boldsymbol{\sigma}^{\mathrm{C}}(\mathbf{X}). \tag{2.74}$$

2.4. Numerical Examples

In this section, several numerical examples are presented. Although the applicability of this method is not restricted to specific materials, we here choose graphene-like atomic sheets and carbon nanotubes as examples, because of their importance in engineering applications, as well as the simplicity of their atomic structures. To assess the performance of the coupled model, a full atomistic model corresponding to each example is solved independently, and compared with the coupled model.

2.4.1. Fracture Modeling of Atomic Graphene Sheet

Figure 2.2 shows a coupled model of an atomic sheet containing a double-vacancy defect in the center. We use a quadratic interatomic potential that consists of a pair-body term and an angle-bending term:

$$E = E_{\text{stretch}} + E_{\text{angle}}. \tag{2.75}$$

The pair-body term is piecewise quadratic, with

$$E_{\text{stretch}}(r) = \begin{cases} \frac{1}{2}k_{\text{a}}(r - r_0)^2 - \gamma & : \quad r < r_{\text{c}}, \\ \frac{1}{2}k_{\text{d}}(r - r_{\text{f}})^2 & : \quad r_{\text{c}} < r < r_{\text{f}}, \\ 0 & : \quad r > r_{\text{f}}, \end{cases} \tag{2.76}$$

where r_0 is the equilibrium distance, r_{c} and r_{f} are the bond lengths at which the interatomic force peaks and vanishes, respectively. The parameters k_{a} and k_{d} characterize the ascending and descending slopes of the force-separation curve, and γ is the potential energy when stretching the bond to infinite length. The parameters in the potential are chosen to ensure that the potential is piecewise continuous and differentiable. The interatomic force for this potential is then bilinear. The angle-bending term is of the following form:

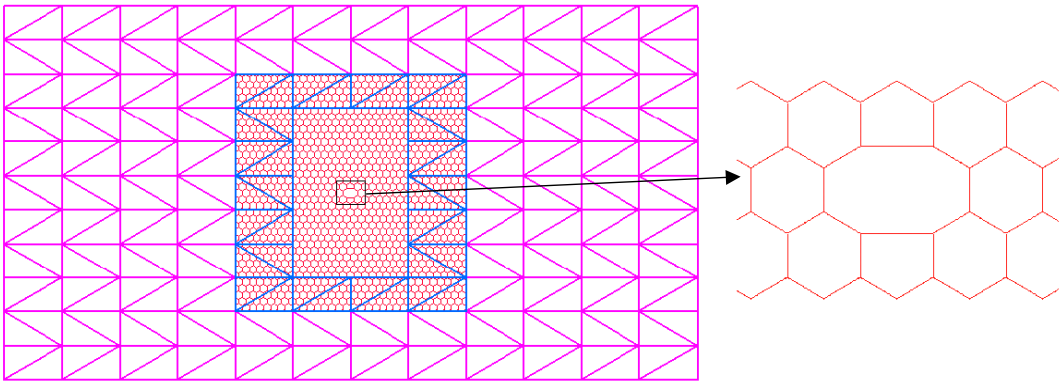

Figure 2.2. A coupled model of a graphene sheet containing a double-vacancy defect; a coarse model is shown for clarity.

$$E_{\text{angle}} = \frac{1}{2} k_\theta (\theta - \theta_0)^2 [1 + k_{sextile}(\theta - \theta_0)^4]. \tag{2.77}$$

Young's modulus and the Poisson's ratio can be then obtained through the Cauchy-Born rule [67]. Plane-stress is assumed for the one-atom-thick sheet. The full atomistic model is set up such that each atom in the atomistic subdomain of the coupled model coincides with an atom in the full atomistic model. We will use two error criteria

(1) ϵ_{G}, the global error which measures the difference between the complete atomistic model and the coupled model in the entire domain Ω.

(2) ϵ_{L}, the local error which measures the error in the atomistic subdomain Ω_0^{A} that is modeled by molecular mechanics.

Let $\mathbf{d}_{\text{A}}$ be the atomic displacements as computed by the full atomistic model and $\mathbf{d}_{\text{C}}$ the displacements at the atomic positions as computed by the coupled model. Then

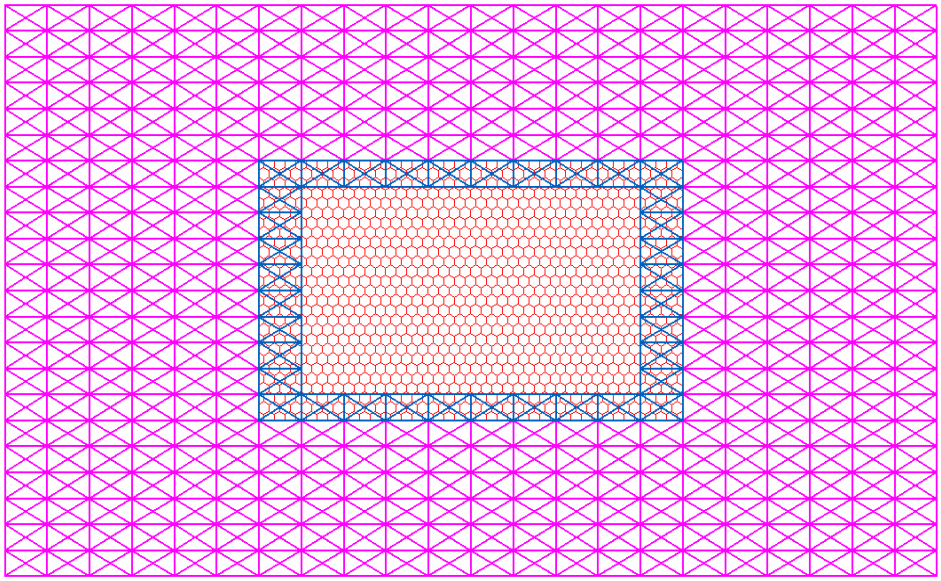

Figure 2.3. A coupled model of a graphene sheet used in patch test.

the global error is defined by

$$\epsilon_{\mathrm{G}} = \frac{\|\mathbf{d}_{\mathrm{C}} - \mathbf{d}_{\mathrm{A}}\|_2}{\|\mathbf{d}_{\mathrm{A}}\|_2}, \tag{2.78}$$

where

$$\|\mathbf{d}\|_2 = (\sum_i d_i^2)^{\frac{1}{2}}. \tag{2.79}$$

The local error is computed by taking the restrictions of $\mathbf{d}_{\mathrm{A}}$ and $\mathbf{d}_{\mathrm{C}}$ to the subdomain Ω_0^{A} (which are denoted by $\mathbf{d}_{\mathrm{AL}}$ and $\mathbf{d}_{\mathrm{CL}}$, respectively) and is given by

$$\epsilon_{\mathrm{L}} = \frac{\|\mathbf{d}_{\mathrm{CL}} - \mathbf{d}_{\mathrm{AL}}\|_2}{\|\mathbf{d}_{\mathrm{AL}}\|_2}. \tag{2.80}$$

To ensure the edge atoms in the overlapping subdomain at the continuum-atomistic interface are properly coordinated, several additional rows of atoms are introduced. These additional atoms are often called virtual atoms or pad atoms[68]. Because of the angle-bending term in the potential, the pad thickness must be slightly larger than the cutoff radius of the atomistic covalent interaction. During the simulation, the positions of the pad atoms are determined by the continuum deformation field through interpolation by the finite element nodal displacements.

As a measure of the effectiveness of the coupling, a patch test is performed by applying a linear displacement field to the outside boundaries of a coupled model. In particular we let

$$u_{XI} = a_{x1} + a_{x2}X_I + a_{x3}Y_I, \tag{2.81}$$

$$u_{YI} = a_{y1} + a_{y2}X_I + a_{y3}Y_I, \tag{2.82}$$

where a_{xi} and a_{yi} are arbitrary constants. According to Eq. (2.54), the deformation gradient should then be constant. The Green strain is computed by Eq. (2.55). This test is applicable to arbitrary materials as long as the continuum material properties are consistent with the atomistic potentials within the framework of the Cauchy-Born hypothesis.

In our studies of the patch test, we avoided some of the difficulties in matching nonlinear atomistics with continua by using a harmonic potential and a Kirchhoff material with small prescribed displacements. Specifically, we used $a_x = [0.5\ \ 0.02\ \ 0.02]$ and $a_y = [0.5\ \ 0.02\ \ 0.02]$. The error norm (2.78), with $\mathbf{d}_{\mathrm{A}}$ equal to the exact displacements by (2.81) and (2.82), was used to evaluate the performance of the method in the patch test.

The model is shown in Fig. 2.3; the ratio of the lattice constant r_{L} to the largest dimension of the elements in the overlapping subdomain h, $r_{\mathrm{L}}/h = 0.25$, the error ϵ_{L} equals to 0.2%, which is higher than expected. Most of the error comes from the handshake domain, where the strain differs as much as 1% from the prescribed value. In the atomistic domain, the maximum error in the strain is only 0.4%. This is adequate for most purposes, but indicates there is room for improvement in the method.

In the next example the size of the atomistic domain is varied while the size of the entire computational domain is fixed. Specifically, three sizes, small (39.3 Å$\times$ 22.7 Å), medium (98.4 Å$\times$ 56.8 Å), and large (157.4 Å$\times$ 90.9 Å) atomistic domains are considered. The global and critical-subdomain errors are computed at around 75% of the fracture strain. For each model, the sheet is stretched in the y-direction by prescribing displacements to the nodes (or the atoms for the full atomistic model) on the edges ($y = \pm h$). At each prescribed displacement, the system is relaxed to its equilibrium configuration, and the corresponding applied tensile force is calculated. In the simulations, $k_{\mathrm{a}} = 23.1$ nN/Å, $k_{\mathrm{d}} = -10.6$ nN/Å, $\gamma = 2.22$ eV, $r_0 = 1.42$ Å, $r_{\mathrm{c}} = 1.73$ Å, and $r_{\mathrm{f}} = 2.41$

Table 2.1. Results for the coupled model and the full atomistic model for the fracture of defected graphene sheets; σ_{frac} and ε_{frac} are the fracture stress and strain, respectively, ε_{G} and ε_{L} are the global and local errors as given in Eqs. (2.78) and (2.80), respectively.

Model	#atoms	# nodes	ε_{G}	ε_{L}	σ_{frac} (GPa)	ε_{frac}
Coupled model I	360	528	0.026	0.189	59.5	17.8
Coupled model II	2174	477	0.030	0.062	56.8	16.7
Coupled model III	5544	366	0.028	0.033	57.8	16.7
Fully atomistic	10440	0	0.000	0.000	57.6	16.8

Å. The resulting Young's modulus and Poisson's ratio for the continuum are 326.8 GPa and 0.167, respectively.

Table I summarizes the results obtained by the coupled model and the full atomistic model. In calculating the stress, the nominal thickness of 3.4 Å for graphene is used. Our simulations show that with increasing size of atomistic domain, the local error progressively decreases, while the global error remains of the same order of magnitude. Except for the coupled model with the smallest atomistic domain, the other two coupled models yield fracture stresses and strains very close to those of the full atomistic model. Running time for five steps of 0.1% strain increment varied from 33.7 seconds to 65.2 seconds from coupled model I to coupled model III, whereas fully atomistic model took 235.7 seconds for same amount of calculations.

We also studied the effects of finite element size on the accuracy of the computational results. An atomic sheet with dimensions of 393.52 Å$\times$ 227.20 Å is used for this study. The size of atomistic subdomain is 196.76 Å$\times$ 113.06 Å. In the simulations, four

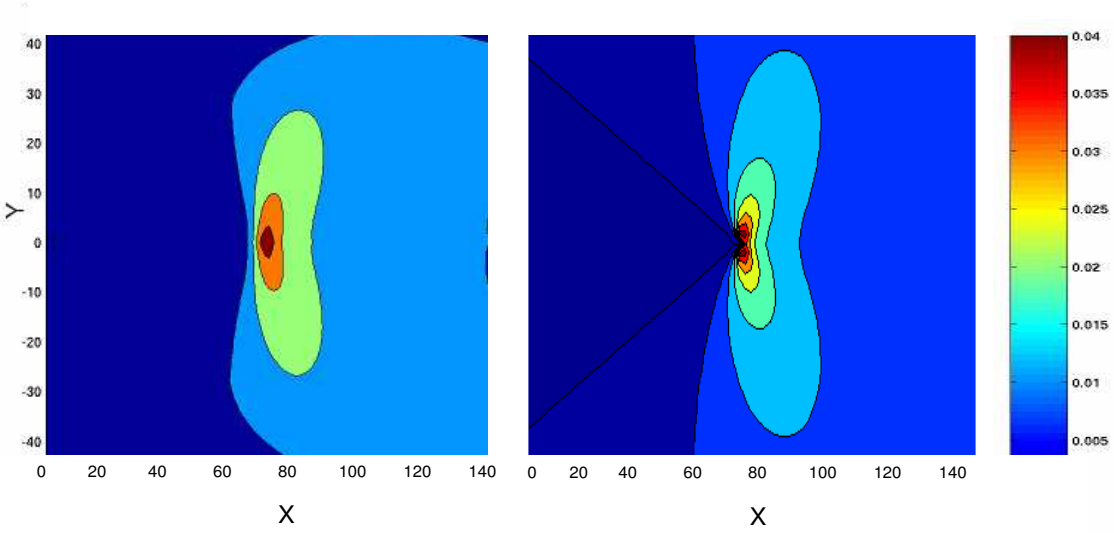

Figure 2.4. Contour of ϵ_{yy} around a crack tip for (a) coupling model (b)linear elastic solution.

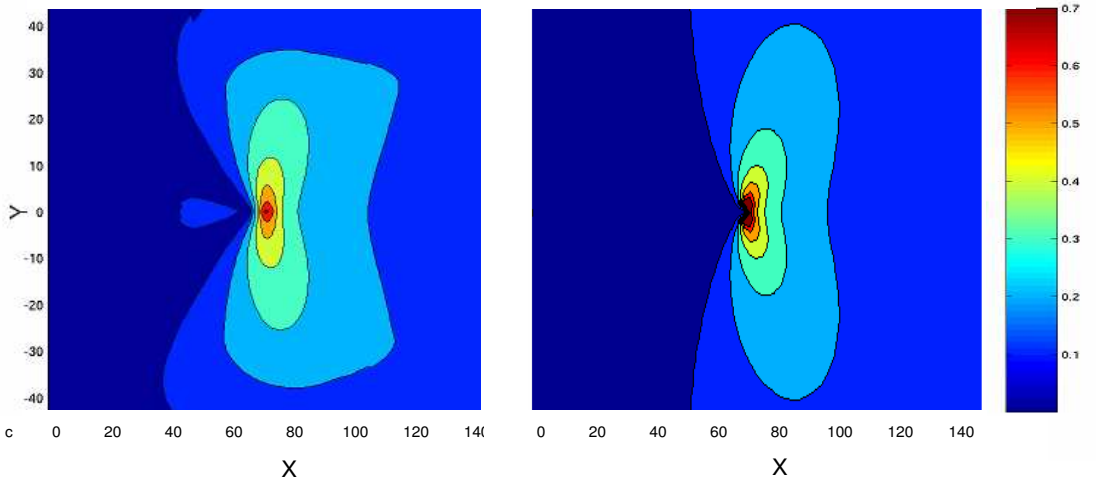

Figure 2.5. Contour of equivalent stress (in TPa) around a crack tip for (a) coupling model (b) linear elastic solution.

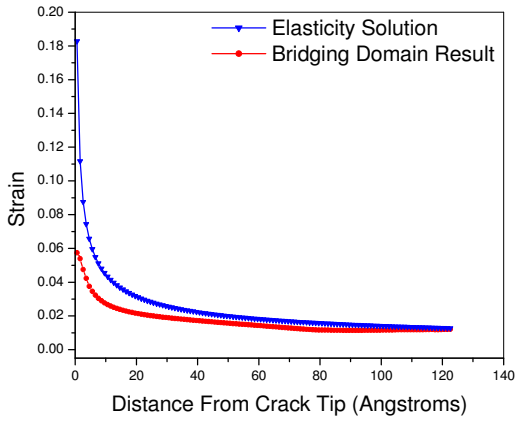

Figure 2.6. Strain along the crack calculated using coupling method and elasticity solution for a K-field.

different finite element sizes are chosen, namely, 4, 5, 10, and 20 lattice spacings. The corresponding local errors are 8.63×10^{-3}, 8.82×10^{-3}, 1.08×10^{-2}, 1.77×10^{-2}.

To illustrate the stress and strain computed by Eqs. (2.58) and (2.74), we consider an atomic sheet with a crack as an example. The dimensions of the sheet are 2262.75 Å$\times$1136.00 Å. The atomistic subdomain is 196.76 Å$\times$112.18 Å in size. An initial crack of 100 lattice spacings is introduced at the center of the sheet with the crack surface perpendicular to the loading direction ($y-$direction). Due to the symmetry, only half of the sheet ($x \geq 0$) is modelled. The stress and the strain are calculated at the prescribed strain $\varepsilon_{yy} = 1\%$. Figure 2.4 shows the contour of the strain component ε_{yy}, and figure 2.5 shows the contour of the equivalent stress (plane-stress condition is assumed for the continuum subdomain). Both the contours for the strain component and the equivalent stress agree well with those of the crack-tip fields based on continuum fracture mechanics. Strain calculated using coupling method for a K-field of strength 3 MPa$\sqrt{\text{m}}$ along the

crack is also plotted in Fig. 2.6 for a better comparison with the linear elastic closed form solution and it can be seen that the error in the strain is quite small.

2.4.2. Fracture of CNTs

Next, we apply the coupled method to study the mechanical response of defected CNTs and multiwalled carbon nanotubes (MWCNTs) with different loading conditions (uniaxial tension and twisting). The modified second-generation Brenner potential [69] is used to describe interatomic interactions. Under applied load, the CNTs are deformed beyond the linear regime, so the continuum domain in the coupling method is characterized by a nonlinear constitutive law established through the exponential Cauchy-Born rule [70]. This nonlinear constitutive law has been used to study the collapse of CNTs [27, 71]. Note that the algorithm discussed in Section 2.2.2 is only valid when the continuum response of material is linear. Therefore, we use the augmented Lagrange multiplier scheme described in [57].

Figure 2.7 shows the coupled model of a single-walled [50,0] CNT containing a double vacancy defect in the center. Fracture of small nanotubes containing such a defect has also been studied quantum mechanically[4]. The atomistic domain contains 1898 atoms, while the continuum domain consists of 1040 finite element nodes. The tube is 142 Å in length, the atomistic domain is 39.15 Å long and the overlapping subdomain is 11.36 Å long. Thus, the overlapping boundary is far enough away from the defect so that

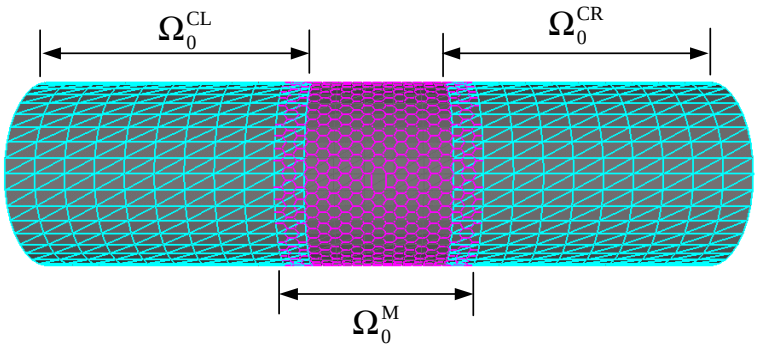

Figure 2.7. Coupled model for a [50,0] CNT; ($\Omega_0^{C} = \Omega_0^{CL} \cup \Omega_0^{CR}$ and $\Omega_0^{H} = \Omega_0^{C} \cap \Omega_0^{M}$).

the displacement field of the continuum domain can be accurately characterized by the finite element model. The full atomistic model of the tube consists of 6698 atoms.

For the continuum domain in the coupled nanotube model, the subdivision finite elements based on Loop's scheme [72] are used. The deformation field within each triangular element depends not only on the nodal displacements of its three nodes, but also on those of its first neighboring nodes. For subdivision elements difficulties arise for the triangular elements at the continuum/atomistic interfaces, for they lack neighboring elements. Thus, in the coupled model, besides adding pad atoms, virtual finite element nodes are needed to ensure that the edge nodes at the continuum/atomistic interfaces are appropriately coordinated. Thus extra row of elements extends into the continuum domain. The finite element nodal positions of these virtual elements are determined by

minimizing the difference between the atomistic displacement and the interpolated continuum displacement:

$$\eta = \sum_{\alpha} \| \sum_{I} N_I(\mathbf{X}_\alpha)\boldsymbol{\phi}_I - \mathbf{x}_\alpha \|^2, \tag{2.83}$$

for all nodes I in the pad elements. Note that the energy associated with the pad atoms and pad elements is not accounted for in the total free energy of the coupled system.

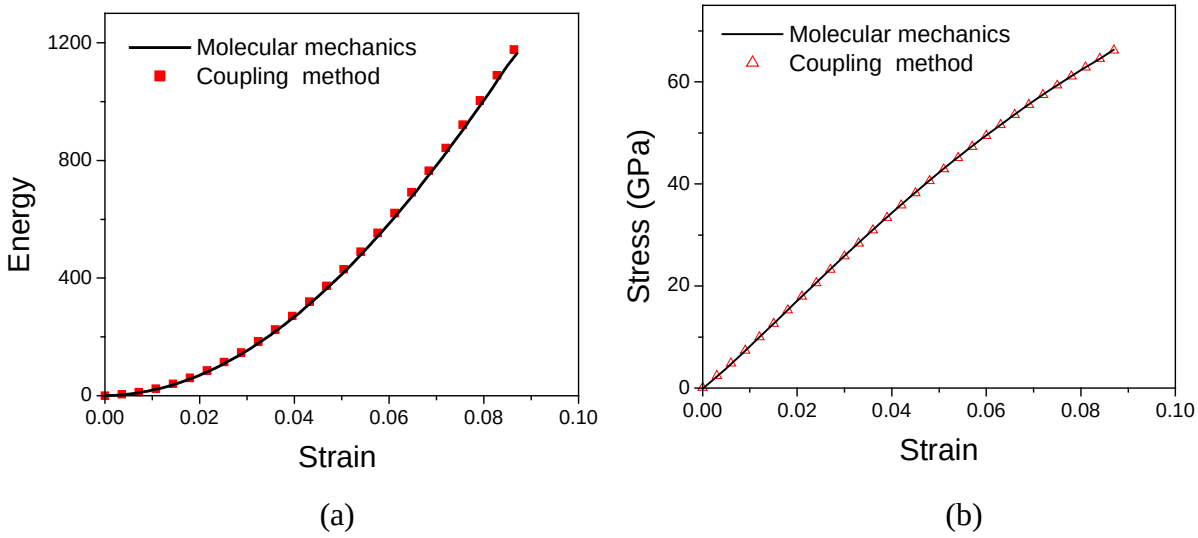

Figure 2.8. Energetics (a) and stress-strain curves (b) of stretched [50,0] CNT.

Figure 2.8 shows the results for the nanotube stretched to fracture. Figure 2.8(a) shows the energy evolution of the tube as a function of applied tensile strain. At small strains, the internal energies provided by these two models are almost indistinguishable. As the applied strain increases, the total energy predicted by the coupled model deviates slightly from the atomistic model. Figure 2.8(b) shows stress-strain curves obtained by these two methods, which are almost indistinguishable.

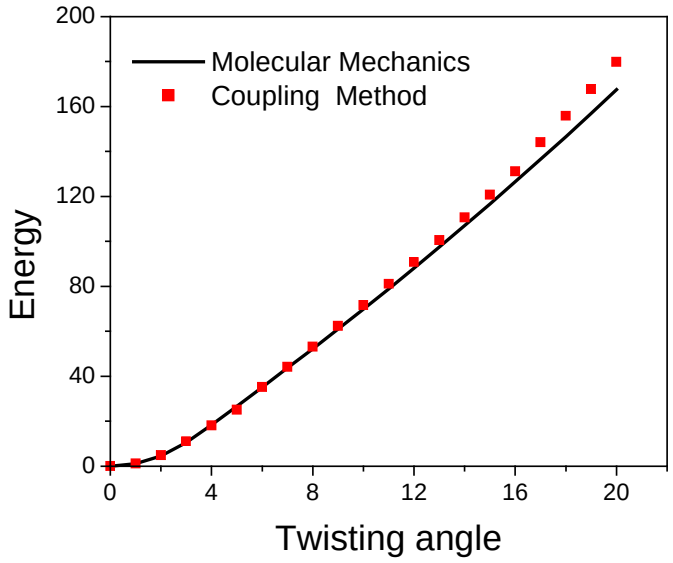

Figure 2.9. Energetics of twisted [50,0] CNT.

Figure 2.9 shows the energy evolution of the CNT twisted up to 20° by rotating its ends in opposite directions with respect to the axis of the tube. As in uniaxial tension, the energetics predicted by the two models is almost identical at small rotation angles, and deviates only slightly from each other at large strains. Figure 2.10 compares the configurations predicted by these two models at 15° rotation. It can be seen that the coupled calculation captures all of the features of the result of the full atomistic model.

The next example serves to illustrate how the atomistic model can easily be moved around once a model has been constructed. Figure 2.11 shows a three walled carbon nanotube in which the atomistic model has been replaced in two locations, first in the center of the tube, next near the support. In each case, the finite element model is modified by setting the material properties of the domain to be overlaid to zero. Note that the mesh of the finite element model is unchanged. Thus, once the finite element model has

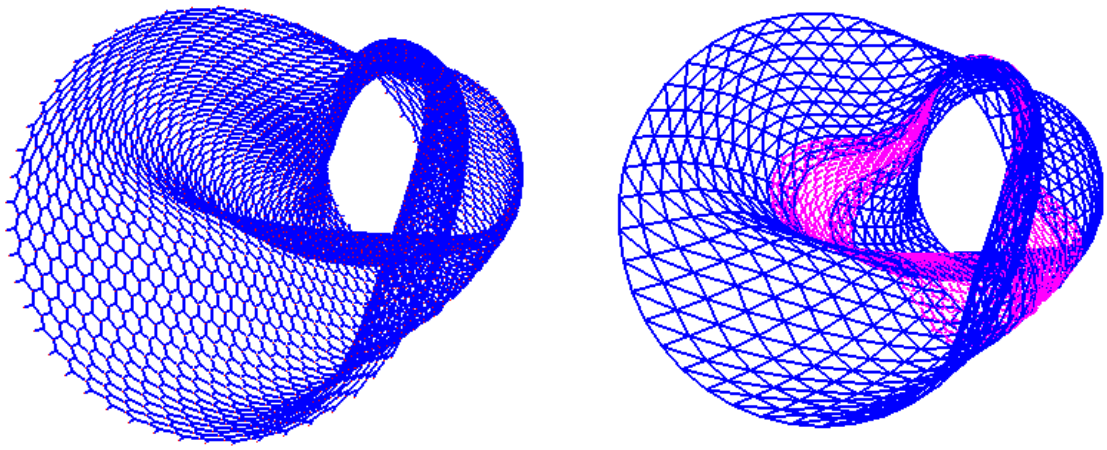

Figure 2.10. Configuration of twisted [50,0] CNT.

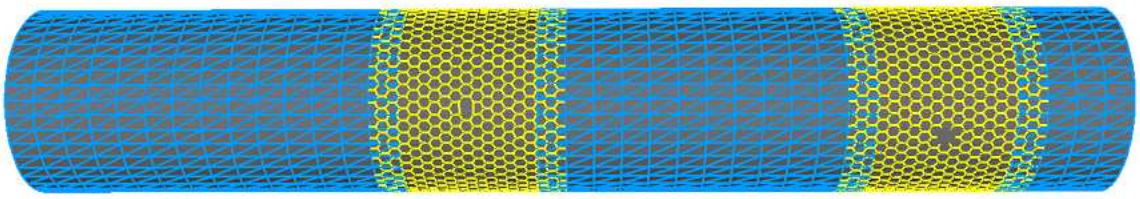

Figure 2.11. A MWCNT with two defects.

been constructed, defects in various locations of the model can easily be studied. Details of how the van der Waals forces between adjacent continuum and continuum/atomistic models are treated are given in [3].

2.5. Concluding Remarks

A coupling method for bridging molecular mechanics and finite element methods has been presented. The method is based on an overlapping domain-decomposition scheme. Displacement compatibility conditions in the overlapping subdomain are enforced

by Lagrange multipliers. A faster formulation has been developed for the case where the continuum domain is linear elastic. An important advantage of the method is that it does not require the finite element nodes to match the atoms at the interface. Such matching is a requirement in many handshake methods, i.e. [14, 19], and is inconvenient for the finite element implementation. In this method, a crystal lattice with an arbitrary lattice constant can be linked to any finite element mesh, although of course, the disparity between the mesh and lattice size should not be too large. This facilitates the placement of the atomistic model in any part of the body: to replace the continuum model anywhere by an atomistic model, it is only necessary to zero the material constants in a subdomain and superimpose the atomistic model.

A method has also been presented for computing strains based on an MLS approximation. The method exactly reproduces a strain state one order lower than the polynomial basis. Thus for a linear basis, the method gives the exact strain for atoms in a linear displacement field. In contrast to the Mott et al. [59] atomistic strain, this method does not require a Voronoi tessellation, so it is much easier to implement.

A patch test has been performed for the coupling method. The performance of this proposed coupling method in the patch test was adequate, but certain irregularities were noted in the strain in the overlapping domain. The discrepancy in the energy for the "patch" test was less than 0.1 %, which is adequate for the most scientific and engineering studies.

Numerical examples studying the mechanical responses of defected atomic sheets and carbon nanotubes are presented. Comparisons between the coupled models and the corresponding fully atomistic models show very good agreement, suggesting the adequacy of the method.

Even though molecular mechanics is more accurate in modeling mechanical behavior of atomic structures than the continuum methods, it still does not model the bond breaking phenomenon accurate enough when compared to quantum mechanics (QM) electronic structure calculations. Troya et al. [12] have shown that the MM predicts incorrect fracture mechanism for CNTs and in [4] it was found that the MM gives much smaller fracture stresses and strains for nanostructures with defects than quantum mechanical calculations. However, the QM methods are computationally very expensive, so we have developed coupled QM/MM schemes in the next chapter to model CNTs and graphene sheets containing defects.

CHAPTER 3

Coupled quantum mechanical/molecular mechanical modeling of the fracture of defective carbon nanotubes and graphene sheets

3.1. Introduction

Electronic structure calculations [73, 74, 12, 75, 76, 4, 77] of the mechanical behavior of pristine CNTs predict fracture strengths in the range of 75−135 GPa and ultimate strains of as much as 30%. However, manufacture of mass-quantities of perfect CNTs or graphene sheets may prove challenging; in practice, mechanical properties will often be limited by the presence of defects−in many cases of substantial size. Oxidative purification treatments [78, 79, 80] are commonly used in the production of CNTs and we have suggested [4, 81] that these can result in pitting, which provides a plausible explanation for the deviations between the CNT strength measurements of Yu et al. [2] and theoretical predictions. One route for the exfoliation of graphene sheets involves thermal exfoliation of graphite oxide [82]. During this process approximately 30% of the carbon atoms are lost as CO_2; thus, the resulting sheets are expected to be highly defected. A detailed understanding of the consequences of such defects may be crucial to the effective utilization of these materials.

Previous electronic structure calculations of defected CNTs were limited to small defects because of the high computational cost of QM calculations; the studies [4, 3] of larger defects were restricted to MM calculations. However, the modified [69, 83] second generation [84] Tersoff-Brenner (MTB-G2) potential employed in those calculations tends to systematically underestimate the strength of both pristine and defected CNTs as compared to QM calculations, and has been shown [12] to predict qualitatively different mechanisms for the fracture of defected CNTs. Thus, a better understanding of the role of defects in CNTs necessitates electronic structure calculations.

One way to treat a system of large molecules is to adopt linear scaling QM methods, which reduce the order of computation to $O(N)$, where N is the total number of orbitals. However, these methods are generally not accurate for covalent bonds and their convergence for systems with defects is problematic. Another approach to treating large systems is to couple a QM method to an MM method so that the important regions of the system are treated quantum mechanically and MM interactions are used elsewhere. In fracture studies, only part of the system, such as the vicinity of defects, requires an accurate treatment of bond breaking; for such systems QM methods can be used for these regions and MM methods can be applied to the rest of the system. Although the MM potential does not need to be able to model bond fracture accurately, it must still predict stiffnesses and strengths that are consistent with the QM results; in the following we will present a simple scaling scheme to improve the compatibility of the QM and MM mechanical properties.

Here we describe a coupled quantum mechanical/molecular mechanical (QM/MM) method. We report the results of calculations of the fracture of CNTs with defects of moderate size and the fracture of graphene sheets. We also consider the effect of lattice trapping [85, 86, 87, 88] on fracture strength by calculating the energy release rate of a crack in a QM/MM model of a graphene sheet using the J-integral [89] method.

The rest of this chapter is organized as follows. Section 3.2 gives an overview of the coupling method and its implementation. In Sec. 3.3 the results of fracture in the presence of defects such as one- and two-atom vacancy defects as well as nanosized holes and slits are presented. Section 3.4 describes the results for lattice trapping in graphene sheets. Conclusions are given in Sec. 3.5.

3.2. Method

The coupled QM/MM method adopted here is a two-layer ONIOM scheme [32]. The MM interaction potential is a modified [69] version of a second generation Tersoff-Brenner [84] potential; in particular, the cutoff function is removed and instead interactions are only retained for atom-atom pairs that are separated by less than 2 Å in the initial (unstrained) configuration. The name MTB-G2 will be used to distinguish this version of the potential from the standard second generation reactive empirical bond order (REBO) potential, which retains the cutoff function. Fracture studies with REBO potentials in which the cutoff function is retained leads to qualitatively inaccurate behavior.

Two types of QM interactions are considered: semi-empirical (PM3) calculations obtained with the GAMESS software package [90] and DFT calculations. The DFT calculations were performed using the Spanish initiative for electronic simulations with thousands of atoms (SIESTA) package. [91, 92] The Perdew-Burke-Ernzerhof (PBE) GGA functional, a double-ζ plus polarization basis set, and Troullier-Martins [93, 94] pseudopotentials were used. Core radii of 1.15 and 1.25 a_0 were used for carbon and hydrogen, respectively, and a non-linear exchange-correlation correction pseudocore radius of 1.50 a_0 was used for carbon. Periodic boundary conditions were employed for the calculation of the surface energy density, whereas cluster calculations were used for the remaining DFT calculations. The Γ point was used for Brillouin zone sampling and diagonalization to solve the Kohn-Sham equations. We used spin-restricted QM calculations for all of the work presented here. Spin unrestricted calculations are generally more accurate, but they are more time consuming, difficult to converge, and are subject to issues of spin contamination which would need to be carefully assessed before they could be used. For our present goals, spin-restricted calculations were deemed adequate.

ONIOM [32] is a widely-used method for coupling in QM/MM calculations due to its simplicity of implementation. It is a general framework that combines layers of computational methods of different levels of accuracy. In the two-layer ONIOM scheme employed here, the energy is given by

$$E = E^{\mathrm{MM}} + E_{\mathrm{F}}^{\mathrm{QM}} - E_{\mathrm{F}}^{\mathrm{MM}}, \tag{3.1}$$

where E^{MM} is the MM energy of the entire system, and $E_{\mathrm{F}}^{\mathrm{QM}}$ and $E_{\mathrm{F}}^{\mathrm{MM}}$ are, respectively, the QM (higher level) and MM (low level) energies of a special subdomain, hereafter usually just referred to as either the QM subdomain or simply the "fragment", within which accurate treatment of bond behavior is desired. The complement of this region will occasionally be referred to as the MM subdomain. We have parenthetically added "low level" and "high level" to MM and QM, respectively, since QM method is obviously a higher level approach which will be applicable where bond breaking takes place.

In calculations for the fragment we employed hydrogen link atoms to saturate the dangling bonds created by cutting covalent bonds that straddle the interface. The link atoms were positioned to lie 1.09 Å along the vector connecting a boundary QM atom and its nearest neighbor across the boundary. The positions of the link atoms were not included in the degrees of freedom of the molecule and were not part of the geometry optimization. The use of hydrogen link atoms to terminate the dangling bonds of a fragment domain consisting of a conjugated graphitic network significantly alters the bond orders of the C-C bonds near the boundary and this can alter properties further inside the domain. To judge the errors introduced by this complication, we repeated our calculations with larger fragments and only report results where the error due to domain truncation is less than 10%.

The energy is minimized by a variable-metric function-minimization routine [95] to obtain the optimized geometry. In the computations reported here, the end carbon atoms of the model were displaced axially with a strain increment of 0.5% until fracture

occurred. The end carbon atoms were constrained to a plane. The tensile strain is defined as

$$\varepsilon = \frac{\Delta l}{l}, \tag{3.2}$$

where l is the initial length of the specimen and Δl is the change in the length. Note that this definition, which corresponds to engineering strain, is not an appropriate general definition of strain for the large deformations obtained here; but because we are only concerned with axial deformation, it is adequate (see Belytschko et al. [63]). At each strain increment the tube configuration was optimized.

The numerical procedure at each strain increment can be summarized as follows:

(1) Calculate the MM energy of the full system.

(2) Calculate the QM and the MM energy of the fragment capped with the link atoms.

(3) Calculate the energy of the system using Eq. (3.1).

(4) Check the convergence criterion, $max|\text{gradient}| < \epsilon$. If the convergence criterion is satisfied, the configuration is considered an equilibrium configuration, otherwise update the atomic positions and repeat from (1).

Where possible, we made use of approximate Hessian information and starting orbitals for the QM energy evaluations that were available from the prior strain steps. Once the geometry is optimized at a certain applied strain, the tensile stress in the tube is calculated as the sum of the axial components of the forces on the carbon atoms at one

end of the CNT divided by the cross-sectional area:

$$\sigma_z = \frac{\sum_{\alpha=1}^{m} F_{\alpha z}}{\pi D t}, \tag{3.3}$$

where m is the number of carbon atoms at one end of the tube, $F_{\alpha z}$ is the axial force on atom α, D is the current diameter of the tube, and $t = 3.4$ Å is a nominal value of the thickness of the CNTs (taken to be the interlayer spacing in graphite). Note that all of our calculations are for the true stress, so the diameter is a strain dependent parameter. Wherever possible, we obtained the value of the CNT diameter from an undefected region of the fragment subdomain because the QM and MM methods predict significantly different Poisson's ratios and the goal of the QM/MM calculations is to match the results of pure QM calculations as closely as possible. Assuming a nominal thickness to define stress is a standard procedure for monolayer atomic sheets such as graphene and CNTs; a more unambiguous definition is based on a force per linear dimension, see Arroyo and Belytschko. [96, 67]

It is crucial in coupled QM/MM simulations of fracture that the MM model matches the QM model over a large range of strains; the upper end of this range should be near the fracture stress. Otherwise, various types of spurious phenomena occur which are simply a result of strength and stiffness mismatch between the QM and MM models. For example, if the strength of the MM model is less than that of the QM model, fracture can occur in the MM subdomain, even if the MM subdomain does not contain a defect

and the QM subdomain does. Another consequence of such a mismatch occurs when a crack attempts to grow into a QM fragment from the MM subdomain: the crack can be deflected back into the MM model if the QM model is stiffer than the MM model.

These mismatches are of concern here because the standard MTB-G2 potential is significantly less stiff and weaker than the PM3 model. For example, for a [5,5] CNT containing a Stone-Wales(SW) defect [97] as reported in Mielke et al. [4], the fracture stress calculated by pure QM calculations is 115 GPa, whereas the fracture stress of a [5,5] pristine tube obtained by MM calculations is 105 GPa. Consequently, if a QM/MM method is used with a QM treatment around the SW defect, the pristine part of the CNT will fail before the defective QM fragment.

To avoid these anomalies, the MTB-G2 energy was scaled so that the low-strain Young's modulus for a CNT closely matches that obtained from a QM calculation. For the armchair CNTs, the scaling factor was chosen to be 1.4 and for the zigzag CNTs the scaling factor was chosen to be 1.2. Similarly, the scaling factor for a graphene sheet was chosen to be 1.4 for QM(PM3)/MM calculations and 1.2 for QM(DFT)/MM calculations.

Our main justification for the scaling is that it matches the MM model more closely to the QM model at lower stresses. Since the fracture properties of the tube are governed by the region encapsulating the defect, which is treated quantum mechanically, the calculated strength is not affected much by the scaling of the MM potential. Another justification for the scaling is the fact that we have found for the quantum fragments used here, the results converge (i.e., the difference between successively larger fragments

decrease). Furthermore, the results of the QM/MM calculations tend to the results of the pure QM calculations. However, we were not able to establish this trend for the largest models we used because pure QM calculations for these were beyond our resources.

Griffith's criterion [98] for fracture in brittle materials states that a crack will extend when the strain energy released by such extension exceeds the energy needed to create a newly fractured surface. This is a thermodynamic criterion and can be used to predict a rigorous lower bound for the fracture stress as a function of the crack length. For the special case of a linear elastic material, the fracture stress for a crack in a thin finite sheet of width w is given by [99]

$$\sigma_{\mathrm{f}} = \sqrt{\frac{2E\gamma}{\pi a}\cos\left(\frac{\pi a}{w}\right)}, \tag{3.4}$$

where a is the size of the defect (half-length of the crack) and $a << w$, E is Young's modulus, and γ is the surface energy density. Note that graphene is nonlinear, so Eq. (3.4) is only an approximation to the Griffith stress.

The appropriate γ to use [86] in calculations of the Griffith formula is the work per unit area needed to *reversibly* separate the fracture surfaces. Thus, it includes contributions from relaxation of the fragments. The unrelaxed surface energy density for such calculations has been used previously [100, 101, 102], and may provide a better estimate of the true fracture stress because of cancelation of errors. However, the relaxed surface

energy provides the proper basis from which to judge the contributions of lattice trapping effects. Our values of γ are obtained by dividing the difference between the energy of a pristine material at its optimized geometry and the energy of the two fragments after they are fractured along the desired surface, separated to infinity, and subsequently optimized to yield their equilibrium geometries, by twice the surface area (where the factor of two is included because fracture leads to two surfaces).

3.3. Results and Discussion

3.3.1. Small defects

We begin by studying the effects of small defects, one- or two-atom vacancy defects and a Stone-Wales defect, [4] on the mechanical strength of small CNTs: [5,5] armchair and [10,0] zigzag tubes. The purpose of these computations was to examine how well the QM/MM calculations reproduce the results of pure QM calculations. The QM results were therefore considered as "benchmark" results, with the difference between the QM/MM and the QM computation indicating errors due to coupling. QM/MM methods are ubiquitous in many areas of chemistry but they are much less common for the study of fracture, [88, 15, 14, 103, 104, 105, 106, 107] and quantitative comparisons of these methods to full QM methods are needed to explore their effectiveness in modeling fracture.

The QM/MM nanotubes were approximately 85.0 Å in length. The [5,5] nanotubes contained 700 atoms, the [10,0] contained 820 atoms. In both cases, the ends of the tubes were capped by hydrogen atoms. The two-atom vacancy defect was created by removing

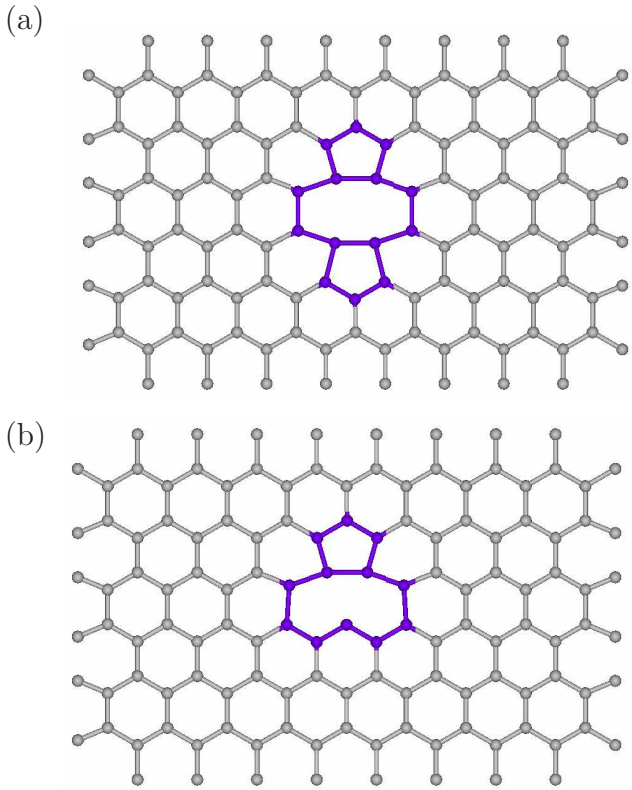

Figure 3.1. (a) Two-atom and (b) one-atom vacancy defects shown on a graphene sheet.

two adjacent atoms and the resulting 14 atom ring reconstructs to form one octagon and two pentagons as shown in Fig. 3.1(a). Two-atom vacancy defects can be produced in CNTs by irradiation with energetic ions or electrons [108, 109]. Figure 3.2 shows the QM fragment in the center of a [10,0] CNT surrounding the two-atom vacancy defect. The QM fragment covers a circular band around the entire circumference of the CNT, so that no QM bonds are stressed in parallel with the MM bonds.

Figure 3.3 shows the stress-strain curves for a [10,0] CNT with a two-atom vacancy calculated by the QM/MM method with increasing fragment sizes, along with the QM

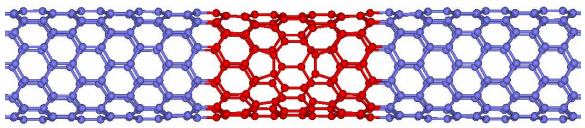

Figure 3.2. Coupled QM/MM model: the central region constitutes the QM fragment (QM atoms, dark red dots; MM atoms, light blue dots).

results of a CNT containing 198 atoms calculated by Mielke et al. [4, 110] and the scaled and unscaled MM results. In the scaled MM calculations, the energy was scaled by the same factor as in the QM/MM calculations. The scaled MM results compare quite well with the QM and QM/MM results. In the QM/MM calculations, the largest quantum fragment is a 158 atom cylindrical band. It can be seen that for the 158 atom fragment, the stress-strain curve for the QM/MM calculations agrees well with the full QM calculations. The major discrepancy is that the QM/MM model fails at a somewhat smaller strain (0.130 vs. 0.142) and somewhat smaller stress (103 GPa vs. 107 GPa) than the QM model. Undoubtedly, an even larger fragment would compare better with the full QM treatment, but we deemed the 158 atom fragment adequate for our purposes.

It is noteworthy that the QM/MM model, like the full QM model, can sustain larger strains and stresses than the MM model, and fracture always initiates in the QM region. The scaled and unscaled MM models failed at a strain of 0.085, whereas for QM and QM/MM models fracture strain was greater than 0.130. A complication that arises for QM fracture studies of finite-sized CNTs is that Peierls distortions [111, 112] can lead to distorted bond lengths as a function of the position along the tube axis and this can

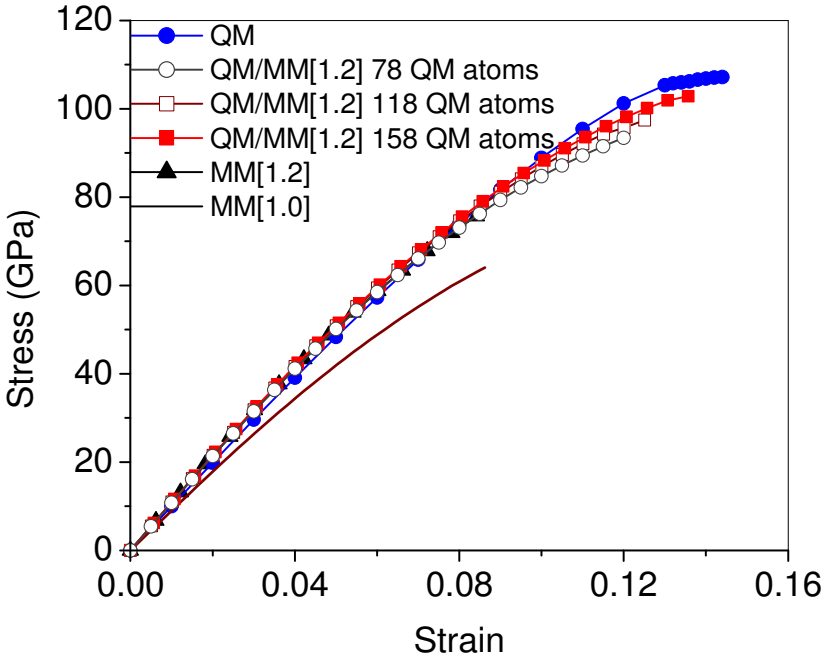

Figure 3.3. Stress-strain curves of [10,0] CNT with a two-atom vacancy. PM3 was used for the QM/MM and QM calculations. The scaling factor used for the MM potential is given in the square brackets. The QM results were taken from Mielke et al. and Troya et al.

result in multiple fracture pathways [4]. These are purely quantal effects that have a very strong size dependence so they are difficult to model precisely by QM/MM methods.

Figure 3.4 shows the stress-strain curves for a [5,5] CNT containing a one-atom vacancy. It can be seen that with the different scaling of the MM energy for the armchair CNT, we were able to replicate full QM results [4, 110] quite well with the QM/MM model. Again, the scaled MM results also match the QM and QM/MM results quite well, although the fracture strain is somewhat lower: 0.117 by molecular mechanics vs. 0.153 by quantum mechanics.

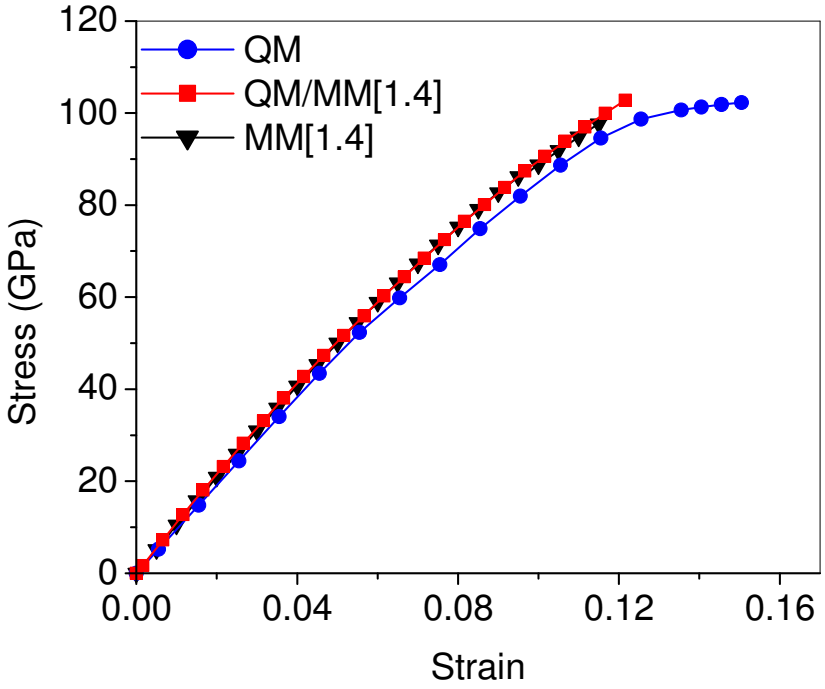

Figure 3.4. Stress-strain curves of [5,5] CNT with a one-atom vacancy. The QM subdomain consisted of 89 atoms. PM3 was used for the QM/MM and QM calculations. The scaling factor used for the MM potential is given in the square brackets. The QM results were taken from Mielke et al. and Troya et al.

Table I lists the fracture stresses and strains calculated for these CNTs along with the corresponding values for the pristine tubes reported in Mielke et al. [4] In the [10,0] CNTs, the QM/MM failure stress is about 6% below the QM fracture stress, whereas for the [5,5] CNTs they are 3 to 5% higher. The unscaled MM fracture stresses are significantly lower, especially for zigzag CNTs, where the difference is about 40%. With the scaling, the agreement improves and the differences are about 25%.

A noteworthy difference between the QM/MM and the scaled MM computations is that the CNTs can be stretched to higher strains in the QM/MM model than in the

Table 3.1. Fracture properties calculated using pure QM, QM/MM, and MM methods. All stresses are in GPa. All the QM results were taken from Mielke et al. and Troya et al. PM3 was used for all the QM/MM calculations. Scaling factors of 1.2 and 1.4 were used for [10,0] and [5,5] CNTs respectively, for all of the QM/MM calculations and the scaled MM calculations. Note that the fracture strain for the scaled and unscaled MM calculations are the same. Also note that we do not report the QM/MM strengths of pristine CNTs, as they fractured at the QM/MM interface or in the MM region. P stands for pristine, DV stands for symmetric two-atom vacancy defect, SV stands for symmetric one-atom vacancy defect and SW stands for Stone-Wales defect.

Chirality Defect	QM Stress	QM/MM Stress	Scaled MM Stress	MM Stress	QM Strain	QM/MM Strain	MM Strain
[10,0] P	124	-	106	88	0.200	-	0.181
[10,0] DV	107	103	77	64	0.142	0.130	0.085
[10,0] SV	101	95	78	65	0.130	0.122	0.089
[5,5] P	135	-	147	105	0.300	-	0.297
[5,5] SW	125	131	123	88	0.220	0.186	0.162
[5,5] SV	100	103	99	71	0.153	0.121	0.117

MM model. Consequently, the QM/MM calculations predict higher fracture strain but similar values of Young's modulus as the scaled MM model. On comparing the results of coupled QM/MM and MM calculations, we found that in the former the bonds at the edge of the defect are able to sustain much larger strains. It can be seen from Figs. 3.3 and 3.4 that there is little difference in the initial slopes of the stress-strain curves, i.e., in Young's modulus, between the QM/MM and scaled MM calculations.

We also studied the convergence of pure QM calculations with model size for the same system as was presented in Fig. 3.3. Calculated failure stresses obtained with 118 and 158 atom models both agreed with the 198 atom model to within 1 GPa. This shows that the ONIOM based QM/MM algorithm with hydrogen link atoms tend to the long

cylinder solution more slowly than pure QM calculations for the special case where the QM subdomain consists of a cylindrical section of a nanotube. We have only noticed this effect for calculations where the QM region consists of cylindrical subdomains. Additionally, pure QM calculations are not affordable for the larger tubes that we consider next, so QM/MM calculations provide the only practical scheme for including quantum effects in fracture studies in models of these sizes.

3.3.2. Slits and Hexagonal and Circular Hole Defects

We next consider the effect of larger defects on the strength of CNTs. Both slit-like and hole defects were studied. We chose slits because crack-like defects are not readily amenable to QM treatments. In MM calculations, cracks are customarily modeled by artificially removing a single row of bonds. This is not feasible quantum mechanically because unless the atoms adjacent to the crack are separated by a significant distance, the bonds persist, i.e., a loss of cohesion between atoms only occurs at a significant separation, which is much greater than the lattice constant.

This observation also has significant implications for actual cracks at the nanoscale, as it suggests that crack-like defects can not exist in an unstressed covalently-bonded material unless at least one row of atoms is absent or the crack surfaces become chemically modified. Thus, the notion of atomistically sharp cracks and MM models with cracks represented by simply omitting bonds must be considered very carefully.

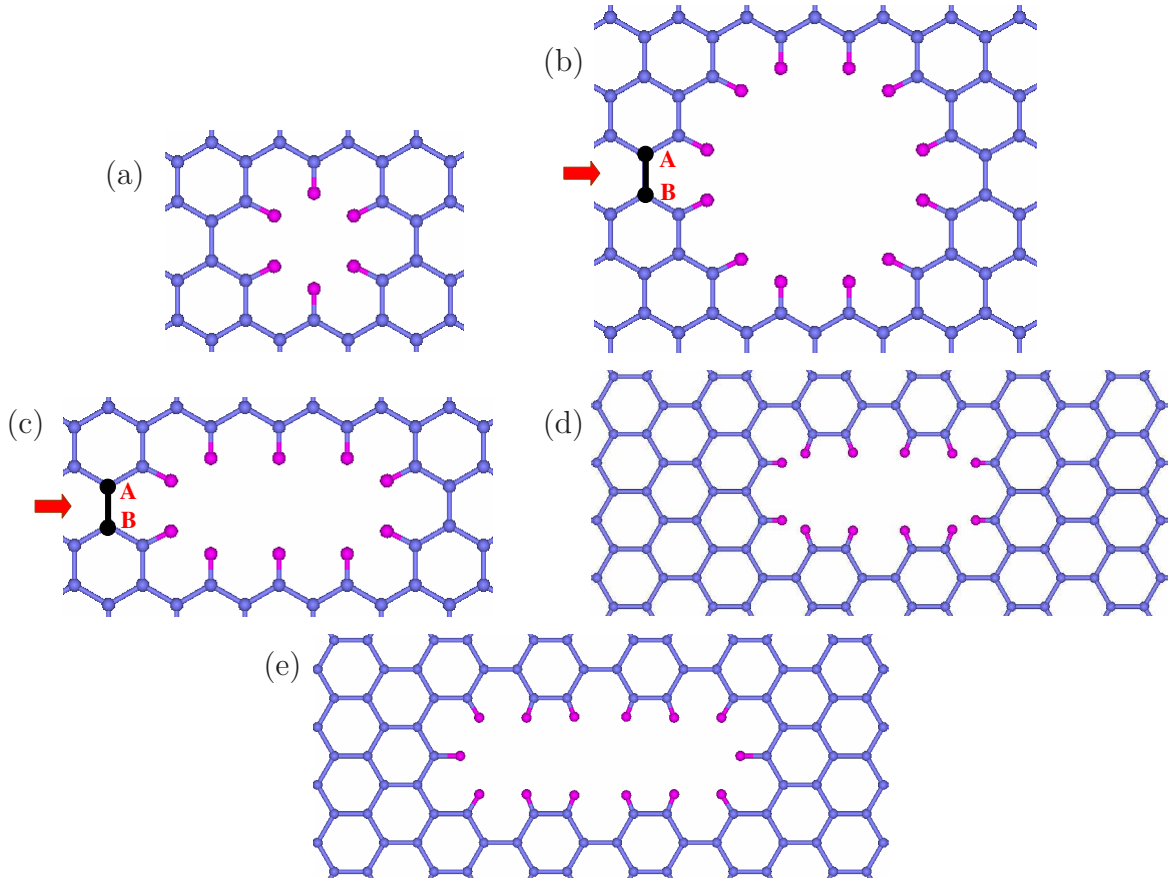

Figure 3.5. Hole and circumferential slit defects in CNTs (carbon, light blue dot; hydrogen, dark pink dot) (a) A slit or hole of index zero, (b) hole of index one and (c) slit of index one in a zigzag CNT; (d) a slit of index one (e) and two in an armchair CNT. Local strains are calculated for the bonds in black, shown by red arrows in (b) and (c).

The hole defects were formed by removing hexagonal units of atoms as presented previously [4, 3], see Fig. 3.5. We denote the size of the hole by a size index: a zero index hole is created by removing one hexagonal unit, a hole of index one is created by removing a ring of six hexagonal units surrounding this hexagon, a hole of index n by removing the n^{th} ring of hexagonal units [4, 3]. In a zigzag tube, circumferential slit defects are created

by removing four rows of carbon atoms as shown in Fig. 3.5(c), whereas in an armchair CNT, slit defects are created by removing three rows of carbon atoms as shown in Figs. 3.5(d) and 3.5(e). For both zigzag and armchair CNT, the size index for a slit is defined so that a slit of index n is of the same length as the diameter of a hole of index n. Note that the holes are created in the same way for both the zigzag and armchair tubes, i.e., by removing hexagonal units of atoms, whereas construction of the slit defects is different. Also note that a zero index hole is identical with a zero index slit. Figure 3.5 shows holes and slits of indices zero and one in a zigzag CNT and slits of indices one and two in an armchair CNT. In all cases, the dangling bonds at the hole/slit edges were terminated with hydrogen atoms so as to create defects with plausible bonding structures as shown in Fig. 3.5.

We considered [50,0] and [29,29] CNTs containing ∼4000 atoms which were 94.5 Å and 83.6 Å long, respectively. Using a quantum fragment which covers the entire circumference for such large CNTs is computationally too expensive, so patch-shaped quantum fragments were used instead, an example of which is shown in Fig. 3.6. The QM patches used for small slits are shown in Fig. 3.5.

Using the QM/MM method, the fracture stresses of [50,0] CNTs with holes of size index zero to four and slits of size index zero to eight were calculated (see Fig. 3.7). These results show that the fracture strengths for holes and slits with the same size indices, i.e., where the length of the slit is equal to the diameter of the hole, differ by less than 5%. Similar agreement between fracture stresses of holes and slits was obtained by molecular

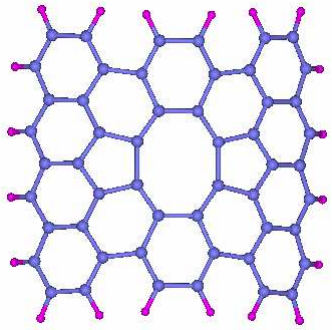

Figure 3.6. A patch quantum subdomain for a [29,29] CNT containing a two-atom vacancy defect(carbon, light blue dot; hydrogen, dark pink dot).

mechanics [3]. This is in stark contrast to continuum mechanics at the macroscale, where the weakening effect of holes is much less than the weakening effects of cracks (i.e., slits). To ensure that the small differences in fracture stresses of the holes and slits of the same defect indices are not due to differences in the sizes of the quantum fragments, the fracture stresses of slits of index one and two for a [50,0] CNT were calculated using a quantum fragment of the same size as for the corresponding holes. The computed strength, as can be seen from Fig. 3.7 and also tabulated in Table II, does not change significantly with the QM subdomain size. Note that the MM results have been scaled by the same scaling factor used for the QM/MM calculations. It is observed that even though the fracture stresses obtained by the QM/MM method are higher than those calculated by molecular mechanics, the trend of the fracture stress versus defect size remains the same.

The results for the fracture of defected [29,29] CNTs are shown in Fig. 3.8. The dependence on defect-size index and the relationship between the scaled MM results and the QM/MM results is similar to what was observed for [50,0] CNTs. For armchair

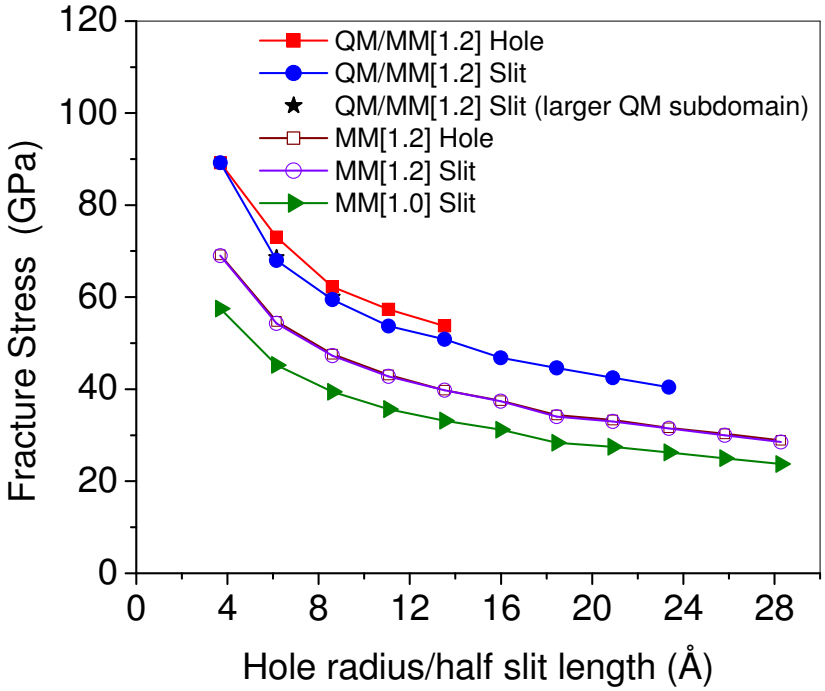

Figure 3.7. Dependence of the fracture stress of a [50,0] CNT on the defect size for holes and slits. PM3 was used for all the QM/MM calculations. The scaling factor used for the MM potential is given in the square brackets.

Table 3.2. Variation of fracture stress and strain of the QM/MM model with QM fragment size for a [50,0] CNT with slits of indices one and two. PM3 was used for all the QM/MM calculations. The MM potential was scaled by a factor of 1.2.

Slit index	Number of atoms in fragment	Fracture Stress(GPa)	Fracture Strain
1	68	68.0	0.077
1	104	68.6	0.077
2	84	59.5	0.072
2	148	60.0	0.072

tubes, spin-restricted QM calculations predict that a surface perpendicular to the tube axis has the lowest surface energy density (5.39 J/m^2 and 5.44 J/m^2 for PM3 and DFT, respectively) whereas the MM potential predicts a higher surface energy density than

was observed for zigzag CNTs (5.09 J/m^2 vs. 4.90 J/m^2). Thus, the fracture within the QM subdomain remains perpendicular to the tube axis but thereafter the fracture surface becomes jagged. Although zigzag tubes have a higher value of γ at the QM level than armchair tubes, the latter possess higher fracture strengths. PM3 calculations for γ are roughly 40% higher for armchair CNTs if fragment relaxation is neglected whereas in zigzag tubes neglecting fragment relaxation produces γ values that are only a few percent higher. In the relaxed armchair CNT fragments, the C-C bonds along the newly created surface have bond lengths of $\sim$1.2 Å and are reminiscent of the triple bonds observed in benzyne. These results suggest that fracture for armchair CNTs will display a significant lattice trapping effect. The correlation between large surface relaxation and large lattice trapping effects has already been observed in SiC fracture by Perez and Gumbsch [113].

In order to develop an understanding of the differences between the QM/MM and MM predictions of fracture, we studied the elongation of the bonds which break first and initiate the fracture. For the hole and slit of index one in a [50,0] CNT, these bonds are labelled AB in Fig. 3.5. The strain in these bonds for QM/MM and MM calculations are plotted versus applied axial strain in Fig. 3.9. It can be seen that the strain in the bond that fails is much higher than the applied strain due to the strain concentration at the defect tip. The bond strains obtained by the MM and the QM/MM calculations vary almost identically until the applied strain reaches 4.5%, at which point the bond AB in the MM model breaks. In the next strain increment, catastrophic fracture breaks the tube into two pieces. On the other hand, in the coupled model, where the critical bond

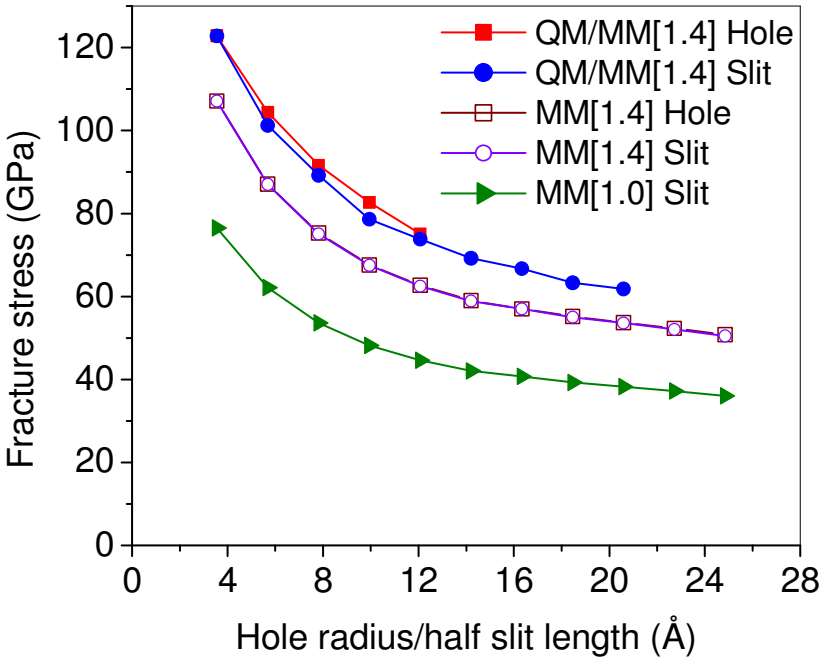

Figure 3.8. Dependence of the fracture stress of a [29,29] CNT on the defect size for holes and slits. PM3 was used for all the QM/MM calculations. The scaling factor used for the MM potential is given in the square brackets.

is treated quantum mechanically, bond AB stretches to a larger strain without breaking. This is a major difference between the behavior of the MTB-G2 potential and the QM calculations: quantum mechanically bonds around a defect can stretch much more without breaking, thus resulting in higher fracture strains and somewhat higher fracture stresses. It is of interest that the behavior of the bond that breaks first is similar in slits and holes; this is true for both the molecular mechanics and the coupled model.

The holes in the preceding studies are hexagonal rather than circular. We also generated some holes with the same opening size normal to the direction of loading but with a more circular shape. Fig. 3.10 shows this kind of hole defect of size index 10 in a graphene sheet. Fracture stresses were calculated for such circular holes with indices six to

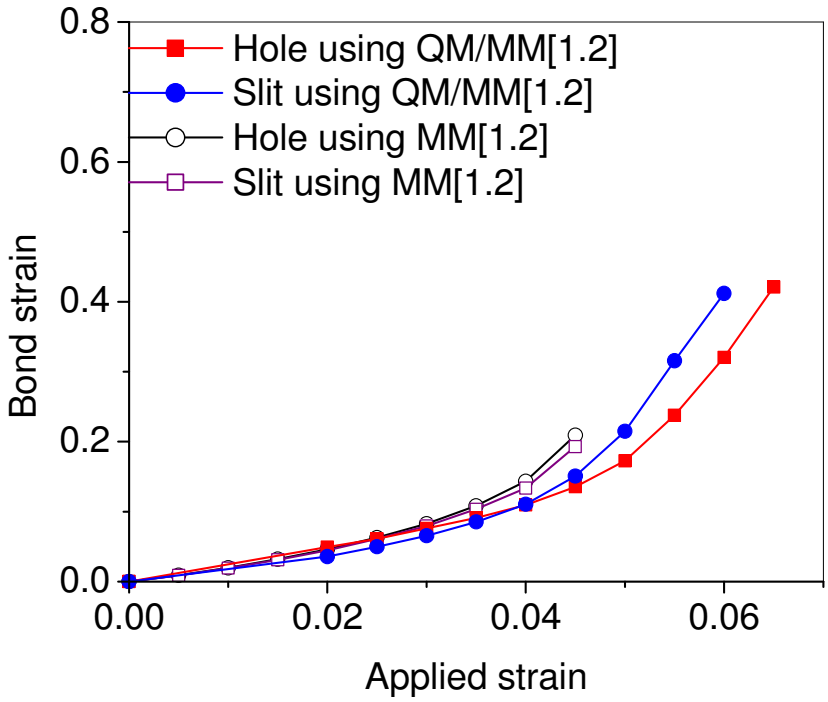

Figure 3.9. Strain in the bond at the fracture initiation site calculated for a slit and hole of index one in a [50,0] CNT using MM and QM/MM models. PM3 was used for the QM/MM calculations. The scaling factor used for the MM potential is given in the square brackets.

eight using MTB-G2 in a [50,0] CNT (defects with size-index ≤ 5 are already as circular as possible). The results are given in Table III. Even though the amount of material removed in the hexagonal opening is less than in the circular opening, the strength of CNTs with circular hole defects is about 40% larger. Thus, it is apparent that the corner, labelled C in Fig. 3.10(a), results in a significant decrease in strength. If, as seen from the results in Table III, two extra carbon atoms are added to the corners of the hexagonal holes to blunt the fracture initiation site, the fracture strength increases to nearly that observed in the rounded holes. Thus, the shape of the defect at the fracture initiation

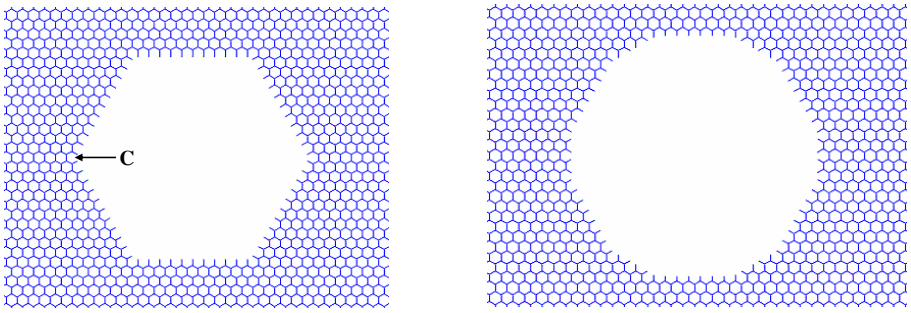

Figure 3.10. (a) A hexagonal hole and (b) a circular hole of size index 10 in a graphene sheet. C indicates a corner of the hexagonal hole.

Table 3.3. Fracture stresses calculated using molecular mechanics for slits, hexagonal holes, and circular holes for a [50,0] CNT. The blunted hexagonal holes were created by adding two extra carbon atoms to the corners of the hexagonal holes. All stresses are in GPa.

Size index	Slit	Hexagonal hole	Circular hole	Blunted hex. hole
6	28.3	28.7	40.5	37.6
7	27.5	27.8	38.0	36.7
8	26.2	26.3	36.7	34.7

site and the cross section of the defect perpendicular to the loading direction are the key features determining the fracture strength.

Next we compared the fracture stresses calculated using the coupled method with the Griffith formula stress σ_{f} [Eq. (3.4)] for slits in a finite graphene sheet. We considered graphene sheets, which have similar bonding as CNTs, because long slits can be modeled more easily in the sheets. To avoid any effects due to the finite-size of the graphene sheets, Mattoni et al. [101] suggested that the length and width of the sheet should be more than five times the crack length. To simulate such big sheets we coupled our

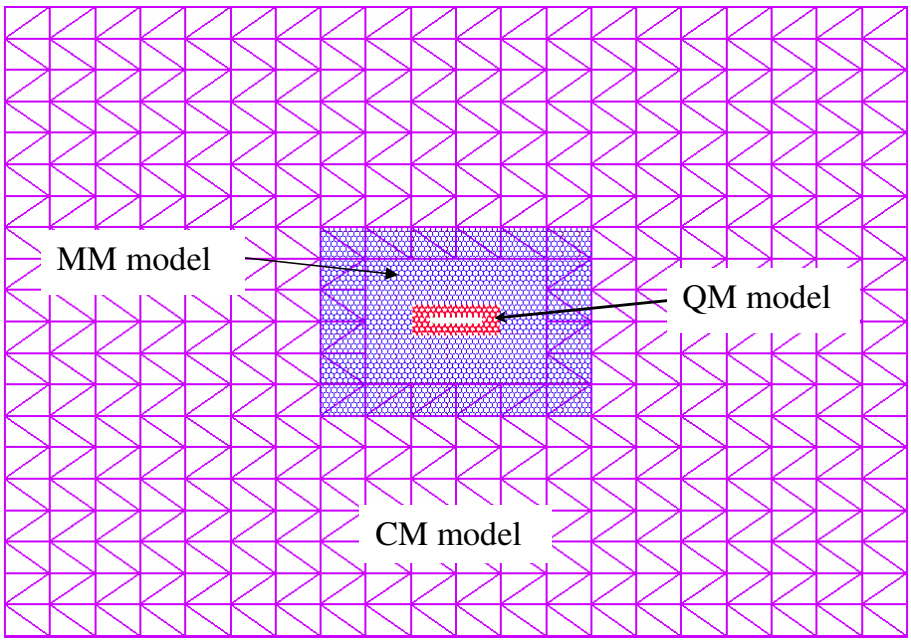

Figure 3.11. A coupled QM/MM/CM model of a graphene sheet with a defect.

atomistic model with a continuum mechanical (CM) model using an overlapping domain-decomposition scheme, known as the bridging domain method. [27, 16] In this method, a linear-elastic finite-element model is used for the continuum representation. The constraints on the displacements in the continuum-atomistic overlapping domain are imposed by the Lagrange-multiplier method. Quantum mechanics was applied on a small region surrounding the slit and the coupled continuum-atomistic model was applied elsewhere as shown in Fig. 3.11. The dimensions of the full sheet were 393.5 Å $\times$ 411.8 Å, where the atomistic region was 115.5 Å $\times$ 82.3 Å, and located in the center of the sheet. A rectangular patch containing the slit was chosen as the QM fragment, as shown in Fig. 3.5 for small slits.

The results computed by QM/MM/CM method decrease roughly well with the inverse of the square root of the crack length. Furthermore, they agree quite well with the predictions of the Griffith formula, Eq. (3.4). Thus, it can be inferred that continuum fracture mechanics agrees quite well with electronic structure calculations for defects as small as ∼20 Å. Mattoni et al. [101] obtained an even better agreement between the Griffith formula and molecular mechanics calculations on SiC with a Tersoff model.

Although the Griffith stress is a rigorous lower bound on the fracture stress, the approximate stress estimate of the Griffith formula [Eq. (3.4)] need not be, and as seen in Fig. 3.12 it predicts results somewhat below the numerical ones for slits shorter than about 20 Å. However, the shape of such small slits, as can be seen from Fig. 3.5(a), bears little relationship to what is commonly called a crack, so the inadequacy of the Griffith formula for small slits is not surprising.

These results are somewhat in disagreement with the arguments of Gao et al., [114] who propose that materials are defect tolerant at the nanoscale and that there is little difference between the theoretical strength and the strength of prefect crystals in the presence of cracks less than 30 nm in length. However, here, we observe that the fracture stresses decrease monotonically and sharply from the pristine strength of ∼115 GPa as the defect size increases. The computed strengths displayed in Fig. 3.12 are within 10% of the Griffith formula results for slits as short as 20 Å. This supports the arguments in Ballarini et al. [115]

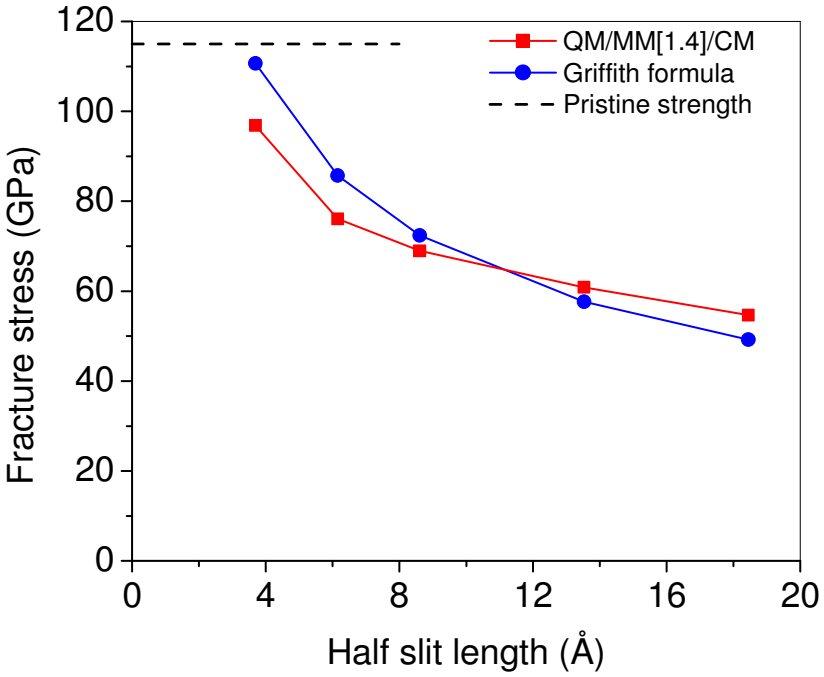

Figure 3.12. The fracture stress of a graphene sheet, containing slits, and strained in a direction perpendicular to the zigzag edge, calculated using the QM/MM/CM method, and compared to results of the Griffith formula. PM3 was used for the QM/MM/CM calculations. The scaling factor used for the MM potential is given in the square brackets.

3.4. Lattice Trapping for Graphene Sheets

An interesting question concerning fracture at the nanoscale is whether it differs markedly from fracture at the macroscale. The major assumptions in the derivation of the Griffith formula that do not apply to graphitic materials are:

(1) The linearity of the stress-strain law.

(2) Constant energy release, i.e., the neglect of lattice trapping.

The stress-strain law for graphitic materials is somewhat nonlinear, as is apparent from Figs. 3.3 and 3.4. Here we examine the extent to which lattice trapping plays a role in the fracture of graphene.

Omeltchenko et al. [116] used molecular dynamics to study crack-front propagation in graphene and calculated fracture toughness in terms of a stress intensity factor (note, however, that retention of the REBO cutoff function makes the quantitative aspects of these results questionable). We will calculate the energy release rate, J, and compare it to twice the surface energy density. The difference is indicative of the magnitude of lattice trapping: in the absence of lattice trapping, the energy release rate at the point of fracture should equal twice the surface energy density.

To simulate a crack growth process that matches notions of a crack as closely as possible, we apply a crack-opening displacement to the boundary of a pristine specimen. A QM fragment is placed at the center, surrounded by an MM model as shown in Fig. 3.13. We use a displacement field [99] given by

$$u_x = \frac{K_I}{2\mu}\sqrt{\frac{r}{2\pi}}\cos\frac{\theta}{2}\left[(\kappa-1)+2\sin^2\frac{\theta}{2}\right] \tag{3.5}$$

and

$$u_y = \frac{K_I}{2\mu}\sqrt{\frac{r}{2\pi}}\sin\frac{\theta}{2}\left[(\kappa+1)-2\cos^2\frac{\theta}{2}\right], \tag{3.6}$$

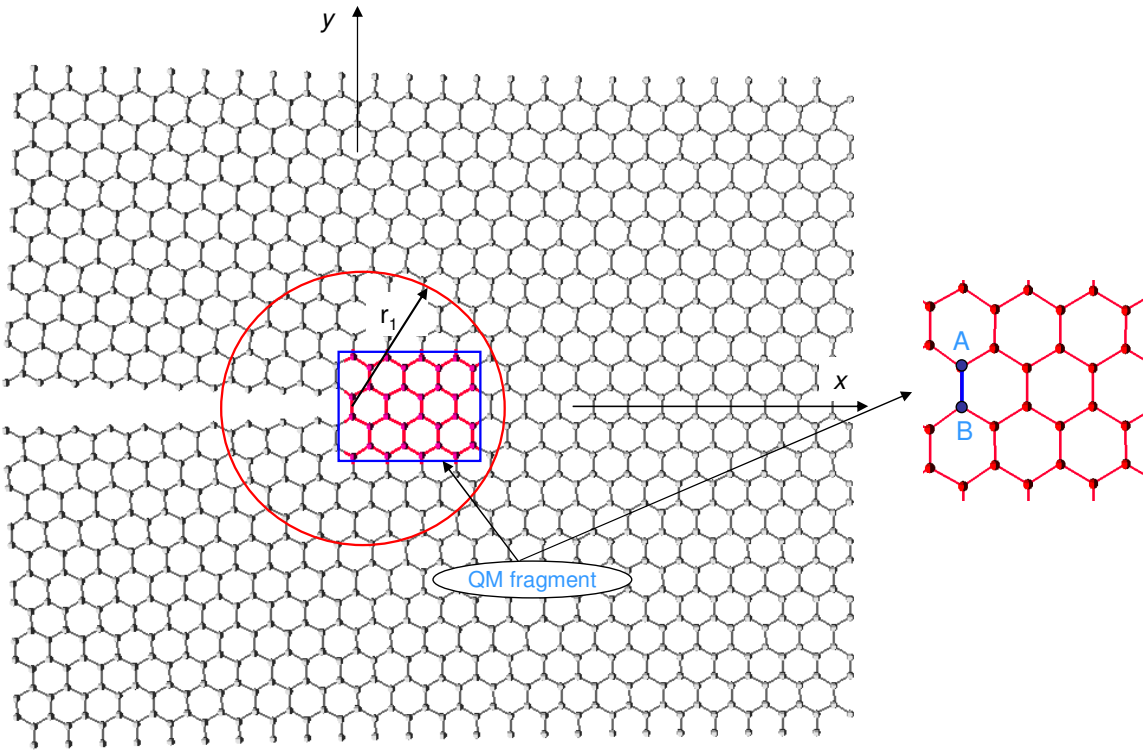

Figure 3.13. A graphene sheet containing a crack. The quantum fragment is shown in the inset. The bond A-B forms the crack tip. Note that r_1 is large enough to enclose the quantum fragment.

where u_x and u_y are the displacements in x and y directions, respectively, μ is the shear modulus of the material [which can be expressed in terms of Young's modulus, Y, and Poisson's ratio, ν, as $\mu = Y/2(1+\nu)$], θ and r are the cylindrical coordinates measured from the crack tip and $\kappa = (3-\nu)/(1+\nu)$ for plane stress. The appropriate continuum model for a monolayer graphene sheet is a state of plane stress.

The parameter K_I, which corresponds to the mode I stress intensity factor, is then incremented until a crack develops along the segment $x < 0$, see Fig. 3.13. An interesting feature of this loading is that because of its antisymmetry the bonds are

broken sequentially in order of increasing x. Thus, the crack grows from left to right, and for sufficiently large K_I all bonds for $x < 0$ break.

We calculated the energy release rate by a discrete form of the energy release [117] integral (a domain form of the Rice J integral [89]);

$$J = \int_{S_0} \sum_{i,j}^{2} \left[\left\{ W\delta_{1j} - P_{ij} \frac{\partial u_i}{\partial X_1} \right\} \frac{\partial q}{\partial X_j} \right] dS, \tag{3.7}$$

where W is the strain energy density, $\mathbf{P}$ is the first Piola-Kirchhoff stress tensor, $\mathbf{u}$ is the displacement field, $\mathbf{X}$ are the material coordinates, S_0 represents the undeformed area of the domain, δ is Kronecker delta and

$$q = \begin{cases} 0 & : \quad r = r_1, \\ 1 & : \quad r = r_2, \\ (r - r_1)/(r_2 - r_1) & : \quad \text{otherwise}, \end{cases} \tag{3.8}$$

where r_1 and r_2 are as shown in Fig. 3.14. The discrete form of Eq. (3.7) (the form for small displacements reported previously [118, 119]) is given by

$$J = \sum_{\alpha \in S_0} \sum_{i,j}^{2} \left[\left\{ W^{\alpha}\delta_{1j} - P^{\alpha}_{ij} \frac{\partial u_i(\mathbf{X}_\alpha)}{\partial X_1} \right\} \frac{\partial q(\mathbf{X}_\alpha)}{\partial X_j} \right] S_0^{\alpha}, \tag{3.9}$$

where S_0^{α} is the initial undeformed area occupied by the atom α, $\mathbf{X}_\alpha$ is the initial position of atom α, W^{α} is the local strain energy density at any atom α which is calculated by the

expression

$$W^{\alpha} = \int_0^{\epsilon_{ij}} \sum_{i,j}^{2} P_{ij}^{\alpha} d\epsilon_{ij}^{\alpha}, \tag{3.10}$$

and the stress at the atom α ($\mathbf{P}^{\alpha}$) is calculated by the virial stress definition [120]

$$\mathbf{P}^{\alpha} = \frac{1}{2\Omega_{\alpha}} \sum_{\beta \neq \alpha} \mathbf{r}^{\alpha\beta} \otimes \mathbf{f}^{\alpha\beta}, \tag{3.11}$$

where $\mathbf{r}^{\alpha\beta}$ is a vector joining atoms α and β, $\mathbf{f}^{\alpha\beta}$ is the force applied on atom α by atom β, and $\Omega_{\alpha} = S^{\alpha}t$ is the volume occupied by atom α, where S^{α} is the area occupied by the atom α in the current configuration. S^{α} is obtained by dividing the current area of the domain by the number of atoms in the domain. The virial stress definition for angle bending has been derived in Zhang et al. [27] The strain ϵ_{ij}^{α} in Eq. (3.10) and $\partial u_i/\partial X_1$ in Eq. (3.9) were obtained by a moving least square fit to the displacement field [27, 64]. Since it is difficult to calculate the bond forces in the QM fragment, we used a domain that lies entirely in the MM region, as shown in Fig. 3.13, to calculate the J-integral.

The results are summarized in Table IV. It can be seen that the difference between the J-integral and twice the surface energy density is only modest for QM/MM calculations using DFT, suggesting a moderate amount of lattice trapping. For the QM(DFT)/MM model $J_{\mathrm{IC}}/2\gamma$ differs from unity by 10%, for the QM(PM3)/MM model and the MM model, this value is 18% and 10%, respectively. These differences between the energy release rates and 2γ are marginally significant, as the resulting fracture stresses

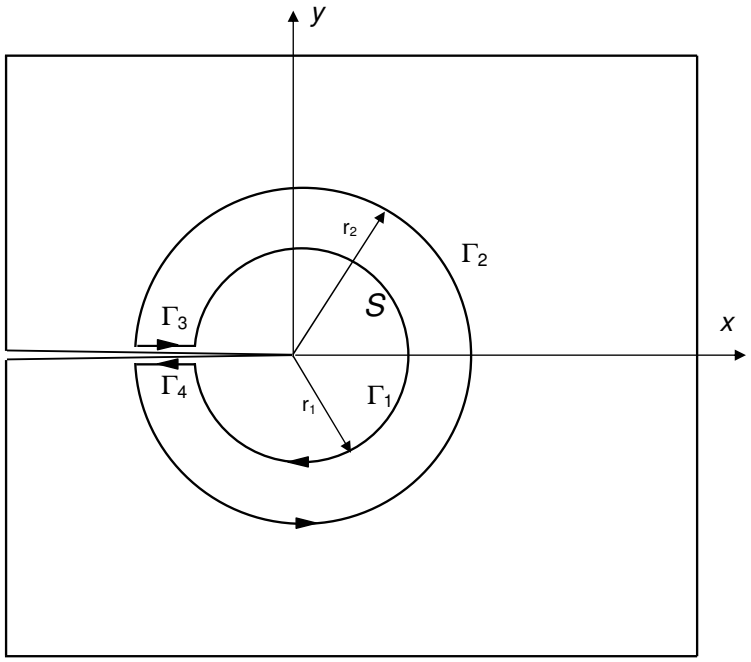

Figure 3.14. Closed contour around a crack tip.

Table 3.4. Critical energy release rate compared to twice the surface energy density for graphene strained in a direction perpendicular to the zigzag edge. All the values are in J/m^2. The scaling factor used for the MM potential is given in the square brackets.

Method	J_{IC}	2γ	$J_{\mathrm{IC}}/2\gamma$
QM(DFT)/MM[1.2]	14.5	13.2	1.1
QM(PM3)/MM[1.4]	15.8	13.4	1.2
MM[1.2]	13.0	11.8	1.1
MM[1.4]	15.1	13.7	1.1
MM	10.8	9.8	1.1

only change by $\sqrt{J/2\gamma}$. Bernstein and Hess [88] have previously reported $J/2\gamma$ values between 1.19 and 1.35 for silicon (which has similar chemical bonding to that of carbon) when the interactions are calculated via tight binding and much larger values for empirical potentials.

3.5. Concluding Remarks

We have studied the impact of large defects on the strength of carbon nanotubes using a coupled QM/MM method. Both slit-like defects and holes were considered. We found that the strengths of CNTs did not depend strongly on the shape of the defects, i.e., the strengths of CNTs with slit-like and hexagonal hole defects of the same size index are comparable while those with rounder holes were about 40% stronger. This contrasts markedly with the effects of holes and cracks at the macroscale, where the cracks have far more deleterious effects on strength than holes.

Comparison of the fracture strengths with the Griffith formula for slits in a finite graphene sheet shows reasonable agreement (within 10% for the longest cracks we calculated). This is somewhat surprising since the stress-strain law is quite nonlinear and the Griffith formula assumes linear material response. The results indicate that continuum fracture mechanics is applicable to crack-like defects as small as 10 Å. Furthermore, they do not indicate any flaw tolerance to nanoscale (5-20 nm) defects: for any defect, the strength is below the theoretical strength, as would be expected.

Crack-like defects, which we called slits, were constructed by removing four rows of carbon atoms in the zigzag CNTs and by removing three rows of carbon atoms in the armchair CNTs. The resulting dangling bonds were capped with hydrogen atoms. This is to be contrasted with crack models based on omitting bonds between adjacent atoms in MM calculations, which are pervasive in the literature. Such defects cannot exist in electronic structure models because interactions between nearby atom pairs cannot simply

be neglected at moderate distances. Thus, the ability of such schemes to accurately model crack behavior is questionable. Crack-like defects can be formed by displacing a lattice according to the asymptotic near-field of elastic fracture mechanics, as we reported in Section 3.4. However, such cracks will not exist in a solid in a stress-free state.

To ascertain the magnitude of lattice trapping in graphene, we computed the energy release rate using a discrete J-integral and compared it to twice the surface energy density, 2γ. These results indicate a modest amount of lattice trapping; the energy release rate calculated by DFT for a graphene sheet at fracture exceeds 2γ by 10%.

The coupled QM/MM calculations were performed with the ONIOM methodology. We checked the accuracy of the method by performing a series of calculations for small defects with QM fragments of increasing size. The resulting stress-strain curves agreed closely over most of the range even for relatively small QM fragments. The fracture stresses and strains also appear to converge, but are more sensitive to the QM fragment size and even for the largest two fragments studied, the fracture stresses and strains differed from the pure QM results by 4% and 8%, respectively, for a [10,0] CNT with a two-atom vacancy defect. Thus, the absolute accuracy of the coupled QM/MM calculations for the failure stress is probably only a few percent and the results are more useful for comparing defects of various sizes than in obtaining quantitative values of failure stresses.

We introduced a simple scaling scheme to improve the compatibility of the MM and QM models. If the MM interaction potential is used unscaled, mismatches between the stiffness and strength of the MM and QM subdomains result in highly spurious behavior.

Comparisons of the QM/MM calculations with MM calculations using the scaled potential show good agreement for the failure stresses and stress-strain curves. In most cases, the differences were less than 15%, and the qualitative pattern of dependence on defect size agreed well. It should be noted that this good agreement is only achieved for the scaled MM potential. The details of the fracture processes predicted by the QM/MM method and the MM method differ significantly. For example, QM/MM calculations show significantly more elongation of the bond at the crack tip.

The results provide further credence to the hypothesis [4] that large defects such as holes are the reason behind the low CNT fracture strengths observed in some experiments [2]. Although the QM/MM models predict failure stresses that are about 40% higher than unscaled MM results modeled previously [4, 3], they are still in the range observed in the Yu et al. experiments [2].

CHAPTER 4

Coupled quantum mechanical/ molecular mechanical/ continuum mechanical models applied to large defects

4.1. Introduction

Even for nanostructures, quantum mechanical/molecular mechanical (QM/MM) methods can be exorbitantly expensive, particularly for large defects. This often precludes the extensive studies required to obtain a full understanding of a system's behavior. An obvious way to avoid these difficulties while minimizing the computational cost is to model the areas where bonds break by a QM method and the molecular mechanical (MM) methods and the remainder with the continuum mechanical (CM) methods. While the QM model often must extend significantly beyond the domain of bond breaking, the resulting QM/MM models apply the QM method in much smaller domains than would be required for strictly QM models. However, the MM methods are unable to take advantage of the reduced spatial resolution requirements far from defects; so coupled quantum mechanical/continuum mechanical (QM/CM) or QM/MM/CM models are often advantageous.

In a coupled QM/MM or QM/MM/CM calculation, the bond-breaking region is modeled by a QM method and MM and/or CM models are used elsewhere. However,

for a covalent system, wherever the QM/MM interface intersects chemical bonds, special treatment is required, as this results in dangling bonds. The most prevalent way to treat this is the link atom approach [34, 33, 29, 32, 35, 121, 36], where the valencies of the interface atoms are saturated by adding hydrogen atoms or pseudo-halogen atoms. Other schemes such as hybrid orbital methods [38, 40, 39, 41, 42, 43, 44, 37] have also been used.

In QM/MM methods employing link atoms, the system is often divided into disjoint MM and QM subdomains. However, when calculating mechanical properties this can lead to substantial errors because the interactions between the subdomains are then determined by artificial forces that do not reflect the true properties of the system. These difficulties may be ameliorated by coupling approaches that overlap the subdomains. A widely-used QM/MM scheme, the ONIOM method [32], involves full overlap between the MM and QM subdomains. In such a model, the MM calculations are performed over the entire system and for a critical subdomain the MM energy and forces are replaced by the QM energy and forces. This necessitates the availability of an MM potential for all chemical interactions in the system, even those treated quantum mechanically. An appropriate MM potential may not be available for systems such as functionalized nanotubes and graphene sheets [122, 123, 124, 125, 81] and therefore this is a severe limitation. Here we describe a quantum to molecular mechanical overlapping domain (QtMMOD) method, which only requires a partial overlap between the MM and the QM subdomains. This method allows treatment of crucial regions strictly by QM methods.

We also describe a multiscale molecular mechanical /continuum mechanical (MM/CM) coupling method, known as the bridging domain method [16, 126], which couples a finite element model with an atomistic model using Lagrange multipliers. Extensive work has been done in developing coupling schemes that link atomistic models with macroscopic models. Abraham et al. [14] and Rudd et al. [15] have presented methods based on a "handshake" domain. In the handshake domain the energy is equipartitioned among the overlapping models; however, the treatment of the constraints, which was not described, includes a coupling energy. Xiao and Belytschko [16], in their development of the bridging domain method, showed that if the coupling is by a Lagrange multiplier method, then the corresponding coupling energy must vanish. The bridging scale methods [127, 20, 19], homogenization method [128], and blending forces coupling methods [129] are some of the other methods developed to couple molecular mechanics(dynamics) with continuum mechanics(dynamics).

The bridging domain method is an overlapping domain decomposition method where compatibility between the coupled models is enforced by Lagrange multipliers in the overlapping or "handshake" domain. A similar method is the Arlequin method[58], which also uses Lagrange multipliers but includes their derivatives in the coupling. In both the Arlequin method and the bridging domain method, the Lagrange multiplier fields are stable. Guidault and Belytschko [130] have shown that one can achieve stability in the bridging domain method if the weighting is continuous. Here we will study the effects of

various types of weight functions in the bridging domain method on the accuracy of the coupled calculations.

In this chapter, we review several methods for coupled QM/MM and coupled QM/MM/CM calculations and we describe a new method, QtMMOD. Furthermore, we show how a QM model can be linked directly to a continuum model and give some illustrations of the performance of such coupling methods. The accuracy of the methods is illustrated for calculations of the mechanical properties of graphene sheets, a system that has generated considerable interest due to its remarkable mechanical and electrical properties [131, 132, 133].

We also describe an extension of an atomistic strain calculation method based on the moving least squares (MLS) [65, 64] method that can be applied to problems with discontinuous strains, such as interfaces. In various applications such as quantum dots [134, 135, 136, 137, 138, 139, 140], in the calculation of J-integral [13, 119], etc., a calculation of the atomistic strain field is required. Faux et al. [141] used a small strain definition to calculate the measure of deformation, which has been used in various calculations on quantum dots [134, 135, 136, 137, 138, 139, 140]. However, for large strains this strain definition does not remain valid and the Green strain is more appropriate. Mott et al.[59] used Voronoi tessellations and Delaunay polygons to calculate Green strain in glass. Jin and Yuan [119] used a simple definition of displacement derivatives which can be used to calculate Green strains, and Li [142] used a least squares scheme to calculate a deformation gradient which can be used to calculate strain.

Zhang et al. [126] introduced an MLS method [65, 64] to compute atomistic strain. This method provides a strain field in the atomistic domain, rather than just the discrete values at nuclei provided by the other methods mentioned above. It was shown [126] that the MLS method provides the exact strain for a linear displacement field when a linear basis is used. Similarly, a quadratic basis can be used to calculate exact strains for a quadratic displacement field. In this article, we extend the MLS method to discontinuous strain fields. This is accomplished by adding to the basis the absolute value of the level set function that describes the interface. We illustrate the method for calculations of a rectangular slab that consists of two different materials under uniform tension.

This article is organized as follows. In Section 4.2, we explain the ONIOM and QtMMOD methods and a QM/CM coupling method based on QtMMOD. The bridging domain method and the MLS strain calculation method are also explained in Section 4.2. In Section 4.3 we present the results obtained from various calculations, and in Section 4.4 conclusions are given.

4.2. Method

4.2.1. Coupling schemes

In this section, we present several coupling methods for QM/MM/CM models and several subsets of such models. For clarity, we first describe the two methods for coupling a QM model with either an MM model or a CM model. Then we describe a methodology for full QM/MM/CM coupled models. The schemes described here are for the determination

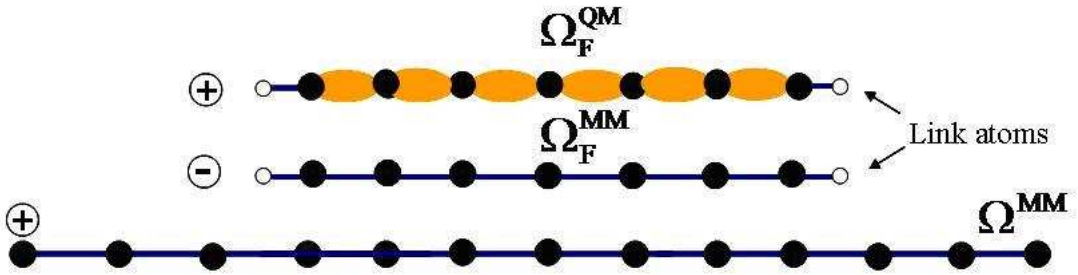

Figure 4.1. One-dimensional representation of the ONIOM model. The circled signs indicate the sign of the associated term in the energy expression.

of equilibrium solutions, so the molecular model is at 0 K and the finite element models for the continuum mechanics are static models. While such solutions sometimes fail to reproduce important phenomena, they are very useful in establishing the equilibrium landscape of a system. In many cases, even phenomena at high temperatures can be predicted quite well by such 0 K equilibrium solutions.

The first scheme we will consider for coupling a QM domain with an MM or a CM domain is a two-level ONIOM [32] method. The basic idea of the ONIOM scheme is applied to QM/MM coupling as shown in Fig. 4.1: 1) the low-order inexpensive model, in this case the MM model, is applied to the entire domain, which in this model is denoted by Ω^{MM}, 2) the higher-order expensive and more accurate model, in this case the QM model, is applied to a subdomain, $\Omega_{\mathrm{F}}^{\mathrm{QM}}$, (sometimes referred to as a QM fragment) where it is needed, in this chapter the region of the model where bond breaking is expected, 3) to cancel the effect of the complete MM model where it is overlapped by the QM model, the energy of the superposed "fictitious" MM fragment $\Omega_{\mathrm{F}}^{\mathrm{MM}} = \Omega_{\mathrm{F}}^{\mathrm{QM}}$ is subtracted. Note

that the difference between the QM and MM energies of the fragment domain is usually thought of as a higher-order correction to the behavior of the system calculated at the lower level of theory.

The total energy of the system is then given by

$$E(\{\mathbf{x}_I\},\{\mathbf{c}_\alpha\}) = E^{\mathrm{MM}}(\{\mathbf{x}_I\}) + E_{\mathrm{F}}^{\mathrm{QM}}(\{\mathbf{x}_I\},\{\mathbf{c}_\alpha\}) - E_{\mathrm{F}}^{\mathrm{MM}}(\{\mathbf{x}_I\}), \tag{4.1}$$

where E^{MM} is the MM energy of the entire system, $E_{\mathrm{F}}^{\mathrm{QM}}$ is the QM energy of the "fragment," i.e., the subdomain for which a higher-level treatment is desired, $E_{\mathrm{F}}^{\mathrm{MM}}$ is the MM energy of the fragment, $\{\mathbf{x}_I\}$ is the set of coordinate vectors of the atoms, where I=1 to N, the number of atoms in the domain of interest, and $\{\mathbf{x}_I\}$ is the set of basis function coefficients used in the representation of the electronic wave function. The portion of the MM model in the lowest layer that overlaps the QM domain in Fig. 4.1 is also fictitious. By subtracting the energy of the fictitious superposed domain [the third term in the right hand side of (4.1)], the energy of the fictitious part in the lowest layer is canceled. Note that the atomic positions used in calculating the energies of the QM and both MM models, $\{\mathbf{x}_I\}$, are identical.

Wherever the QM/MM interface intersects covalent bonds the resulting dangling bonds are saturated by hydrogen link atoms (in both the MM and QM calculations). The link atoms are positioned so that they lie on the line connecting the two former bonding

partners. The distance between any link atom and its bonding partner is commonly taken to be that of a typical equilibrium separation.

Whenever a QM/MM or QM/QM multiscale scheme is used to partition a system into subdomains, sources of error are introduced due to boundary effects such as the use of link atoms and domain-size effects in the QM treatments. In unfavorable cases these errors can be so large that it is better to use only the lower-level treatment on the unpartitioned domain rather than a multiscale approach[143]. One advantage that the ONIOM approach has over disjoint partitioning schemes is that the effects of these complications may partially cancel if the consequences are sufficiently similar with the higher-level and lower-level treatments. In the limit that the higher-level and lower-level treatments are identical, the boundary and domain-size effects associated with domain partitioning vanish in the ONIOM scheme whereas they persist in a disjoint coupling scheme. The cost associated with applying the lower-level treatments on the additional fictitious domains needed in the ONIOM scheme are typically quite small, especially when compared to the benefits that may result from this potential cancelation of errors.

The QtMMOD [144] method was developed for coupled calculations in systems for which it is desirable to treat part of the material strictly by QM methods, such as when reliable empirical potentials are not available to describe the chemical interactions in part of the domain. In the QtMMOD method, as shown in Fig. 4.2, the QM model is used in the interesting area but the underlying MM model is not used for the entire system, but only on a subdomain Ω^{MM} that excludes the interesting region. The MM model is

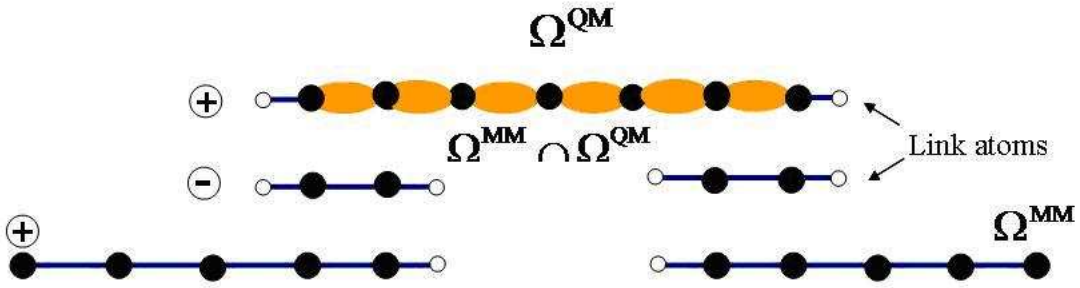

Figure 4.2. One-dimensional representation of the QtMMOD model. The circled signs indicate the sign of the associated term in the energy expression.

coupled to the QM model only through a small overlapping domain. The total energy of the system is then the sum of the QM energy E^{QM} of the subdomain Ω^{QM}, which requires more accurate treatment, and the MM energy E^{MM} of the subdomain Ω^{MM} , where MM calculations are accurate enough, minus the MM energy $E_{\mathrm{O}}^{\mathrm{MM}}$ of the overlapping domain ($\Omega^{\mathrm{MM}} \bigcap \Omega^{\mathrm{QM}}$),

$$E(\{\mathbf{x}_I\},\{\mathbf{c}_\alpha\}) = E^{\mathrm{QM}}(\{\mathbf{x}_I\},\{\mathbf{c}_\alpha\}) + E^{\mathrm{MM}}(\{\mathbf{x}_I\}) - E_{\mathrm{O}}^{\mathrm{MM}}(\{\mathbf{x}_I\}), \tag{4.2}$$

As in the ONIOM scheme, hydrogen link atoms are added to the dangling bonds of the QM model, MM model, and the overlapping domain. The link atoms are not part of the geometry optimization; their positions are obtained from the positions of the two atoms joined by the covalent bonds that have been cut by the interfaces.

An analog of the QtMMOD scheme (denoted QtCMOD) can be employed to couple a QM model to a finite element CM model by replacing the MM model of the QtMMOD

scheme with a finite element model. However, for the purpose of developing a QM/CM coupling in multi-dimensions, the CM domain must be carefully defined. The boundary of the CM domain should correspond to a line (in two dimensions) or a surface (in three dimensions) that crosses the nuclei at the edge of the QM domain. In the simplest form of such a coupling, the nuclei should correspond to the nodes of the finite element mesh in the overlapping domain when the QtMMOD scheme is used.

Let the undeformed reference configuration of the continuum domain be denoted by Ω_0^{CM} and the overlaid CM domain by Ω_0^{CMO}. We denote the motion of the material in the CM domain by $\boldsymbol{\varphi}(\mathbf{X})$, where $\mathbf{X}$ represents the material coordinates.

The energy of the quantum to continuum mechanical overlapping domain (QtC-MOD) model is then given by

$$E(\{\mathbf{x}_I\},\{\mathbf{c}_\alpha\},\boldsymbol{\varphi}(\mathbf{X})) = E^{\mathrm{QM}}(\{\mathbf{x}_I\},\{\mathbf{c}_\alpha\}) + E^{\mathrm{CM}}(\boldsymbol{\varphi}(\mathbf{X})) - E^{\mathrm{CMO}}(\boldsymbol{\varphi}(\mathbf{X})), \tag{4.3}$$

where E^{CM} is a functional of the motion $\boldsymbol{\varphi}(\mathbf{X})$ that corresponds to the energy of the classical subdomain and E^{CMO} is the energy functional of the overlapping domain:

$$E^{\mathrm{CM}}(\boldsymbol{\varphi}(\mathbf{X})) = \int_{\Omega_0^{\mathrm{CM}}} W(\mathbf{F}(\mathbf{X}))\mathrm{d}\Omega_0, \tag{4.4}$$

$$E^{\mathrm{CMO}}(\boldsymbol{\varphi}(\mathbf{X})) = \int_{\Omega_0^{\mathrm{CMO}}} W(\mathbf{F}(\mathbf{X}))\mathrm{d}\Omega_0, \tag{4.5}$$

where W is the strain-energy density function, and the deformation tensor $\mathbf{F}$ is given by

$$\mathbf{F} = \frac{\partial \boldsymbol{\varphi}}{\partial \mathbf{X}} \tag{4.6}$$

The discretization of this model is described later.

The initial link atom position in this method may be chosen based on the lattice structure of the material. For example, for a graphene sheet a bulk carbon atom is bonded to three atoms in a hexagonal lattice structure. The interface atoms are chosen so that they are bonded to two carbon atoms of the atomistic subdomain and the positions of the link atoms are obtained based on the equilibrium hydrogen-carbon bond length and hexagonal lattice structure. Subsequently, the link atom positions are obtained by the finite element interpolants of the displacement.

The previously discussed coupling schemes can be generalized to a QM/MM/CM method as follows. Suppose that we have a CM model for the domain Ω_{C} and an MM model is to be used for a fragment Ω_{M}. The boundary of the domain Ω_{M} should lie on the atoms so that there is no ambiguity about the energy apportionment and Ω_{M} should

overlap Ω_{C}. Quantum mechanics is used in a domain Ω_{Q} that is chosen so that $\Omega_{\mathrm{C}} \bigcap \Omega_{\mathrm{M}}$ does not overlap Ω_{Q}. The energy of the system is then written as

$$
\begin{aligned}
(4.7)\quad E(\{\mathbf{x}_I\},\{\mathbf{c}_\alpha\},\boldsymbol{\varphi}(\mathbf{X})) &= E^{\mathrm{QM}}(\{\mathbf{x}_I\},\{\mathbf{c}_\alpha\}) + E^{\mathrm{MM}}_{\Omega_{\mathrm{M}}}(\{\mathbf{x}_I\}) \\
&\quad - E^{\mathrm{MM}}_{\Omega_{\mathrm{M}} \bigcap \Omega_{\mathrm{Q}}}(\{\mathbf{x}_I\}) + \int_{\Omega_0^{\mathrm{CM}}} w^{\mathrm{C}}(\mathbf{X}) W(\mathbf{F}(\mathbf{X})) \mathrm{d}\Omega_0 \\
&\quad + \sum_{I \in \Omega^0_{\mathrm{C}} \bigcap \Omega^0_{\mathrm{M}}} \int_{\Omega^0_{\mathrm{C}} \bigcap \Omega^0_{\mathrm{M}}} \boldsymbol{\lambda}(\mathbf{X}) \cdot [\boldsymbol{\varphi}(\mathbf{X}) - \mathbf{x}_I] \delta(\mathbf{X} - \mathbf{X}_I) \mathrm{d}\Omega_0,
\end{aligned}
$$

where for a pair-wise potential or quasi-pairwise potential (as in the case of the modified Tersoff-Brenner potential used in some of the calculations presented herein),

$$
(4.8)\qquad E^{\mathrm{MM}}_{\Omega_{\mathrm{M}}} = \sum_{I \in \Omega_{\mathrm{M}}} \sum_{J > I} \left[w^{\mathrm{M}} \left(\frac{1}{2} (\mathbf{X}_I + \mathbf{X}_J) \right) V_{IJ} \right],
$$

where V_{IJ} is the atomistic interaction potential between atoms I and J (which may depend on all the atomistic coordinates), w^{M} and w^{C} are the weight functions for the energies in the domains Ω^0_{M} and Ω^0_{C}, $\mathbf{X}_I$ is the initial position vector of atom I, $\delta(\mathbf{X} - \mathbf{X}_I)$ is a Dirac delta function, and Ω^0_{M} and Ω^0_{C} represent the initial MM and CM subdomains. The last term in the right hand side of (4.7) is used to impose the compatibility between the MM and CM subdomains via the Lagrange multipliers, $\boldsymbol{\lambda}$ [16, 126]. It is required

that $w^{\mathrm{M}} + w^{\mathrm{C}} = 1$, to avoid double-counting of the energies, so $(w^{\mathrm{M}}(\mathbf{X}_I), w^{\mathrm{C}}(\mathbf{X}_I))$ form a partition of unity in the overlapping domain.

The weight functions are given by

$$w^{\mathrm{M}} = 1 - w^{\mathrm{C}} = \begin{cases} 0 & : \text{ in } \Omega^0_{\mathrm{C}}, \\ \text{an increasing function of the distance} & : \text{ from } \Gamma^0_{\mathrm{C}} \text{ to } \Gamma^0_{\mathrm{M}}, \\ 1 & : \text{ in } \Omega^0_{\mathrm{M}} \end{cases} \tag{4.9}$$

where Γ^0_{C} and Γ^0_{M} represent the continuum and molecular boundaries on the MM/CM overlapping domain, respectively. Guidault and Belytschko [130] showed that a continuous weight function is required for such coupling in the bridging domain method because a discontinuous function results in a numerical instability associated with the Lagrange multiplier field. Note that this approach is limited to use with interaction potentials that can be decomposed as in (4.8), so coupling of intrinsically many-body interactions such as those of QM calculations or more-sophisticated empirical potentials directly with a CM model requires a different treatment.

The discretization of models that include a continuum model, such as QtCMOD or QM/MM/CM, is as follows. A finite element method is used for the discretization of the continuum field. The motion $\boldsymbol{\varphi}^e$ for any element e in the finite element model is expressed by

$$\boldsymbol{\varphi}^e(\mathbf{X}) = \sum_I N_I(\mathbf{X})\boldsymbol{\varphi}_I, \tag{4.10}$$

where $N_I(\mathbf{X})$ is the nodal shape function (interpolant) of node I, $\boldsymbol{\varphi}_I$ denotes the current nodal position of node I, and the sum is over all the nodes in the element e. Similarly, the Lagrange multiplier field can be expressed in terms of Lagrange multiplier nodes, $\boldsymbol{\lambda}_I$, and the corresponding interpolants, N_I^λ, (which may differ from the displacement interpolants) as

$$\boldsymbol{\lambda}^e(\mathbf{X}) = \sum_I N_I^\lambda(\mathbf{X})\boldsymbol{\lambda}_I. \tag{4.11}$$

The discrete equations are obtained by finding the stationary points of the energy. For metastable points, the stationary points are local minima; saddle points correspond to the unstable equilibria. The stationary points are found by setting the derivatives of (4.7) with respect to the atomic coordinates, nodal coordinates in the CM domain, and the Lagrange multipliers to zero:

$$\begin{aligned} \frac{\partial E}{\partial \mathbf{x}_I} &= 0, I = 1 \cdots n_{\mathrm{A}}, \\ \frac{\partial E}{\partial \boldsymbol{\varphi}_J} &= 0, J = 1 \cdots n_{\mathrm{C}}, \\ \frac{\partial E}{\partial \boldsymbol{\lambda}_K} &= 0, \alpha = 1 \cdots n_{\lambda}, \end{aligned} \tag{4.12}$$

where n_{A}, n_{C}, and n_{λ} are the total number of atoms, total number of finite element nodes, and the total number of the Lagrange multiplier nodes in the entire domain, respectively. In addition, for the PM3 method considered here the energy must be a stationary point with respect to the basis parameters c_{α}, so

$$\frac{\partial E}{\partial c_{\alpha}} = \frac{\partial E^{\mathrm{QM}}}{\partial c_{\alpha}} = 0. \tag{4.13}$$

The resulting equations are

$$\begin{aligned} \sum_{I \in \Omega_0^{\mathrm{C}} \bigcap \Omega_0^{\mathrm{M}}} \frac{\partial}{\partial \mathbf{X}_I} \Big(E^{\mathrm{QM}}(\{\mathbf{x}_I\}, \{\mathbf{c}_{\alpha}\}) + E^{\mathrm{MM}}_{\Omega_{\mathrm{M}}}(\{\mathbf{x}_I\}) - E^{\mathrm{MM}}_{\Omega_{\mathrm{M}} \bigcap \Omega_{\mathrm{Q}}}(\{\mathbf{x}_I\}) \Big) \\ - \sum_{I \in \Omega_0^{\mathrm{C}} \bigcap \Omega_0^{\mathrm{M}}} \sum_{K=1}^{n_{\lambda}} N_K^{\lambda} \boldsymbol{\lambda}_K = 0, \end{aligned} \tag{4.14}$$

$$\mathbf{f}_J^{\text{int}} + \sum_{K=1}^{n_\lambda} \mathbf{G}_{KJ} \boldsymbol{\lambda}_K = 0, \tag{4.15}$$

$$\sum_{I \in \Omega_0^{\text{C}} \bigcap \Omega_0^{\text{M}}} N_K^\lambda(\mathbf{X}_I) \mathbf{u}_I - \sum_{J=1}^{n_C} \mathbf{G}_{KJ} \mathbf{u}_J = 0, \tag{4.16}$$

where $\mathbf{u}_I$ denotes the displacement of atom I,

$$\mathbf{f}_J^{\text{int}} = \int_{\Omega_{\text{C}}^0} w^{\text{C}}(\mathbf{X}) \frac{\partial W}{\partial \mathbf{F}} \frac{\partial \mathbf{F}}{\partial \boldsymbol{\phi}_J} \text{d}\Omega_0, \tag{4.17}$$

and

$$\mathbf{G}_{KJ} = \sum_{\alpha \in \Omega_{\text{C}}^0 \bigcap \Omega_{\text{M}}^0} N_K^\lambda(\mathbf{X}_I) N_J(\mathbf{X}_I), \tag{4.18}$$

The continuum forces in (4.17) can be expressed in terms of the first Piola-Kirchhoff stress $\mathbf{P}$ by using (see Belytschko et al. [63])

$$\mathbf{P} = \frac{\partial W}{\partial \mathbf{F}}. \tag{4.19}$$

Using the relation

$$\frac{\partial \mathbf{F}}{\partial \boldsymbol{\phi}_J} = \frac{\partial N_J}{\partial \mathbf{X}}, \tag{4.20}$$

(4.17) can be rewritten as

$$\mathbf{f}_J^{\text{int}} = \int_{\Omega_{\text{C}}^0} w^{\text{C}}(\mathbf{X}) \mathbf{P} \frac{\partial N_I}{\partial \mathbf{X}} \mathrm{d}\Omega_0. \tag{4.21}$$

Further details on the MM/CM coupling can be found in Zhang et al. [126].

The above yields a coupled QM/MM/CM model, where the MM domain is coupled to the CM domain using the bridging domain method and the QM domain is coupled to the MM domain using either the ONIOM or the QtMMOD scheme. Applications of this coupled scheme are given in Section 3.

4.2.2. Scaling the MM potential

It was observed in coupled simulations of fracture that for some widely used potentials, the MM model must be scaled so that it matches the QM model over a large range of strains [13]. Otherwise, various types of unphysical phenomena occur which are simply a result of strength and stiffness mismatches between the QM and MM models. For example, if the strength of the MM model is less than that of the QM model, fracture

can occur in the MM subdomain, even if the MM model does not have a defect. Another consequence of such mismatches is that cracks propagating from the MM domain to the QM domain can be deflected back into the MM domain if the QM model is stiffer than the MM model.

To avoid these anomalies, the MM energy was scaled by a factor which varies with the applied strain to match the QM and MM models. This method of scaling was recently developed [145] and it improves the level of agreement between the QM/MM results and pure QM benchmarks. Details of this method are given in the Appendix.

4.2.3. Atomistic strain calculations using MLS

Recently, a moving least squares method for calculating strains in QM and MM models was developed [126]. This method constructs a smooth strain field within the model without recourse to tessellation techniques. It was shown that for a linear basis, this method reproduces the exact constant strain [126], i.e., the atomic positions are given by a linear field. For a quadratic basis, the method computes the correct linear strain field; however, the method encounters significant errors at an interface, as between two materials, because it presupposes a smooth strain field. Here we develop an extension that yields the exact strain even when an interface leads to discontinuous strains. This method is based on Belytschko et al. [146].

Suppose an interface is given by

$$f(\mathbf{X}) = 0. \tag{4.22}$$

For example, for a vertical interface or circular interface

$$f(\mathbf{X}) = X - a;\ \ f(\mathbf{X}) = X^2 + Y^2 - a^2, \tag{4.23}$$

where a is the location of the interface or the radius of inclusion, respectively, and X and Y denote two components of $\mathbf{X}$.

In the MLS approximation, the displacement $\mathbf{u}(\mathbf{X})$ at any point $\mathbf{X}$ is approximated in the domain by

$$\mathbf{u}(\mathbf{X}) = \sum_{i=1}^{m} p_i(\mathbf{X})\mathbf{a}_i(\mathbf{X}), \tag{4.24}$$

where m is the number of terms in the basis, and $p_i(\mathbf{X})$ and $\mathbf{a}_i(\mathbf{X})$ are vector coefficients to be determined as described subsequently. The bases used here are

$$[p_i(\mathbf{X})] = [1, X, Y, |f|] \qquad \text{for a linear basis,} \tag{4.25}$$

and

$$[p_i(\mathbf{X})] = [1, X, Y, X^2, XY, Y^2, |f|] \quad \text{for a quadratic basis,} \tag{4.26}$$

where $|f|$ is the wedge function that adds a discontinuity in the gradient. We note that

$$\mathbf{a}_i = [a_{1i}, a_{2i}] = [a_{xi}, a_{yi}]. \tag{4.27}$$

The coefficients $\mathbf{a}_i$ at any point $\mathbf{X}$ are found by minimizing the weighted L^2 norm $q(\mathbf{X})$ given by

$$q(\mathbf{X}) = \sum_{I \in \mathrm{S}_{\mathbf{X}}} (p_i(\mathbf{X}_I)\mathbf{a}_i(\mathbf{X}) - \mathbf{u}_I)^{\mathrm{T}} w^{\mathrm{MLS}}(\mathbf{X}_I - \mathbf{X})(p_j(\mathbf{X}_I)\mathbf{a}_j(\mathbf{X}) - \mathbf{u}_I), \tag{4.28}$$

where $\mathbf{u}_I = \mathbf{u}(\mathbf{X}_I) = [u_{xI}, u_{yI}]^{\mathrm{T}}$, $w^{\mathrm{MLS}}(\mathbf{X}_I - \mathbf{X})$ is a weight function of compact support, and S_X is the set of atoms within the support of $w^{\mathrm{MLS}}(\mathbf{X}_I - \mathbf{X})$. Note that Einstein notation is used in the above equation, i.e., the repeated indices i and j indicate an implicit summation over these indices. A cubic spline is used here for the weight function

$$w^{\mathrm{MLS}}(r) = \begin{cases} \frac{2}{3} - 4r^2 + 4r^3 & \text{for } r \leq \frac{1}{2}, \\ \frac{4}{3} - 4r + 4r^2 - \frac{4}{3}r^3 & \text{for } \frac{1}{2} < r \leq 1, \\ 0 & \text{for } r > 1, \end{cases} \tag{4.29}$$

where $r = ||\mathbf{X} - \mathbf{X}_I||/R_0$, and R_0 is the radius of the support circle centered at point $\mathbf{X}$.

By minimizing $q(\mathbf{X})$ in (4.28) with respect to $\mathbf{a}_j$, a set of linear equations for $\mathbf{a}_j$ is obtained as

$$M_{kj}\mathbf{a}_j = \mathbf{b}_k. \tag{4.30}$$

where M_{kj} is known as the Gram matrix or the moment matrix and is given by

$$M_{kj} = \sum_{I \in S_{\mathrm{X}}} p_k(\mathbf{X}_I) p_j(\mathbf{X}_I) w^{\mathrm{MLS}}(\mathbf{X}_I - \mathbf{X}), \tag{4.31}$$

and

$$\mathbf{b}_k = \sum_{I \in S_X} p_k(\mathbf{X}_I) w^{\mathrm{MLS}}(\mathbf{X}_I - \mathbf{X}) \mathbf{u}_I. \tag{4.32}$$

For a two-dimensional problem with a linear basis, the above equations lead to two systems of three equations in three unknowns with the same Gram matrix. The deformation gradient $\mathbf{F}$ is then obtained using Eqs. (4.6) and (4.24) and the relation $\boldsymbol{\varphi} = \mathbf{u} + \mathbf{X}$ as

$$\mathbf{F} = \mathbf{I} + \sum_{i}^{m} \frac{\partial (p_i \mathbf{a}_i)}{\partial \mathbf{X}} \tag{4.33}$$

where $\mathbf{I}$ is the identity tensor. The Green strain $\boldsymbol{\epsilon}$ can be calculated by

$$\boldsymbol{\epsilon} = \frac{1}{2}(\mathbf{F}^{\mathrm{T}}\mathbf{F} - \mathbf{I}). \tag{4.34}$$

As we mentioned before, a noteworthy attribute of the MLS strain scheme is that for a linear displacement of the atoms, the MLS strain gives the exact constant strain state. This may be seen as follows. Suppose that the displacements of the atoms are given by

$$\mathbf{u}_I = p_i^{\mathrm{L}}(\mathbf{X}_I)\bar{\mathbf{a}}_i. \tag{4.35}$$

where p_i^{L} is the linear basis with a wedge function and $\bar{\mathbf{a}}_i$ are given coefficients. Then substituting (4.35) into the right hand side of (4.32) and using (4.30) gives

$$M_{kj}\mathbf{a}_j = \mathbf{b}_k = \sum_{I \in \mathrm{S}_X} p_k^{\mathrm{L}}(\mathbf{X}_I) w^{\mathrm{MLS}} p_i^{\mathrm{L}}(\mathbf{X}_I) \bar{\mathbf{a}}_i. \tag{4.36}$$

The right hand side of the above can then be seen as $M_{ki}\overline{\mathbf{a}}_i$ and by comparison with (4.31) it follows that $\mathbf{a}_i = \overline{\mathbf{a}}_i$, if the basis is linear. This is often called a reproducing condition: the MLS strain reproduces the strain associated with any displacements of the atoms derived from a linear field with a discontinuity in the gradient at $f(\mathbf{X}) = 0$, if a linear basis with a wedge function is used.

4.3. Numerical Studies

4.3.1. Fracture of a defected graphene sheet by QM/MM and QM/CM methods

The coupling methods were implemented to couple molecular mechanics using the modified Tersoff-Brenner (MTB-G2) potential or continuum mechanics using a linear elastic finite elements model with quantum mechanics using the semi-empirical method PM3 [147]. MTB-G2 [83, 3, 84, 69] is a modified version of the standard reactive empirical bond order (REBO) [84] potential, in which the cutoff function is removed and interatomic interactions are included only for those atom pairs that are less than 2.0 Å apart in the initial unstrained configuration. This was found [83, 69] to be necessary to prevent spuriously high values of the fracture strength due to the cutoff function.

Three coupling methods were used to calculate the stress-strain curves and fracture stresses of a graphene sheet containing defects. In these calculations, the end carbon atoms of the graphene sheet were displaced with an increment of 0.5% of the sheet length until the sheet fractures. At each strain increment, the sheet configuration was optimized with the carbon atoms at each edge constrained to lie within a plane. Once the geometry was optimized at a given applied strain, the tensile stress in the sheet can be calculated by taking derivatives of the energy using finite differences with respect to the strain. An effective thickness of 3.4 Å was used in the stress calculations; this corresponds to the interlayer spacing in graphite, and is widely used to present the tractions on graphene sheets as stresses.

We first consider a graphene sheet containing an asymmetric two-atom vacancy [4][109]. It was stretched in the direction perpendicular to the zigzag edge. The coupled models of this system for the three coupling methods considered are shown in Figs. 4.3-4.5. The sheet was 27 Å by 21 Å in dimensions and contained 248 carbon atoms with 64 carbon atoms in the QM domain and 38 carbon atoms in the overlapping domain for the QtMMOD scheme. The results were compared to those calculated by pure QM calculations. In addition to the two QM/MM models, a QM/CM model (shown in Fig. 4.3) using triangular elements was also used.

The stress-strain curves for the three methods are shown in Fig. 4.6. The stresses calculated by the QtMMOD and ONIOM coupling methods are almost indistinguishable. The results match quite well with the benchmark pure QM results although there are

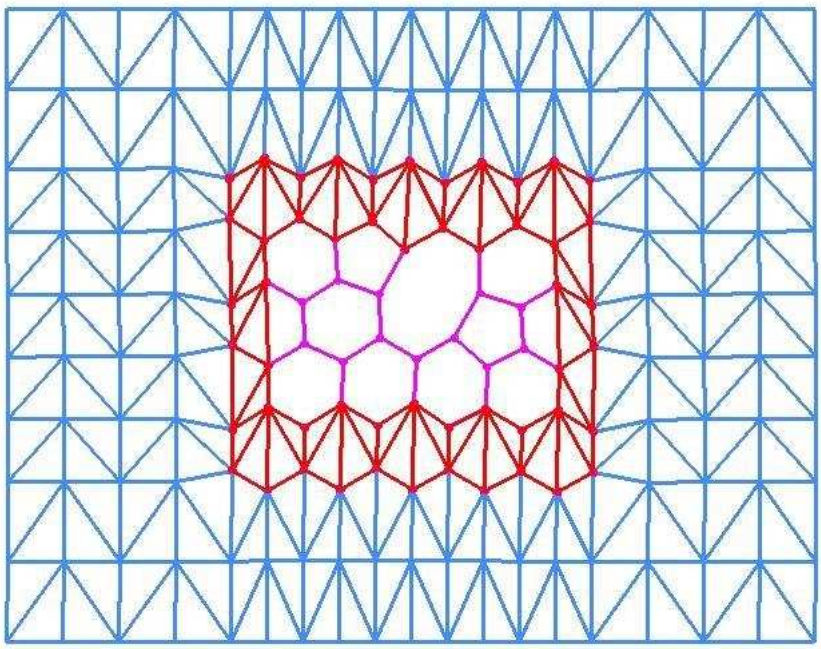

Figure 4.3. A QM/CM model of a graphene sheet containing an asymmetric two-atom vacancy defect. Pink (light, ball and stick) atoms in the center constitute the strictly QM region, red (dark, ball and stick) atoms constitute the overlapping region, and blue (light, stick) region represents the strictly CM region.

small differences near the fracture strain. The QtMMOD and ONIOM methods calculated fracture stress values of 87.4 GPa and 87.2 GPa, respectively, in comparison to 88.1 GPa obtained from the strictly QM calculations. The stress-strain curve for the QM/CM coupled calculations matches the stresses from the other methods quite well and yields a fracture stress value of 87.3 GPa. However, small differences are observed, which may be due to several reasons, such as, the fact that a finite element model does not reflect the physics near the defect as accurately as the MM method. Nevertheless, the QM/CM model is still sufficiently accurate to be useful for studies of large systems, such as calculations

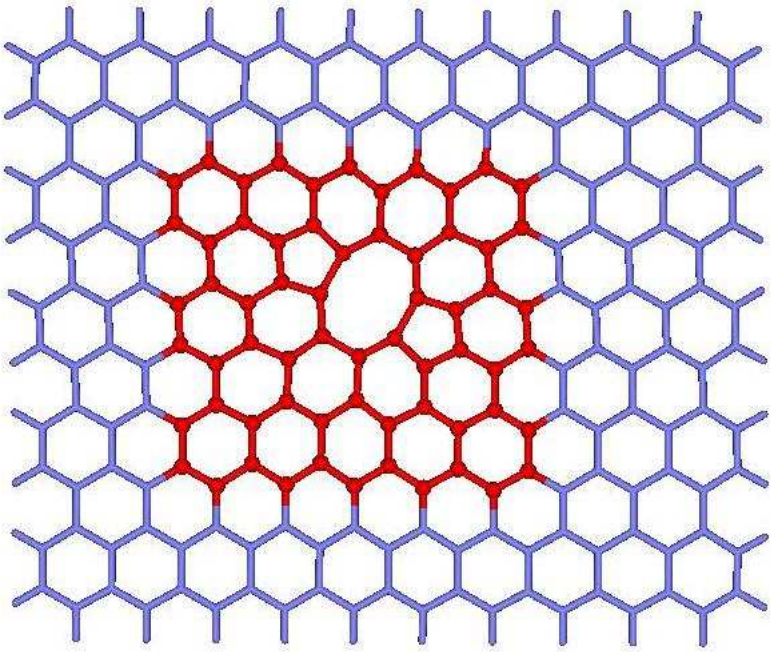

Figure 4.4. An ONIOM model of a graphene sheet containing an asymmetric two-atom vacancy defect. Red (dark, ball and stick) atoms constitute the QM fragment and blue (light, stick) atoms indicate the region treated by MM methods.

of the fracture stress of a graphene sheet containing a crack [13]. In such models, the region near the crack tip can be modeled quantum mechanically and the CM model can be applied elsewhere.

4.3.2. Effect of weight functions on the accuracy of the bridging domain method

Ben Dhia and Rateau [58] and Guidault and Belytschko [130] observed that a discontinuous weight function results in an instability in the Lagrange multiplier in an L^2 coupling. Guidault and Belytschko [130] observed that the instability can be avoided by

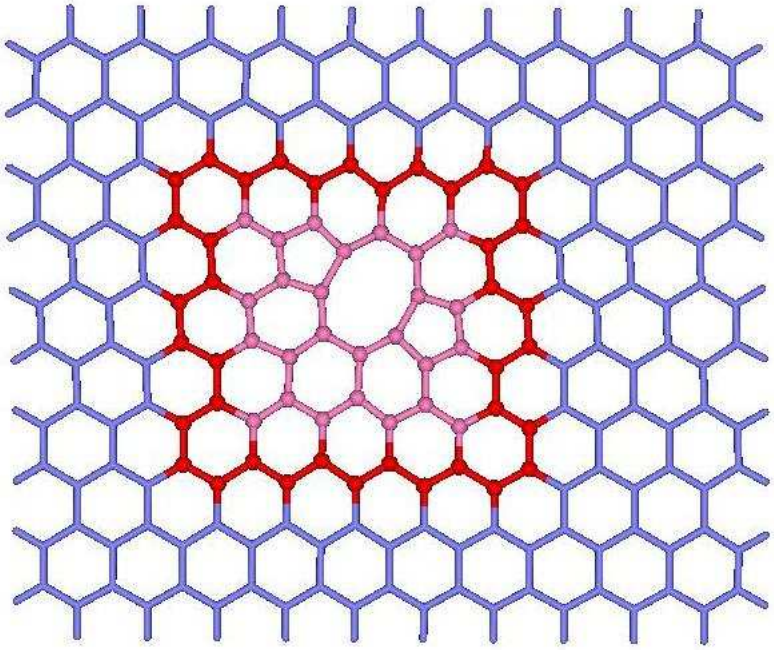

Figure 4.5. A QtMMOD model of a graphene sheet containing an asymmetric two-atom vacancy defect. Pink (light, ball and stick) atoms constitute the strictly QM region, red (dark, ball and stick) atoms constitute the overlapping region, and blue (light, stick) atoms constitute the strictly MM region.

smooth weight functions. Here we consider three weight functions-a discontinuous function, a linear function, and a cubic function, as shown in Fig. 4.7- and we examined the effect of these weight functions on the accuracy of a coupled MM/CM calculation.

A harmonic potential with an angle bending term was used to model the atomistic region (for the details of the potential see Zhang et al. [126]). A linear elastic finite element model was chosen for the continuum region. A graphene sheet, 728 Å x 426 Å in dimensions, was stretched in the direction perpendicular to the zigzag edge. The atomistic region was 323 Å x 190 Å in dimensions and located in the center as shown in

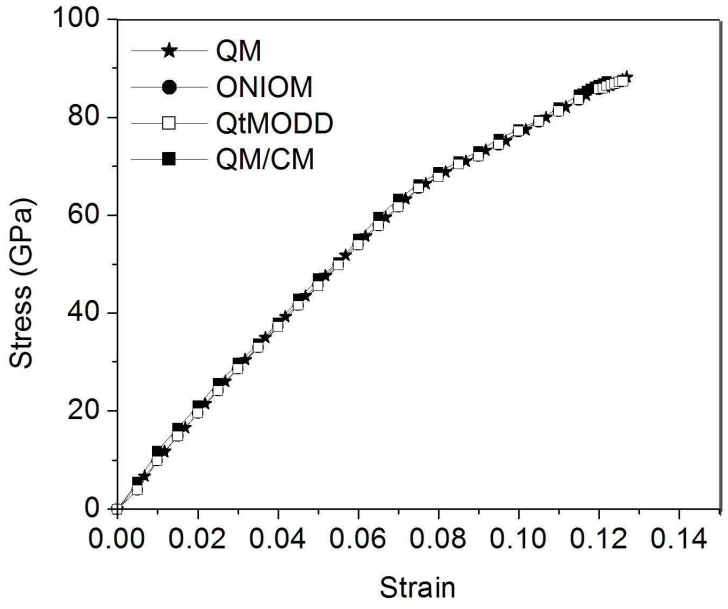

Figure 4.6. Stress-strain curves obtained by the ONIOM, QtMMOD, QM/CM coupling, and pure QM methods for the graphene sheet models shown in Figs. 3-5.

Fig. 4.8. All degrees of freedom of the top and bottom boundary nodes and the x-degrees of freedom of the left and right boundary nodes were fixed. The L^2 norm used to estimate the error is given by

$$\varepsilon_{L^2} = \frac{||\mathbf{d} - \mathbf{d}_{\text{exact}}||}{||\mathbf{d}||} \tag{4.37}$$

where $\mathbf{d}$ is the displacement of an atom or a node calculated using the coupled calculation, $\mathbf{d}_{\text{exact}}$ is the exact solution at that atom or node, and

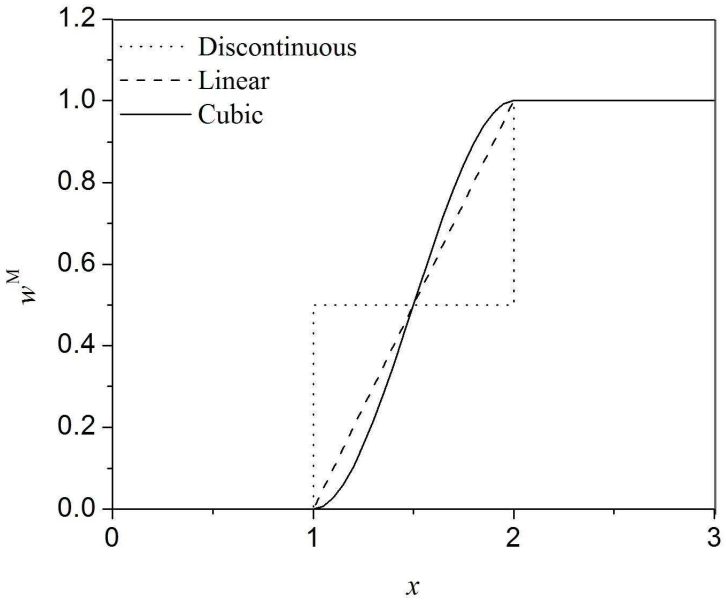

Figure 4.7. A one dimensional representation of the weight function, w^{M}, such that $\Omega_{\mathrm{C}} \in [0, 2]$ and $\Omega_{\mathrm{M}} \in [1, 3]$. Note that $w^{\mathrm{C}} = 1 - w^{\mathrm{M}}$.

$$||\mathbf{d}|| = \left[\sum_I (d_{xI}^2 + d_{yI}^2) \right], \tag{4.38}$$

where d_{xi} and d_{yi} are the x and y components of the displacement of atom or node I and the sum is over all the atoms and finite element nodes.

When a uniform strain of 1% was applied, we observed errors in the L^2 norm of 0.0023, 0.0014, and 0.0019 calculated using the discontinuous, linear, and the cubic weight functions, respectively. Similar trends were observed at higher strains. As expected, the use of a linear weight function gives a small error than the discontinuous weight function.

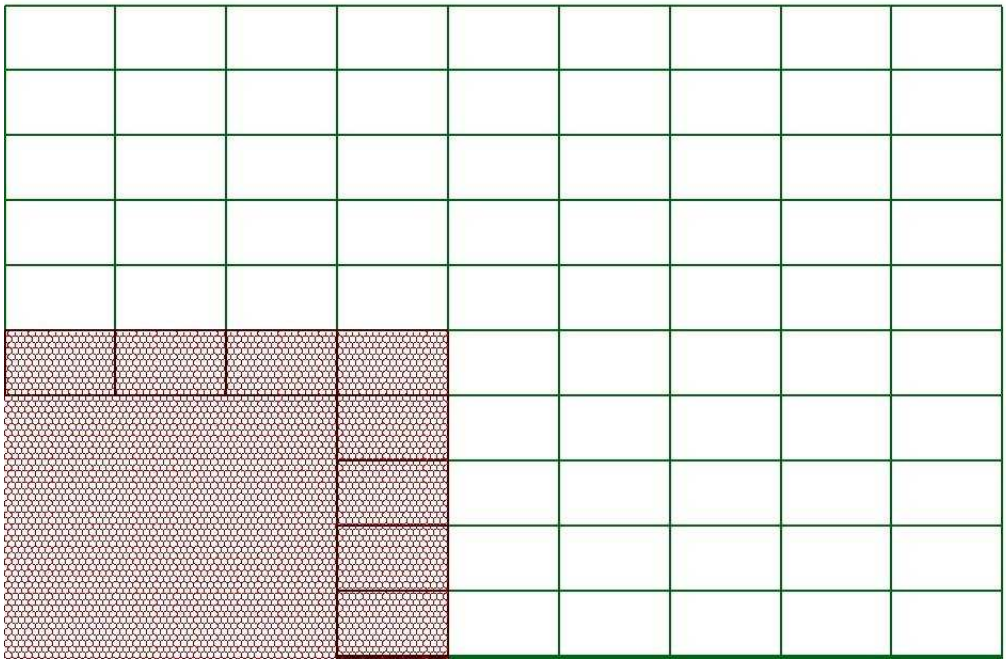

Figure 4.8. Right-top quarter of the MM/CM bridging domain model of a graphene sheet.

The cubic weight function, despite possessing C^1 continuity, gives larger errors than the linear weight function.

4.3.3. Strain calculation using MLS

To illustrate the ability of the extended MLS method to capture the strain discontinuity at interfaces, we applied tensile strain to the sheet shown in Fig. 9. Harmonic potentials with only pairwise interactions were used such that the Young's modulus of the inner material shown in Fig. 9 is twice as large as that of the Young's modulus of the outer material. Because there are two interfaces, the following basis set was used for the displacement

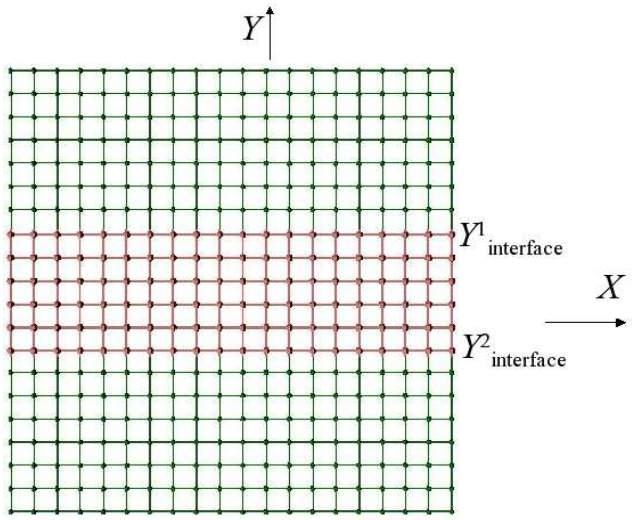

Figure 4.9. The region containing red (dark) atoms has a Young's modulus that is twice as large as that of the region containing the green (light) atoms.

$$[p_i(\mathbf{X})] = [1, X, Y, |Y - Y^1_{\text{interface}}|, |Y - Y^2_{\text{interface}}|], \tag{4.39}$$

where $Y^1_{\text{interface}}$ and $Y^2_{\text{interface}}$ are the Y coordinates of the two interfaces in Fig. 4.9.

The sheet was 27 Å x 27 Å in dimensions. At an applied strain of 3.5%, strain, ϵ_y, calculated with and without the interface terms in the basis along $X = 0$ is compared to the exact strain in Fig. 4.10. It can be seen that without the interface terms the MLS scheme incorrectly smoothens the strain across the interface. With the enhanced basis, the exact strains are obtained at the interface and the discontinuity is captured well.

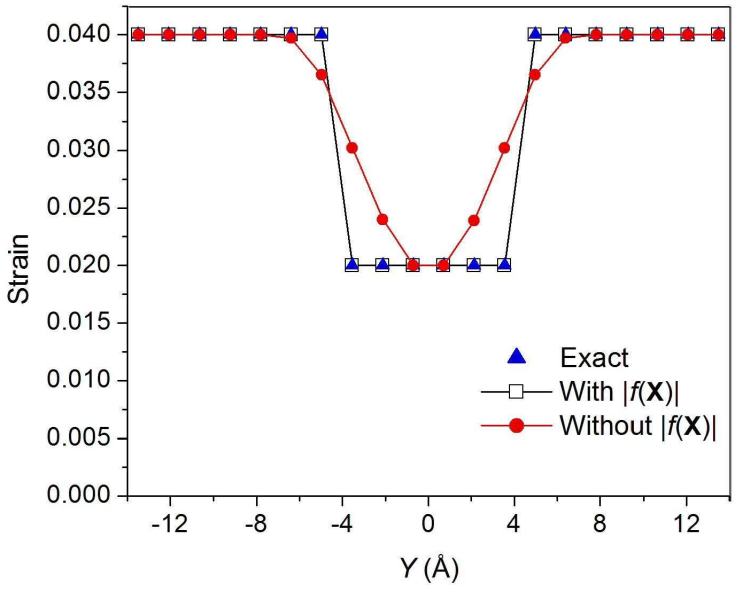

Figure 4.10. Comparison of MLS strain at $X = 0$ with the exact strain at an applied strain of 0.035.

We next illustrate the use of the MLS scheme to calculate the atomistic strain field in a graphene sheet with a crack. To simulate a crack we applied an asymmetric crack-opening displacement (K-field) to the boundary atoms using

$$u_x = \frac{K}{2\mu}\sqrt{\frac{r}{2\pi}}\cos\frac{\theta}{2}\left[(\kappa - 1) + 2\sin^2\frac{\theta}{2}\right] \tag{4.40}$$

and

$$u_x = \frac{K}{2\mu}\sqrt{\frac{r}{2\pi}}\sin\frac{\theta}{2}\left[(\kappa + 1) - 2\cos^2\frac{\theta}{2}\right] \tag{4.41}$$

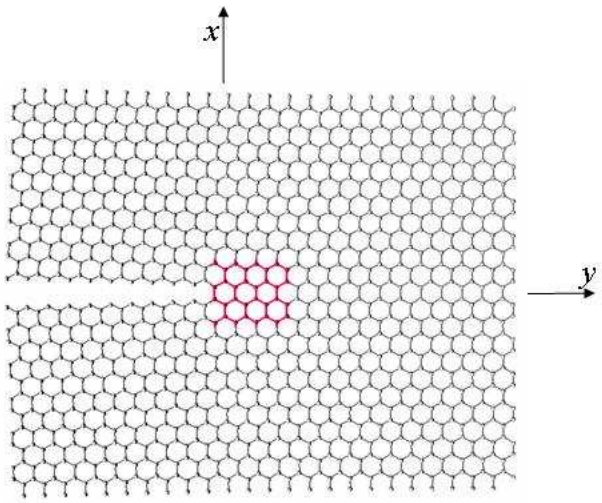

Figure 4.11. QM/MM model of a graphene sheet with a crack. Red (dark) atoms represent the QM subdomain and the Grey (light) atoms represent additional atoms treated at the MM level.

where u_x and u_y are the displacements in the x and y directions, respectively, μ is the shear modulus of the material [which can be expressed as $\mu = Y/2(1+\nu)$, where Y is the Young's modulus and ν is the Poisson's ratio], θ and r are the cylindrical coordinates measured from the crack tip and $\kappa = (3-\nu)/(1+\nu)$ for plane stress.

We used the ONIOM coupling scheme such that the region near the crack tip was modeled by quantum mechanics and the rest of the structure was treated by the MM method as shown in Fig. 4.11. We calculated the strain ϵ_y using the MLS scheme and compared it to the elasticity solution at K = 3 MPa$\sqrt{\text{m}}$, as shown in Fig. 4.12. Reasonable agreement is observed between the elasticity solution and the computed strain. The discrepancies can be explained by the fact that the elasticity solution is not accurate near the crack tip.

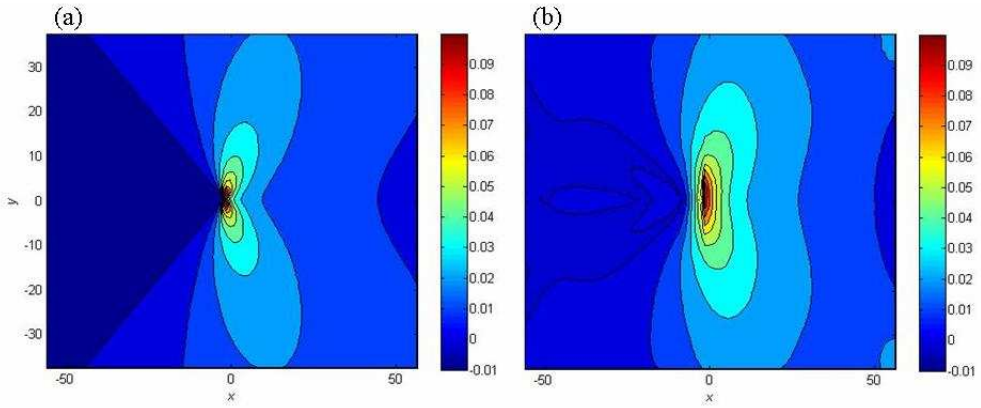

Figure 4.12. ϵ_y obtained from (a) elasticity solution and (b) MLS method for the sheet shown in Fig. 11.

Note that the MM energy was scaled by a constant scaling factor such that the Young's modulus calculated using the MM potential matches the Young's modulus calculated by quantum mechanics for a pristine graphene sheet. Thus for the QM/MM model, the entire sheet had the same Young's modulus and no strain discontinuity is expected at the QM/MM interface.

4.3.4. Comparison of QM/MM/CM computations of fracture strength for graphene sheet with Griffith's formula

In this example we consider the fracture strength of a graphene sheet with slit defects of various lengths and compare the calculated strengths to those predicted by Griffith's formula for a crack in an infinite sheet. Slit defects were created by removing four rows of atoms and then saturating the dangling bonds by hydrogen atoms [13, 3]. In order to be able to compare with the results for an infinite sheet, very large sheets were required,

so we used the QM/MM/CM scheme described earlier, where the QM/MM coupling was obtained by using the QtMMOD scheme and the bridging domain method was used to link the MM model to a finite element model.

A representation of the QM/MM/CM model for one slit size is shown in Fig. 4.13. The dimensions of the full sheet are 393.5 Å by 411.8 Å. The atomistic region is 115.5 Å by 82.3 Å , and located in the center of the sheet. In Fig. 14 the numerical results are compared with the results of the Griffith formula, which is given by

$$\sigma = \sqrt{\frac{2Y\gamma}{\pi a}}, \tag{4.42}$$

where σ is the Griffith formula stress, Y is the Young's modulus, a is the half length of the slit, and γ is the surface energy density. We calculated γ as the difference between the PM3 energy of optimized pristine fragment and the energy of the two resulting fragments after they are fractured along the desired surface, separated to infinity, and subsequently optimized to yield their equilibrium geometries, divided by twice the surface area. The factor of two is included because two surfaces are produced on fracture.

The QM/MM/CM results agree well with the prediction of the Griffith formula and decrease approximately as the inverse of the square root of the crack length. The Griffith stress is a lower bound on the fracture stress, but the approximate stress estimates of the Griffith formula need not be, and as seen in Fig. 4.14 the Griffith formula results

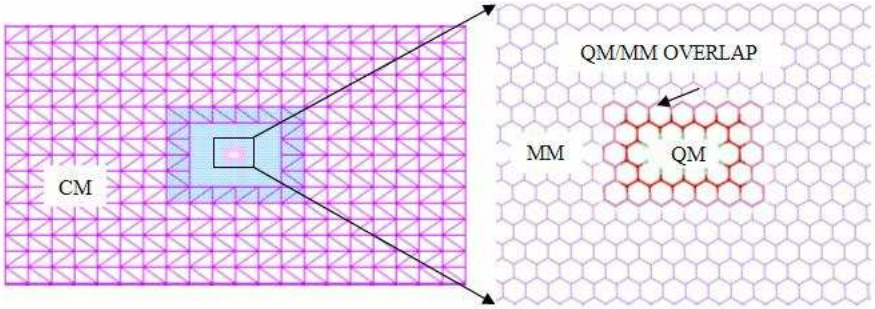

Figure 4.13. QM/MM/CM model of a graphene sheet containing a slit-like defect.

fall below the numerical ones for slits longer than 20 Å. We also observe that the fracture strength decreases sharply from the pristine strength as the slit length increases, which contradicts the hypothesis of Gao et al. [114] that materials are insensitive to defects at the nanoscale.

A similar calculation was reported in Khare et al. [13] but we have here calculated fracture strengths using the QtMMOD method for the QM/MM coupling and a different scaling scheme[145]. The trends are quite similar but the fracture stresses obtained here are slightly different for the same cases.

4.4. Concluding Remarks

We have implemented two general QM/MM coupling methods and one QM/CM coupling method to calculate fracture stresses of a graphene sheet containing an asymmetric two-atom vacancy defect. The results of the two QM/MM coupling methods matched almost perfectly with each other and agreed quite well with the pure QM results. The QM/CM method also shows good agreement with the other two coupling

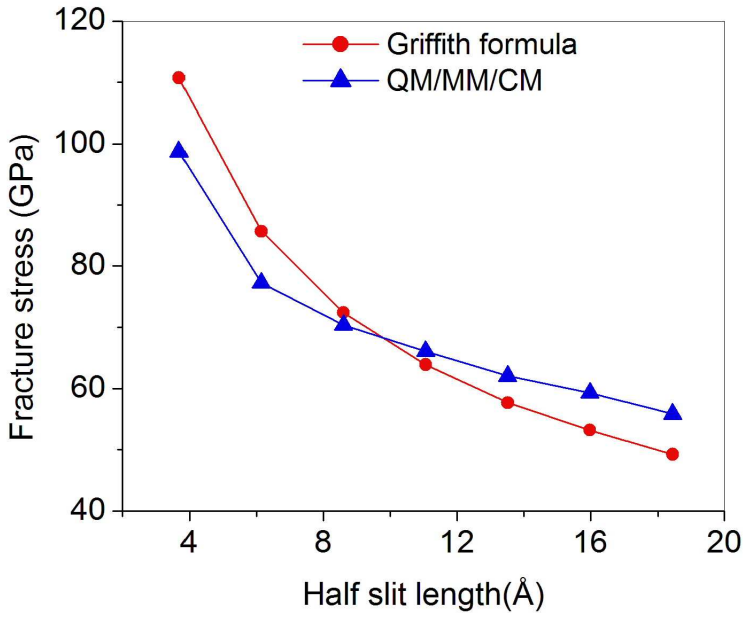

Figure 4.14. Results of the Griffith formula versus QM/MM/CM fracture strengths for a graphene sheet containing a slit-like defect.

methods, although some small differences were observed. The QtMMOD method couples two overlapping domains such that a region is modeled by the QM method only, thus allowing calculations for systems containing defected regions for which no reliable reactive empirical potentials are available. The QM/CM coupling was similar to the QtMMOD method, except that the MM region is replaced by a finite element mesh such that the finite element nodes match the atomic positions in the overlapping domain. This method allows coupled calculations of large systems for which even QM/MM calculations may be too expensive.

We have computed fracture strengths of a graphene sheet containing slit defects using a QM/MM/CM model and observed good agreement with the Griffith formula for a

crack in an infinite sheet. It was also observed that in the presence of defects, the fracture strength decreases sharply and monotonically, which is somewhat in disagreement with the arguments of Gao et al. [114] that materials become defect tolerant at the nanoscale.

We also studied the effect of various weight functions on the bridging domain atomistic/continuum coupling. Linear weight functions give the least error when compared to discontinuous and cubic shape functions in a uniformly strained graphene sheet calculation. The cubic weight functions were better than the discontinuous weight function, but produced larger errors than the linear weight function.

The MLS scheme for strain calculation was tested for several problems. For a graphene sheet with a crack, the strain compares well with the elasticity solution despite the linear stress-strain law in the elasticity solution. The MLS scheme gives the exact strain field for a linear displacement field when a linear basis is used. We also showed that with an additional basis function, the MLS scheme can reproduce the strain discontinuity at interfaces. Moreover, a strain field can be calculated in the entire domain using this method rather than just at the atomic positions.

CHAPTER 5

An XFEM study of dislocations in carbon nanotubes

5.1. Introduction

Brittle fracture of carbon nanotubes (CNTs) had been observed in experiments [2, 148, 149] and extensively studied by theoretical calculations for pristine and defected CNTs [4, 3, 13, 150, 83, 151, 152]. In this mode of failure, bonds near a defect have much higher strains than the region away from the defect [13] and thus these break first leading to the brittle failure of the tube. However, recent experiments at very high temperatures [153, 154] have shown large plastic strains before failure accompanied by kink formation. Single-walled carbon nanotubes (SWCNTs) were seen to be deformed plastically when stretched in a transmission electron microscope at 2000 ^{o}C and showed a 280% tensile elongation and a 15-fold diameter reduction.

Nardelli et al. [155] proposed a plastic failure mechanism for CNTs based on dislocation motion [156]. It was suggested that a Stone-Wales defect [97], which is a two pentagon and two heptagon pair defect (5-7-7-5), can be seen as a pair of dislocations or a dislocation dipole, as shown in Fig. 5.1. Under tension and at high temperatures these dislocation pairs glide away from each other, which changes the chirality of the tube causing the diameter to decrease and the length to increase. However, this mechanism

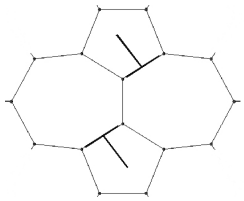

Figure 5.1. Stone-Wales defect can be seen as a pair of dislocations, where each 5-7 pair represents a dislocation.

can not explain the loss of mass observed in the experiments [153, 154] and therefore a mechanism based on dislocation climb due to the removal of atoms from the lattice was proposed as a plausible explanation [157]. It was suggested that a two-atom vacancy defect can also be seen as a dislocation dipole (Fig. 5.2), which can both climb and glide. Ding et al. [157] modeled the combined climb and glide mechanism using a Monte Carlo simulation rather than molecular dynamics simulations because these are very slow phenomenon. Mori et al. [158] and Zhang et al. [159] performed molecular mechanics (MM) simulations on small CNTs under bending and tensile loading, respectively, to obtain the energetics of the glide of 5-7 pairs.

For large CNTs or multi-walled CNTs, atomistic simulations of dislocation glide and climb are computationally very expensive. CNTs have previously been modeled as thin shells in a continuum mechanics framework [160, 161, 162, 96, 70, 67, 126]. It was shown in [67] that continuum models of pristine CNTs can accurately model the large deformations and buckling instabilities. In this chapter, we have used a continuum model based on the extended finite element method (XFEM) [45, 46, 47] to study dislocations [54, 55, 56] in CNTs.

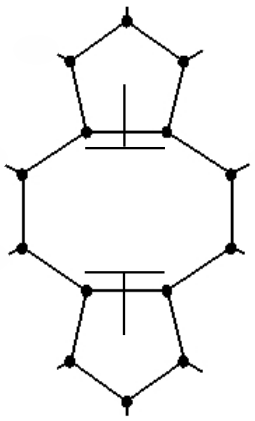

Figure 5.2. Two-atom vacancy defect can be seen as a pair of dislocations.

We used the extended finite element method in which, the finite element displacement field is enriched based on a known local feature of the solution of a given problem using a local partition of unity framework [48]. Problems such as crack propagation [45, 47], shear band [49], two phase flows [50], etc. have been modeled using XFEM without the requirement of remeshing [45, 46, 47].

Continuum models of dislocations are traditionally based on the superposition of infinite domain solutions [51, 52, 53]. As a result, these models are limited to small displacements and linear isotropic material models. Even though linear anisotropic models exist, their application is limited due to their computationally complexity. More importantly in the application to CNTs, the extension of these models to three dimensional shells is not obvious.

Recently new techniques for modeling dislocations based on the extended finite element method have been proposed [54, 163] where the superposition of infinite domain

solution is not required. The computation of the Peach-Kohler force and application to material interfaces were studied in [55] and the method was extended to non-linear formulation and applied to dislocations in three dimensions in [56]. Due to the ability of the XFEM to model arbitrary discontinuities [46], dislocation can be treated in the manner of a Volterra model [164], where a dislocation is modeled as a cut along the glide plane that is displaced and reattached. Using the extended finite element method, slip across the glide plane is modeled by a step function.

In this chapter, we have treated CNTs as thin shells and implemented the extended finite element method dislocation model using subdivision surface elements [165, 166] to solve the linear Kirchhoff-Love thin shell equations. The results are compared to molecular mechanics calculations done using a modified Tersoff-Brenner potential [4, 3, 84, 69, 83]. In particular, we have studied the energetics of tubes as the dislocations glide or climb in response to an applied tensile strain.

The rest of the chapter is organized as follows. Section 5.2 describes the XFEM implementation for the shell elements, the enrichment functions and the molecular mechanics method. Results and discussions are given in Section 5.3 and Section 5.4 presents the conclusions.

5.2. Method

5.2.1. XFEM for dislocations in shells

In this section we develop discrete equations for dislocations in thin shells using the Kirchhoff-Love theory. We start by defining the weak form, we then define the approximations for the displacement field and finally we derive the discrete equations.

5.2.1.1. Weak form.

Let the reference domain and the current domain of the body be denoted by Ω_0 and Ω, respectively, and let Γ_0 and Γ be their respective boundaries. Displacement $\overline{\mathbf{u}}$ is prescribed on Γ_{0u} and traction $\bar{\mathbf{t}}_0$ is prescribed on Γ_{0t}. Let Γ_{0d}^{λ} represent the interior discontinuities in the reference domain due to the dislocations, where $\lambda = 1 \dots n_{\mathrm{D}}$ and n_{D} is the total number of dislocations in the body. Let Γ_d^{λ} denote the same discontinuities in the current configuration. We define a parametric body $\overline{\Omega}$ with boundary $\overline{\Gamma}$, as shown in Fig. 5.3.

The undeformed and deformed configurations are mapped to the parametric body by differentiable and invertible maps φ_0 and φ, respectively, such that $\varphi_0(\overline{\Omega}) = \Omega_0$ and $\varphi(\overline{\Omega}) = \Omega$. The deformation map is then given as

$$\Phi = \varphi \circ \varphi_0^{-1}. \tag{5.1}$$

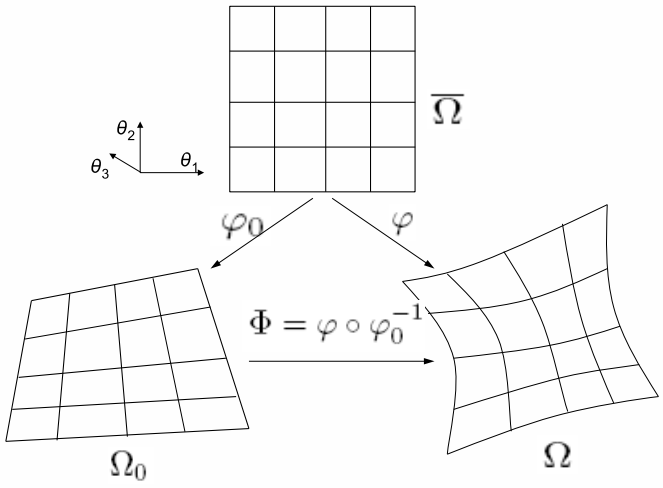

Figure 5.3. The reference domain, the current domain and the parametric domain.

The position vectors $\mathbf{x}$ and $\mathbf{X}$ of a material point in the current and the reference domain, respectively, can be written in terms of parametric coordinates $\{\theta_1, \theta_2, \theta_3\}$ such that

$$\mathbf{X}(\theta_1, \theta_2, \theta_3) = \mathbf{R}(\theta_1, \theta_2) + \theta_3 \mathbf{g}_3^0 \tag{5.2}$$

$$\mathbf{x}(\theta_1, \theta_2, \theta_3) = \mathbf{r}(\theta_1, \theta_2) + \theta_3 \mathbf{g}_3 \tag{5.3}$$

where the functions $\mathbf{R}(\theta_1, \theta_2)$ and $\mathbf{r}(\theta_1, \theta_2)$ are the parametric mappings of the shell in the reference and the deformed configuration, respectively. The corresponding convected

bases of the tangents of the deformed body, $\mathbf{g}_\alpha$, and undeformed body, $\mathbf{g}^0_\alpha$, are given by

$$\mathbf{g}_\alpha = \varphi_{,\alpha,}\ , \mathbf{g}^0_\alpha = \varphi^0_{,\alpha},\ \alpha = 1, 2. \tag{5.4}$$

The covariant component of the metric tensor of the surface of Ω and Ω_0 can be calculated by

$$g_{\alpha\beta} = \mathbf{g}_\alpha \cdot \mathbf{g}_\beta,\ g^0_{\alpha\beta} = \mathbf{g}^0_\alpha \cdot \mathbf{g}^0_\beta,\ \ \beta = 1, 2, \tag{5.5}$$

and the contravariant components of the deformed surface metric tensor, $G_{\alpha\beta}$, and the undeformed surface metric tensor, $G^0_{\alpha\beta}$, are obtained by taking the inverse of the deformed and undeformed covariant metric tensors, respectively.

Let the displacement of the mid surface be denoted by $\mathbf{u}$ such that

$$\mathbf{u}(\theta_1, \theta_2) = \mathbf{r}(\theta_1, \theta_2) - \mathbf{R}(\theta_1, \theta_2). \tag{5.6}$$

Using the above expressions, the membrane strain $\boldsymbol{\epsilon}^m$ and bending strain $\boldsymbol{\epsilon}^b$ are given by the following expressions [165]:

$$\epsilon^m_{\alpha\beta} = \frac{1}{2}(\mathbf{g}^0_\alpha \cdot \mathbf{u}_{,\beta} + \mathbf{g}^0_\beta \cdot \mathbf{u}_{,\alpha}), \tag{5.7}$$

$$\epsilon^b_{\alpha\beta} = -\mathbf{g}^0_3 \cdot \mathbf{u}_{,\alpha\beta} + \frac{1}{|g^0|}[(\mathbf{g}^0_{\alpha,\beta} \times \mathbf{g}^0_2) \cdot \mathbf{u}_{,1} + (\mathbf{g}^0_1 \times \mathbf{g}^0_{\alpha,\beta}) \cdot \mathbf{u}_{,2}] + \frac{(\mathbf{g}^0_{\alpha,\beta} \cdot \mathbf{g}^0_2)}{|g^0|}[(\mathbf{g}^0_2 \times \mathbf{g}^0_3) \cdot \mathbf{u}_{,1} + (\mathbf{g}^0_3 \times \mathbf{g}^0_1) \cdot \mathbf{u}_{,2}], \tag{5.8}$$

where

$$\mathbf{g}^0_3 = \frac{\mathbf{g}^0_1 \times \mathbf{g}^0_2}{|\mathbf{g}^0_1 \times \mathbf{g}^0_2|} \tag{5.9}$$

and

$$|g^0| = |\mathbf{g}^0_1 \times \mathbf{g}^0_2|. \tag{5.10}$$

$\mathbf{g}^0_3$ is constrained to coincide with the unit normal to the undeformed surface. In the similar manner, $\mathbf{g}_3$ and $|g|$ are calculated from the deformed surface.

The principal of virtual work for a thin shell under linear elastic assumptions [165, 166] is given as: find $\mathbf{u} \in \mathcal{U}$, such that

$$\int_\Omega \left[\eta^1 \delta\boldsymbol{\epsilon}^{m\mathrm{T}}(\mathbf{v})\mathbf{C}\boldsymbol{\epsilon}^m(\mathbf{u}) + \eta^2 \delta\boldsymbol{\epsilon}^{b\mathrm{T}}(\mathbf{v})\mathbf{C}\boldsymbol{\epsilon}^b(\mathbf{u})\right] \mathrm{d}\Omega - \int_\Omega \mathbf{q} \cdot \mathbf{v} \mathrm{d}\Omega - \int_{\Gamma_\mathrm{t}} \bar{\mathbf{t}} \cdot \mathbf{v} \mathrm{d}\Gamma, \forall \mathbf{v} \in \mathcal{U}_0, \tag{5.11}$$

where $\eta^1 = Eh/(1-\nu^2)$, $\eta^2 = Eh^3/12(1-\nu^2)$, h is the thickness of the shell, E is Young's modulus, ν is Poisson's ratio, $\mathbf{q}$ is the body force and $\bar{\mathbf{t}}$ is the traction applied on boundary

Γ_t and $\mathbf{C}$ is given by

$$\mathbf{C} = \begin{bmatrix} (G^0_{11})^2 & \nu G^0_{11}G^0_{22} + (1-\nu)(G^0_{12})^2 & G^0_{11}G^0_{12} \\ & (G^0_{22})^2 & G^0_{22}G^0_{12} \\ \text{sym.} & & \frac{1}{2}[(1-\nu)G^0_{11}G^0_{22} + (1+\nu)(G^0_{12})^2] \end{bmatrix}. \tag{5.12}$$

Note that Eq. (5.8) involves the second derivative of the displacement and therefore C^1 continuity is required for the displacement field. The spaces $\mathcal{U}_0$ and $\mathcal{U}$ in Eq. (5.11) are defined as

$$\mathcal{U}_0 = \{\mathbf{u} \in H^2(\Omega \setminus \Gamma_d), \mathbf{u} = 0 \text{ on } \Gamma_u\}, \tag{5.13}$$

$$\mathcal{U} = \{\mathbf{u} \in H^2(\Omega \setminus \Gamma_d), \mathbf{u} = \overline{\mathbf{u}} \text{ on } \Gamma_u\}. \tag{5.14}$$

5.2.1.2. Displacement approximations.

In XFEM of a dislocation, the displacement approximation is decomposed into a standard continuous part $\mathbf{u}^{\mathrm{C}}$ and an enriched or discontinuous part $\mathbf{u}^{\mathrm{D}}$, such that

$$\mathbf{u}(\theta_1, \theta_2) = \mathbf{u}^{\mathrm{C}}(\theta_1, \theta_2) + \mathbf{u}^{\mathrm{D}}(\theta_1, \theta_2), \tag{5.15}$$

where $\mathbf{u}^{\mathrm{C}}$ is given by the standard finite element approximation

$$\mathbf{u}^{\mathrm{C}}(\theta_1, \theta_2) = \sum_I N_I(\theta_1, \theta_2)\mathbf{u}_I, \tag{5.16}$$

where N_I are the finite element interpolants and $\mathbf{u}_I$ are the nodal degrees of freedom. We define the map φ_0 between the parametric domain $\overline{\Omega}$ and the reference domain Ω_0 such that for an initially flat shell

$$\begin{aligned} \boldsymbol{\theta}_1 &= \mathbf{X}_1, \\ \boldsymbol{\theta}_2 &= \mathbf{X}_2, \\ \boldsymbol{\theta}_3 &= \mathbf{X}_3, \end{aligned} \tag{5.17}$$

where $\mathbf{X}_1$, $\mathbf{X}_2$, $\mathbf{X}_3$ are the basis vectors of the reference coordinate system.

The geometry of a dislocation pair is described in the parametric coordinate system by two level set functions $f(\theta_1, \theta_2)$ and $\mathrm{g}(\theta_1, \theta_2)$, such that the glide plane is given by $f(\theta_1, \theta_2) = 0$ and $\mathrm{g}(\theta_1, \theta_2) < 0$ and the dislocation cores are given by the points of intersection of the contours $f(\theta_1, \theta_2) = 0$ and $\mathrm{g}(\theta_1, \theta_2) = 0$, as shown in Fig. 5.4. In addition, we associate a scalar with each dislocation core: +1 or -1 when the sense of the dislocation line passing through the core is in the direction of $+\boldsymbol{\theta}_2$ and $-\boldsymbol{\theta}_2$, respectively.

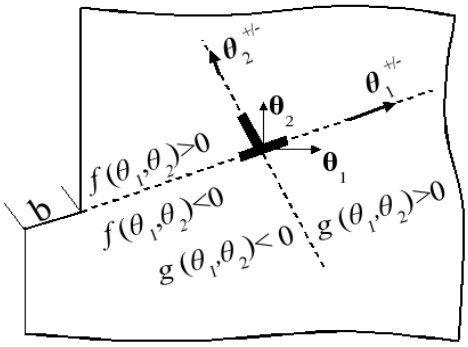

Figure 5.4. An edge dislocation in two dimensional sheet.

For every dislocation pair, there is always one dislocation with a positive sense and one with a negative sense.

We also define a local coordinate system at each of these cores. Let $\boldsymbol{\theta}_1^+$, $\boldsymbol{\theta}_2^+$ and $\boldsymbol{\theta}_1^-$, $\boldsymbol{\theta}_2^-$ be the basis vectors of the local coordinate system at the core with positive and negative sense, respectively. These basis vectors are constructed from the level sets $f(\theta_1, \theta_2)$ and $\mathrm{g}(\theta_1, \theta_2)$:

$$\boldsymbol{\theta}_1^\diamond = \boldsymbol{\nabla} \mathrm{g}|_{\boldsymbol{\theta}_c^\diamond},$$

$$\boldsymbol{\theta}_2^\diamond = \diamond \nabla f|_{\boldsymbol{\theta}_c^\diamond}, \ \diamond = +, -, \tag{5.18}$$

where $\boldsymbol{\theta}_c^{+,-}$ is the location of the positive or negative core in the parametric coordinate system.

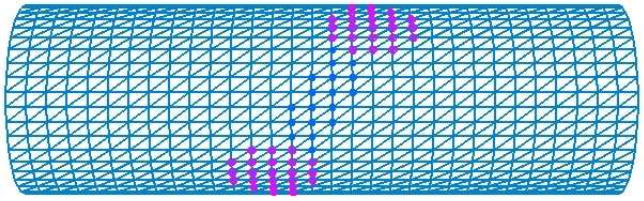

Figure 5.5. An XFEM model of an edge dislocation pair in a CNT. The bigger and darker nodes belong to $\mathrm{S}^{\infty,\diamond}$ and the smaller and lighter nodes belong to S^{H}. Note that for the clarity of vision only upper half of the tube is shown.

The enriched part of the displacement field for an edge dislocation dipole is given by

(5.19)

$$\mathbf{u}^{\mathrm{D}}(\theta_1,\theta_2) = \sum_{J\in \mathrm{S}^{H}} N_J(\theta_1,\theta_2)[\boldsymbol{\Psi}^{H}(\theta_1,\theta_2) - \boldsymbol{\Psi}_J^{H}] + \sum_{K\in \mathrm{S}^{\infty,+}} N_K(\theta_1,\theta_2)[\boldsymbol{\Psi}^{\infty,+}(\theta_1,\theta_2) - \boldsymbol{\Psi}_K^{\infty,+}] + \sum_{L\in \mathrm{S}^{\infty,-}} N_L(\theta_1,\theta_2)[\boldsymbol{\Psi}^{\infty,-}(\theta_1,\theta_2) - \boldsymbol{\Psi}_L^{\infty,-}],$$

where $\boldsymbol{\Psi}_J^{H} = \boldsymbol{\Psi}_J^{H}(\theta_1^J,\theta_2^J)$, $\boldsymbol{\Psi}_K^{\infty,+} = \boldsymbol{\Psi}_K^{\infty,+}(\theta_1^K,\theta_2^K)$ and $\boldsymbol{\Psi}_L^{\infty,-} = \boldsymbol{\Psi}_L^{\infty,-}(\theta_1^L,\theta_2^L)$. θ_1^J and θ_2^J are the parametric coordinates of node J. A node K is in $\mathrm{S}^{\infty,+}$ if $||\boldsymbol{\theta}_K - \boldsymbol{\theta}_c^{+}|| < \rho^{+}$, is in $\mathrm{S}^{\infty,-}$ if $||\boldsymbol{\theta}_K - \boldsymbol{\theta}_c^{-}|| < \rho^{-}$ and is in S^{H} if K is not in $\mathrm{S}^{\infty,+}$ nor $\mathrm{S}^{\infty,-}$ and the support of K is cut by $f(\theta_1,\theta_2) = 0$. Fig. 5.5 shows such an XFEM model of CNT.

The image of $\boldsymbol{\Psi}^{H}(\theta_1,\theta_2)$ in the parametric domain is

$$\mathbf{\Psi}_{\theta}^{H}(\theta_1, \theta_2) = \mathbf{b}_{\theta} H(f(\theta_1, \theta_2)) H(g(\theta_1, \theta_2)), \tag{5.20}$$

where $H(\cdot)$ is the Heaviside step function and $\mathbf{b}_{\theta}$ is the image of the Burgers vector $\mathbf{b}$ in the parametric domain.

We note here that both the magnitude and direction of $\mathbf{b}_{\theta}$ are constant along the parametric image of the glide plane between two edge or prismatic dislocations. However, the magnitude and direction of the Burgers vector, $\mathbf{b}$, in the reference domain will depend upon the curvature of the shell.

The image of $\mathbf{\Psi}^{\infty,\diamond}(\theta_1, \theta_2)$ in the parametric domain is

$$\mathbf{\Psi}_{\theta}^{\infty,\diamond}(\theta_1, \theta_2) = \mathbf{T}^{\diamond} \cdot \mathbf{u}^{\infty,\diamond}(\theta_1^{\diamond}, \theta_2^{\diamond}), \;\; \diamond = +, -, \tag{5.21}$$

where

$$\mathbf{T}^{\diamond} = \begin{bmatrix} \boldsymbol{\theta}_1 \cdot \boldsymbol{\theta}_1^{\diamond} & \boldsymbol{\theta}_1 \cdot \boldsymbol{\theta}_2^{\diamond} \\ \boldsymbol{\theta}_2 \cdot \boldsymbol{\theta}_1^{\diamond} & \boldsymbol{\theta}_2 \cdot \boldsymbol{\theta}_2^{\diamond} \end{bmatrix}. \tag{5.22}$$

$\mathbf{u}^{\infty,\diamond}$ is the solution for an edge dislocation in the infinite two dimensional domain and is given by

$$\mathbf{u}^{\infty,\diamond}(\theta_1^\diamond,\theta_2^\diamond) = b_\theta \frac{1}{2\pi} \begin{bmatrix} \left(\tan^{-1}\left(\frac{\theta_2^\diamond}{\theta_1^\diamond}\right) + \frac{\theta_1^\diamond \theta_2^\diamond}{2(1-\nu)(\theta_1^{\diamond 2}+\theta_2^{\diamond 2})}\right) \\ -\left(\frac{1-2\nu}{4(1-\nu)}\ln(\theta_1^{\diamond 2}+\theta_2^{\diamond 2}) + \frac{\theta_1^{\diamond 2}-\theta_2^{\diamond 2}}{4(1-\nu)(\theta_1^{\diamond 2}+\theta_2^{\diamond 2})}\right) \end{bmatrix}. \tag{5.23}$$

where b_θ is the magnitude of the Burgers vector in the parametric domain.

A prismatic dislocation dipole can be created by either removing a row of atoms from the lattice or inserting an extra row of atoms, as shown in Fig. 5.6. We have used a step enrichment function to model this type of dislocation as proposed in [54]. The discontinuous part of the displacement approximation for a prismatic dislocation is

$$\mathbf{u}^{\mathrm{D}}(\theta_1,\theta_2) = \sum_{J\in \mathrm{S}^P} N_J(\theta_1,\theta_2)[\mathbf{\Psi}^P(\theta_1,\theta_2) - \mathbf{\Psi}_J^P], \tag{5.24}$$

where $\mathbf{\Psi}_J^P = \mathbf{\Psi}_J^P(\theta_1^J,\theta_2^J)$. The nodal set S^{P} is the set of all the nodes of the elements cut by $f(\theta_1,\theta_2)=0$ and $\mathrm{g}(\theta_1,\theta_2)<0$. Fig. 5.7 shows such an XFEM model of a CNT containing a prismatic dislocation pair. The image of $\mathbf{\Psi}^P(\theta_1,\theta_2)$ in the parametric domain is

$$\mathbf{\Psi}_\theta^P(\theta_1,\theta_2) = \mathbf{b}_\theta H(f(\theta_1,\theta_2))H(g(\theta_1,\theta_2)). \tag{5.25}$$

where $\mathbf{b}_\theta$ is perpendicular to $f(\theta_1,\theta_2)=0$.

For a cylinder of radius R the enrichment functions $\mathbf{\Psi}_\theta^H$, $\mathbf{\Psi}_\theta^{\infty,\diamond}$ and $\mathbf{\Psi}_\theta^P$ are mapped into the reference coordinate system using $\mathbf{X} = \varphi_0(\boldsymbol{\theta})$, such that

$$\begin{aligned} \Psi_1(\theta_1,\theta_2) &= \Psi_{\theta 1}(\theta_1,\theta_2), \\ \Psi_2(\theta_1,\theta_2) &= R(\cos(\theta_2/R + \Psi_{\theta 2}/R) - \cos(\theta_2/R)), \\ \Psi_3(\theta_1,\theta_2) &= R(\sin(\theta_2/R + \Psi_{\theta 2}/R) - \sin(\theta_2/R)). \end{aligned} \tag{5.26}$$

For small $\Psi_{\theta 2}$, Eq. (5.26) can be reduced to

$$\begin{aligned} \Psi_1(\theta_1,\theta_2) &= \Psi_{\theta 1}(\theta_1,\theta_2), \\ \Psi_2(\theta_1,\theta_2) &\approx -\Psi_{\theta 2}\sin(\theta_2/R), \\ \Psi_3(\theta_1,\theta_2) &\approx \Psi_{\theta 2}\cos(\theta_2/R). \end{aligned} \tag{5.27}$$

Note that the above equations give us a linear mapping between the enrichment functions in the parametric domain and the reference domain. This allows us to write Eqs. (5.19) and (5.24) as

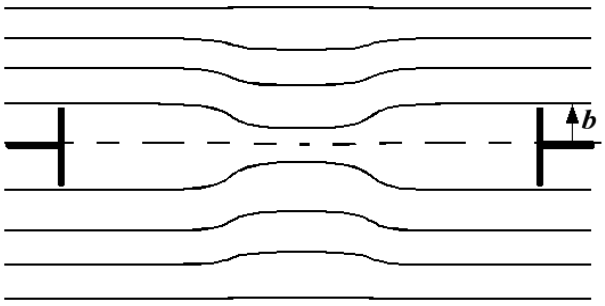

Figure 5.6. Prismatic dislocation in two dimensional sheet.

$$\mathbf{u}^{\mathrm{D}}(\theta_1,\theta_2) = b_\theta \left(\sum_{J\in \mathrm{S}^H} N_J(\theta_1,\theta_2)[\boldsymbol{\Upsilon}^H(\theta_1,\theta_2) - \boldsymbol{\Upsilon}^H_J] + \sum_{K\in \mathrm{S}^{\infty,+}} N_K(\theta_1,\theta_2)[\boldsymbol{\Upsilon}^{\infty,+}(\theta_1,\theta_2) - \boldsymbol{\Upsilon}^{\infty,+}_K] + \sum_{L\in \mathrm{S}^{\infty,-}} N_L(\theta_1,\theta_2)[\boldsymbol{\Upsilon}^{\infty,-}(\theta_1,\theta_2) - \boldsymbol{\Upsilon}^{\infty,-}_L] \right), \tag{5.28}$$

and

$$\mathbf{u}^{\mathrm{D}}(\theta_1,\theta_2) = b_\theta \sum_{J\in \mathrm{S}^P} N_J(\theta_1,\theta_2)[\boldsymbol{\Upsilon}^P(\theta_1,\theta_2) - \boldsymbol{\Upsilon}^P_J], \tag{5.29}$$

respectively, where, $\boldsymbol{\Upsilon}^H = \boldsymbol{\Psi}^H/b_\theta$, $\boldsymbol{\Upsilon}^{\infty,\diamond} = \boldsymbol{\Psi}^{\infty,\diamond}/b_\theta$ and $\boldsymbol{\Upsilon}^P = \boldsymbol{\Psi}^P/b_\theta$. This expression is similar to the ones for two dimensional simulations used in [54, 56] for the enriched displacement and it gives the discrete equations of same form.

To simplify the presentation of discrete equations, we condense the approximation (5.28) into the following equivalent form:

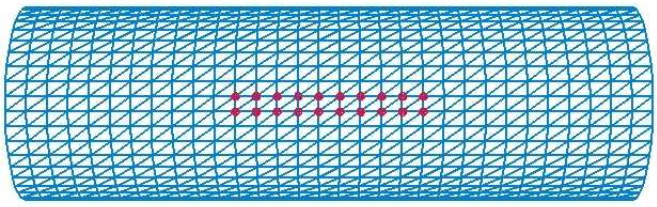

Figure 5.7. An XFEM model of a prismatic dislocation pair in a CNT. The bigger and darker nodes belong to S^{P}. Note that for the clarity of vision only upper half of the tube is shown.

$$\mathbf{u}^{\mathrm{D}}(\theta_1,\theta_2)=\sum_{J\in\mathrm{S}}N_J(\theta_1,\theta_2)[\boldsymbol{\Upsilon}(\theta_1,\theta_2)-\boldsymbol{\Upsilon}_J], \tag{5.30}$$

where S and Υ are chosen so that Eqs. (5.30) and (5.28) are equivalent. The enriched displacement for n^{D} dislocations can be written as

$$\mathbf{u}^{\mathrm{D}}(\theta_1,\theta_2)=\sum_{\lambda=1}^{n^{\mathrm{D}}}b_\theta^\lambda\sum_{J\in\mathrm{S}^\lambda}N_J(\theta_1,\theta_2)[\boldsymbol{\Upsilon}^\lambda(\theta_1,\theta_2)-\boldsymbol{\Upsilon}^\lambda{}_J], \tag{5.31}$$

where $\boldsymbol{\Upsilon}^\lambda(\theta_1,\theta_2)$ is the enrichment function of dislocation λ and S^λ is the set of enriched nodes for dislocation λ.

5.2.1.3. Discrete equations.

We substitute Eqs. (5.16) and (5.31) into Eq. (5.15) and Eq. (5.15) into Eq. (5.11) to obtain the following discrete equations

$$\mathbf{K}\mathbf{d} = \mathbf{f}^{\text{ext}} + \mathbf{f}^{\text{d}}, \tag{5.32}$$

where

$$\mathbf{f}_I^{\text{ext}} = \int_\Omega \mathbf{N}_I^{\text{T}} \mathbf{q} \text{d}\Omega + \int_{\Gamma_{\text{t}}} \mathbf{N}_{\text{I}}^{\text{T}} \bar{\mathbf{t}} \text{d}\Gamma, \tag{5.33}$$

$$\mathbf{f}_I^{\text{d}} = -\mathbf{K}_{I\lambda}^b \mathfrak{b}_\lambda, \tag{5.34}$$

where $\mathbf{d}$ is a vector of nodal unknowns, $\mathfrak{b}$ is a vector of Burgers vector magnitudes, $\mathfrak{b}^{\text{T}} = [b_\theta^1, b_\theta^2 .... b_\theta^{n^{\text{D}}}]$,

$$\mathbf{K}_{IJ} = \int_\Omega \left[\eta^1 (\mathbf{M}^I)^{\text{T}} \mathbf{C} \mathbf{M}^J + \eta^2 (\mathbf{B}^I)^{\text{T}} \mathbf{C} \mathbf{B}^J \right] \text{d}\Omega \tag{5.35}$$

and

$$\mathbf{K}_{I\lambda}^b = \int_\Omega \left[\eta^1 (\mathbf{M}^I)^{\text{T}} \mathbf{C} \mathbf{P}^\lambda + \eta^2 (\mathbf{B}^I)^{\text{T}} \mathbf{C} \mathbf{D}^\lambda \right] \text{d}\Omega. \tag{5.36}$$

The matrices $\mathbf{M}$, $\mathbf{P}$, $\mathbf{B}$ and $\mathbf{D}$ are

$$\mathbf{M}^I = \begin{bmatrix} N_{I,1}\mathbf{g}_1 \cdot \mathbf{e}_1 & N_{I,1}\mathbf{g}_1 \cdot \mathbf{e}_2 & N_{I,1}\mathbf{g}_1 \cdot \mathbf{e}_3 \\ N_{I,2}\mathbf{g}_1 \cdot \mathbf{e}_1 & N_{I,2}\mathbf{g}_1 \cdot \mathbf{e}_2 & N_{I,2}\mathbf{g}_1 \cdot \mathbf{e}_3 \\ (N_{I,2}\mathbf{g}_1 + N_{I,1}\mathbf{g}_2) \cdot \mathbf{e}_1 & (N_{I,2}\mathbf{g}_1 + N_{I,1}\mathbf{g}_2) \cdot \mathbf{e}_2 & (N_{I,2}\mathbf{g}_1 + N_{I,1}\mathbf{g}_2) \cdot \mathbf{e}_3 \end{bmatrix}, \tag{5.37}$$

$$\mathbf{P}^\lambda = \sum_{I \in \mathrm{S}^\lambda} \begin{bmatrix} (N_I \Upsilon^\lambda_1)_{,1}\mathbf{g}_1 \cdot \mathbf{e}_1 & (N_I \Upsilon^\lambda_2)_{,1}\mathbf{g}_1 \cdot \mathbf{e}_2 & (N_I \Upsilon^\lambda_3)_{,1}\mathbf{g}_1 \cdot \mathbf{e}_3 \\ (N_I \Upsilon^\lambda_1)_{,2}\mathbf{g}_1 \cdot \mathbf{e}_1 & (N_I \Upsilon^\lambda_2)_{,2}\mathbf{g}_1 \cdot \mathbf{e}_2 & (N_I \Upsilon^\lambda_3)_{,2}\mathbf{g}_1 \cdot \mathbf{e}_3 \\ \big\{(N_I \Upsilon^\lambda_1)_{,2}\mathbf{g}_1 + & \big\{(N_I \Upsilon^\lambda_2)_{,2}\mathbf{g}_1 + & \big\{(N_I \Upsilon^\lambda_3)_{,2}\mathbf{g}_1 + \\ (N_I \Upsilon^\lambda_1)_{,1}\mathbf{g}_2\big\} \cdot \mathbf{e}_1 & (N_I \Upsilon^\lambda_2)_{,1}\mathbf{g}_2\big\} \cdot \mathbf{e}_2 & (N_I \Upsilon^\lambda_3)_{,1}\mathbf{g}_2\big\} \cdot \mathbf{e}_3 \end{bmatrix}, \tag{5.38}$$

$$\begin{Bmatrix} B^I_{1j} \\ B^I_{2j} \\ B^I_{3j} \end{Bmatrix} = \begin{bmatrix} \Big(-N_{I,11}\mathbf{g}_3 + \frac{1}{|g|}[N_{I,1}\mathbf{g}_{1,1} \times \mathbf{g}_2 + N_{I,2}\mathbf{g}_1 \times \mathbf{g}_{1,1} + \\ \quad \mathbf{g}_3 \cdot \mathbf{g}_{1,1}(N_{I,1}\mathbf{g}_2 \times \mathbf{g}_3 + N_{I,2}\mathbf{g}_3 \times \mathbf{g}_1)]\Big) \cdot \mathbf{e}_j \\ \Big(-N_{I,22}\mathbf{g}_3 + \frac{1}{|g|}[N_{I,1}\mathbf{g}_{2,2} \times \mathbf{g}_2 + N_{I,2}\mathbf{g}_1 \times \mathbf{g}_{2,2} + \\ \quad \mathbf{g}_3 \cdot \mathbf{g}_{2,2}(N_{I,1}\mathbf{g}_2 \times \mathbf{g}_3 + N_{I,2}\mathbf{g}_3 \times \mathbf{g}_1)]\Big) \cdot \mathbf{e}_j \\ \Big(-N_{I,12}\mathbf{g}_3 + \frac{1}{|g|}[N_{I,1}\mathbf{g}_{1,2} \times \mathbf{g}_2 + N_{I,2}\mathbf{g}_1 \times \mathbf{g}_{1,2} + \\ \quad \mathbf{g}_3 \cdot \mathbf{g}_{1,2}(N_{I,1}\mathbf{g}_2 \times \mathbf{g}_3 + N_{I,2}\mathbf{g}_3 \times \mathbf{g}_1)]\Big) \cdot \mathbf{e}_j \end{bmatrix} \tag{5.39}$$

and

$$
(5.40)\quad \left\{ \begin{array}{c} D^I_{1j} \\ D^I_{2j} \\ D^I_{3j} \end{array} \right\} = \sum_{I \in \mathrm{S}^\lambda} \left[\begin{array}{c} \{-(N_I \Upsilon^\lambda_j)_{,11}\mathbf{g}_3 + \frac{1}{|g|}[(N_I \Upsilon^\lambda_j)_{,1}\mathbf{g}_{1,1} \times \mathbf{g}_2 \\ +(N_I \Upsilon^\lambda_j)_{,2}\mathbf{g}_1 \times \mathbf{g}_{1,1} + \mathbf{g}_3 \cdot \mathbf{g}_{1,1}((N_I \Upsilon^\lambda_j)_{,1}\mathbf{g}_2 \times \mathbf{g}_3 \\ +(N_I \Upsilon^\lambda_j)_{,2}\mathbf{g}_3 \times \mathbf{g}_1)]\} \cdot \mathbf{e}_j \\ \{-(N_I \Upsilon^\lambda_j)_{,22}\mathbf{g}_3 + \frac{1}{|g|}[(N_I \Upsilon^\lambda_j)_{,1}\mathbf{g}_{2,2} \times \mathbf{g}_2 \\ +(N_I \Upsilon^\lambda_j)_{,2}\mathbf{g}_1 \times \mathbf{g}_{2,2} + \mathbf{g}_3 \cdot \mathbf{g}_{2,2}((N_I \Upsilon^\lambda_j)_{,1}\mathbf{g}_2 \times \mathbf{g}_3 \\ +(N_I \Upsilon^\lambda_j)_{,2}\mathbf{g}_3 \times \mathbf{g}_1)]\} \cdot \mathbf{e}_j \\ \{-(N_I \Upsilon^\lambda_j)_{,12}\mathbf{g}_3 + \frac{1}{|g|}[(N_I \Upsilon^\lambda_j)_{,1}\mathbf{g}_{1,2} \times \mathbf{g}_2 \\ +(N_I \Upsilon^\lambda_j)_{,2}\mathbf{g}_1 \times \mathbf{g}_{1,2} + \mathbf{g}_3 \cdot \mathbf{g}_{1,2}((N_I \Upsilon^\lambda_j)_{,1}\mathbf{g}_2 \times \mathbf{g}_3 \\ +(N_I \Upsilon^\lambda_j)_{,2}\mathbf{g}_3 \times \mathbf{g}_1)]\} \cdot \mathbf{e}_j \end{array} \right],
$$

for $j = 1$ to 3. For more details on obtaining the discrete equations for shell elements see [165, 166].

Note that $\mathbf{K}$ is the standard finite element stiffness matrix, which remains unaltered by the enrichment and the effects of the dislocations appear only through nodal forces. This is a major advantage, since solving the above system for moving dislocations is computationally cheap as triangulation of the stiffness matrix is only required once when a direct solver is used. For further details on this method see [54, 55, 56]. Note that we have adopted a linear elastic formulation, though nonlinear materials can be formulated in a similar manner [56].

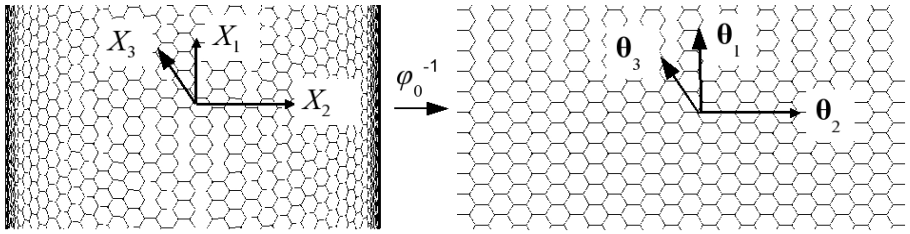

Figure 5.8. A graphene sheet rolled into a CNT along axis X_2.

5.2.2. Molecular mechanics

To evaluate the continuum dislocation method, we compared it to atomistic simulations. Atomic simulations are performed using the modified Tersoff-Brenner (MTB-G2) potential [84, 83]. MTB-G2 is a modified standard reactive empirical bond order (REBO) potential [84], where the cut-off function is removed and interatomic interactions are included only for atom pairs within a distance of 2 Å in initial unstrained configurations [69, 83].

The total energy of the system was minimized to obtain the optimum geometry. All the calculations were done at 0 K. The locations of carbon atoms at the ends of the tube were prescribed to apply the displacement boundary conditions and their edges were terminated with hydrogen atoms. At each strain increment, the CNT configuration was optimized with the carbon atoms at the boundary constrained using a large scale BFGS quasi-Newton algorithm [60]. Once the geometry was optimized at a given applied strain, the stresses in the tube can be calculated by taking derivatives of the energy using finite differences with respect to the strain. An effective thickness of 3.4 Å was used in the

stress calculations; this corresponds to the interlayer spacing in graphite, and is widely used to present the tractions on CNTs as stresses [96].

5.3. Results

5.3.1. Glide of dislocation by bond rotation

We begin by studying the energetics of a pair of edge dislocations in a CNT using both MM and XFEM. The edge dislocation pair is generated by creating a Stone-Wales defect, as shown in Fig. 5.1. Ding et al. [157] suggested that in the glide mechanism in CNTs, where the side bond of one of the heptagons of the Stone-Wales defect is rotated by 90° and the reconstruction of bonds generates two separated 5-7 pairs thus changing the chirality of the tube, as shown in Fig. 5.9. This process when repeated several times can reduce the diameter and increase the length of the tube significantly. Here we perform the MM and XFEM calculations for this process in a [15,15] CNT under different applied strains.

In the MM calculations a 249.6 Å long [15,15] CNT containing 6120 atoms was considered. A Stone-Wales defect was created in the center of the tube and the energy was minimized with end carbon atoms fixed to obtain the optimum geometry. The 5-7 pairs were then allowed to glide away from each other by bond rotation and reconstruction, as shown in Fig. 5.9 and the optimized energy was calculated at every glide step. The entire glide process was repeated with the CNT stretched by applying appropriate displacement to the carbon atoms at the end of the tube and the energy at various glide steps was

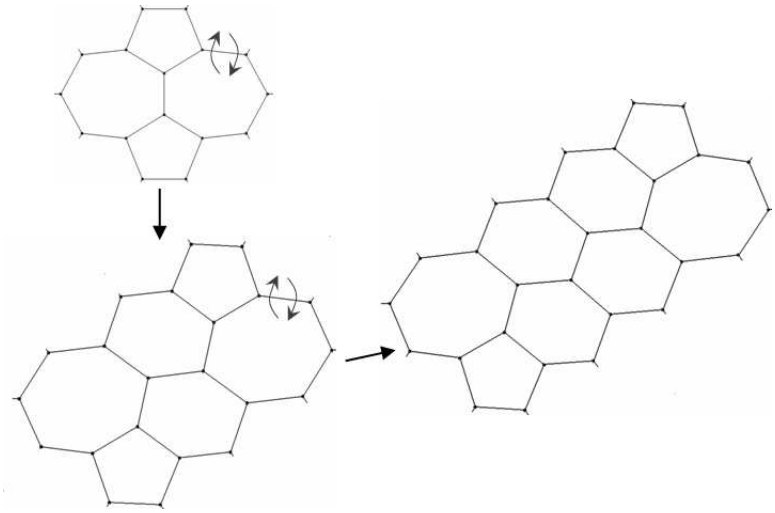

Figure 5.9. 5-7 pairs gliding away form each other due to bond reconstructions.

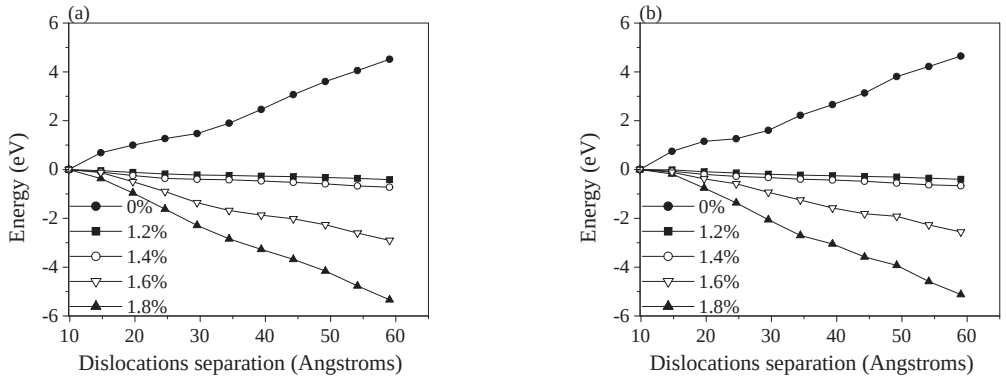

Figure 5.10. Energy change at various strains with glide calculated by (a) MM and (b) XFEM for a [15,15] CNT. One glide step corresponds to the Stone-Wales rotation of one bond and $\sim 12^o$ separation between the two dislocation cores.

calculated. Fig. 5.10(a) shows the dependence of the energy on the separation distance between two 5-7 pairs at different applied strains. It is observed that when the applied strain is less than 1.2%, the energy of the tube increases as the 5-7 defects move away from

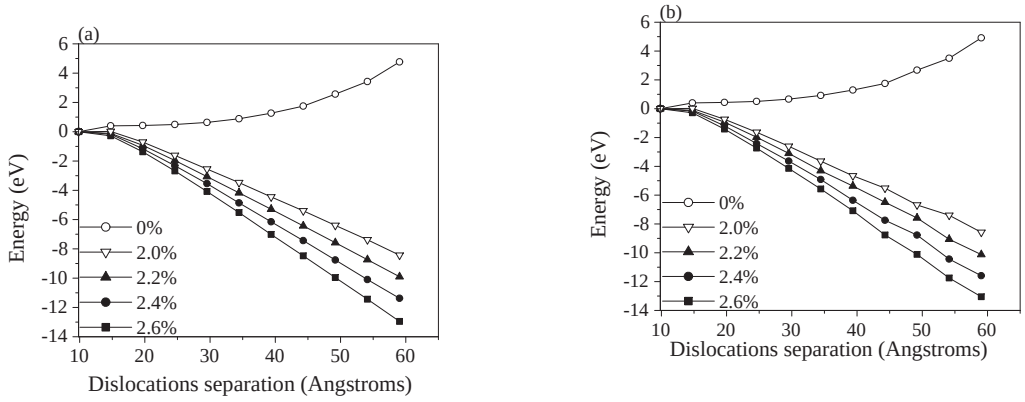

Figure 5.11. Energy change at various strains with glide calculated by (a) MM and (b) XFEM for a [50,50] CNT. One glide step corresponds to the Stone-Wales rotation of one bond and $\sim 7.2^o$ separation between the two dislocation cores.

each other, suggesting that the gliding process is not energetically favorable. However, as the applied strain becomes more than 1.2%, a decrease in the energy is observed, suggesting that the process of glide becomes energetically favorable when the applied strain is increased. Similar energetics was also observed by Zhang et al. [159] for CNTs in tension and Mori et al. [158] for CNTs under bending deformations. Note that we have shown energies relative to the energy of the tube when the dislocations are 4 glide steps apart at the given strain, so all the energies in the plot to start at 0 eV.

We have reproduced the above mentioned MM calculations using the XFEM technique. A cylindrical mesh of the same radius and length as that of the [15,15] CNT used in the above example is constructed. We have used subdivision surface elements [165, 166]. The finite element mesh consisted of 1440 elements and 765 nodes and the enrichment function in Eq. (5.19) was used versus 6120 atoms for the MM calculations. The material

properties $E = 730$ GPa and $\nu = 0.4$ were calculated using the MTB-G2 potential. A dislocation dipole was introduced by using the discontinuous enrichment function away from the two cores for the glide planes. The singular core enrichment was used for the nodes within a distance equal to twice the magnitude of the Burgers vector (2.46 Å) from the cores, thus $\rho^+ = \rho^- = 2b$. The dislocation cores were moved away from each other along their glide planes to replicate the movement of 5-7 defect pairs in the MM calculations. Displacement boundary conditions were applied by fixing all degrees of freedom of the boundary nodes.

In XFEM calculations using the above mentioned enrichment functions, the total energy of the system diverges because $\mathbf{u}^\infty$ is singular [55]. Therefore, to calculate a finite strain energy a small region around the dislocation cores was omitted in the strain energy calculations as is common in continuum dislocation models. The omitted region was calculated by comparing the energy of the XFEM model with the MM calculation at 0% applied strain with a separation of four glide steps between the two dislocations. Note that a single glide step separates two dislocations pair by a single hexagon, which is a $\sim 12^o$ angular separation for a [15,15] CNT. For this set of strain energy calculations we have excluded the quadrature points within a distance of 2.6 Å from the dislocation cores.

Fig. 5.10(b) shows the energy curves calculated by XFEM at different applied strains as the dislocations move apart. Similar to the MM calculations, we observe that after an applied strain of 1.2%, the dislocation motion becomes energetically favorable.

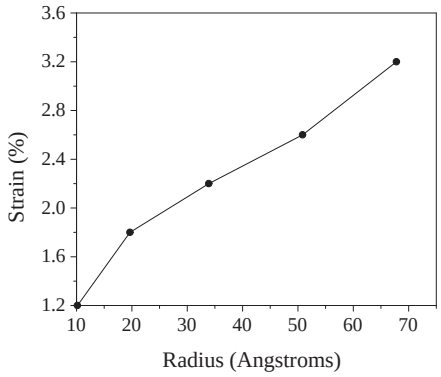

Figure 5.12. Tensile strain at which glide becomes energetically favorable with increasing CNT radius.

We repeated the same set of calculations on a [50,50] CNT using both the MM and XFEM methods. The XFEM model was 249.6 Å long and consisted of 4800 elements and 2550 nodes in comparison to 20400 atoms in the MM model. The energy variation with the glide steps is shown in Fig. 5.11. Similar to the [15,15] CNT, for small applied strain the energy of the [50,50] tube increases and for high strains the energy decreases as the two dislocations glides away from each other. However, glide becomes energetically favorable at applied strain 2.2%, which is higher than the strain at which the same happens in [15,15] CNT. In Fig. 5.12, we have plotted these transition strains calculated using XFEM for CNTs with radius as large as 67.8 Å ([100,100] CNT). It is observed that as the tube radius increases the transition strain increases. This is reasonable as CNT with smaller radius bears higher bending strain, which adds to the total strain energy of the tube and therefore gliding becomes energetically favorable at smaller strains.

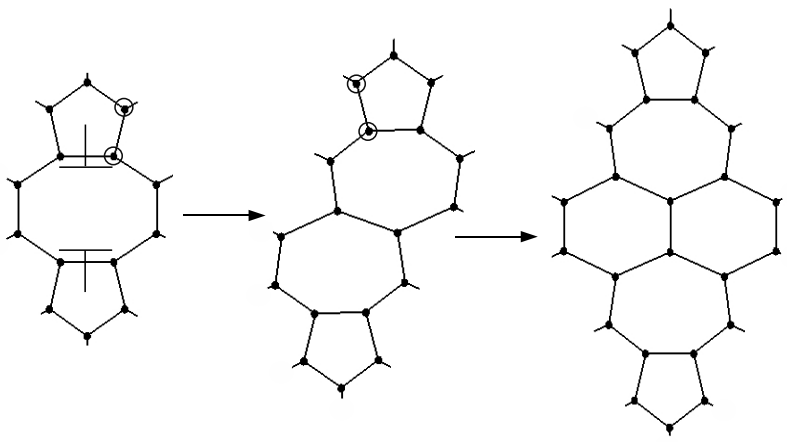

Figure 5.13. Climb motion of dislocation due to sequential removal of two-atom pairs (circled atoms).

5.3.2. Climb of dislocation by atom removal

We next model climb of dislocation pairs away from each other due to the removal of atom pairs from the lattice. It was proposed [157] that the loss in mass of CNTs during the experiments [153] was due to the removal of atom pairs, which also leads to the climb motion of a prismatic dislocation. As shown in Fig. 5.13, a two-atom vacancy can be seen as a dislocation pair. Removal of pairs of atoms followed by the reconstruction of bonds makes the dislocation pair climb away from each other, as shown in Fig. 5.13.

We modeled the climb motion first using MM. A two-atom vacancy defect was first created in a 143.5 Å long [10,0] CNT containing 1360 atoms. Pair of atoms were then removed sequentially and the energy for the optimized structure was calculated so that the climb direction is along the axis of tube. The same process was repeated after applying tensile strain to the tube. The energy of the tube, shown in Fig. 5.14(a), increases as the

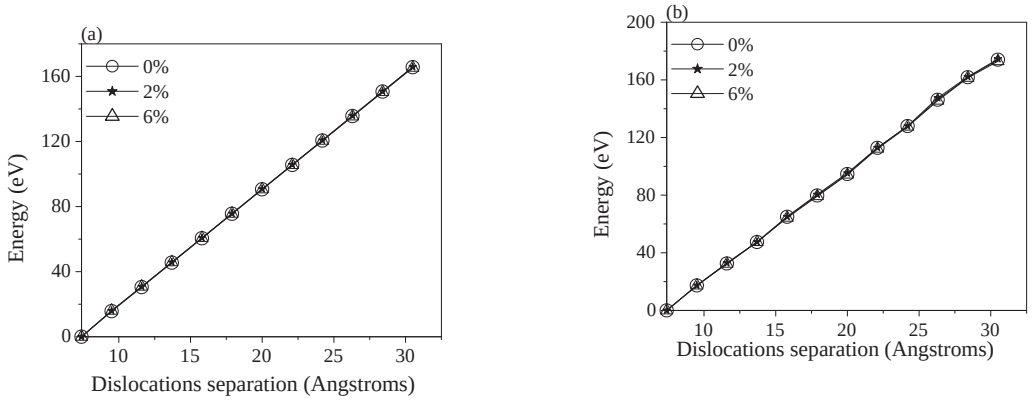

Figure 5.14. Energy change at various strains with climb calculated by (a) MM and (b) XFEM for a [10,0] CNT. One climb step corresponds to the removal of two carbon atoms and $\sim$ 2.1 Å separation between the two dislocation cores.

dislocation moves away from each other at all strains. This suggests that unlike glide, the climb motion remained energetically unfavorable at all the strains. Note that Fig. 5.14 shows the energies relative to the energy of the tube when both of the dislocation cores have climbed one step away from each other.

We used 750 elements with 420 nodes and enriched appropriate nodes using Eq. (5.24) for the XFEM calculations in comparison to 1360 atoms in the MM calculations. The material properties $E = 915$ GPa and $\nu = 0.4$ were calculated using the MTB-G2 potential. Note that the Young's modulus of [10,0] CNT is significantly different from that of a [15,15] CNT. This is one of the idiosyncracies of the MTB-G2 potential [4]. Quantum mechanical calculations clearly show the same Young's modulus for all the chiralities of CNTs, but the MTB-G2 potential predicts significantly different Young's moduli for CNTs of small radius with different chiralities [4].

As in the glide example, a small region around the dislocation core was omitted in the strain energy calculations. The energy in region was calculated by equating the strain energy of the tube after two climb steps, which is removal of six carbon atoms from the pristine tube, with the XFEM strain energy of the tube containing a dislocation dipole separated by same distance as in the MM calculations. Note that the removal of first pair of carbon atoms creates a dislocation pair and the removal of next two atom pairs moves the dislocation dipoles away. For these calculations quadrature points within a distance of 1.86 Å from the core were excluded.

The energies calculated using the XFEM are shown in Fig. 5.14(b). The results match quite well the MM calculations: the energy increases at all the strains with dislocation dipoles climb. Thus the climb motion of dislocation is not energetically favorable, however at very high temperatures this state can be achieved due to high thermal energies available to overcome the energy barrier.

5.4. Concluding Remarks

An extended-finite element method for dislocations was applied to model plasticity in CNTs. The formulation uses C^1 thin shell Kirchhoff-Love elements. An edge dislocation dipole was introduced using discontinuous and singular core enrichments. We calculate a finite strain energy by omitting a certain region around the dislocation cores. This region was calculated by comparing energy with the MM calculations. Excellent agreement was observed between the MM and XFEM calculations. Both MM and XFEM calculations

suggested that the glide mechanism becomes energetically favorable as the tensile strain is increased, which is in agreement with previous calculations [158, 159]. We also observed that for larger tubes higher strains are required for glide to become energetically favorable as they have less bending strain due to their high radius.

We also modeled the climb of prismatic dislocations using XFEM and MM. A step enrichment function was used to model the discontinuity caused by the removal of atoms from the lattice. We calculated the change in energy using both methods at different applied strains. Again very good agreement was seen between the XFEM and MM calculations. It was observed that energy always increased as dislocations climbed away from each other at all the strains, which suggests that the climb of dislocation is energetically unfavorable.

For large CNTs and multi-walled CNTs atomistic calculations can be computationally very expensive. XFEM simulations have been used to model both edge and prismatic dislocations without the requirement of remeshing with high accuracy and less computational cost compared to the atomistic solutions. Due to the simplicity of formulations it can easily be implemented into commercial softwares.

CHAPTER 6

Conclusions

We have given main conclusions of all the chapters at the end of each chapter. A summary is listed below:

∗ A bridging domain method based on overlapping domain decomposition has been developed for equilibrium shell problems for coupling atomistics with continuum mechanics. It uses Lagrange multipliers to impose displacement compatibility between the atomic lattice and the finite element mesh in the overlapping domain. This method does not require the finite element nodes to match the atomic positions at the interface.

∗ The quantum mechanical/molecular mechanical coupling scheme ONIOM was implemented to study the effect of large defects in carbon nanotubes and graphene sheets. The results of stress-strain curves calculated using the coupled scheme agree quite well with the benchmark pure quantum calculations. A scaling method was developed, which matches the molecular mechanical energy to the quantum mechanical energy over the entire range of the applied strains. This avoids unphysical behavior which may be caused by the difference between strength and stiffness of two models.

∗ A method for computing strains in discrete lattice structure based on the moving least squares approximation has been developed. It reproduces exact strain for a linear

displacement field when a linear basis is used and gives strain fields similar to the continuum strain fields near crack tip for atomistic model. An extension of the moving least squares strain calculation scheme for capturing the strain discontinuity at the material interfaces was developed.

∗ A new partial overlap quantum mechanical/molecular mechanical coupling scheme was developed, which does not require molecular mechanical calculation for the entire body thus allowing calculations for systems containing defected regions for which no reliable reactive empirical potentials are available.

∗ The fracture strengths of defected graphene sheets and carbon nanotubes decreases as the size of defect was increased thus contradicting the flaw-tolerance theory, which suggests that materials become flaw tolerant at nanoscale. Furthermore, it has been shown that the decrease in strength agrees quite closely with that predicted by Griffith theory for defects larger than two lattice constants.

∗ It was observed that the slits and holes of same length were reducing the strengths by same degree at nanoscale, which is in contrast with the standard fracture mechanics theory where cracks/slits cause much higher strain concentrations.

∗ An XFEM technique to model dislocation was implemented for modeling dislocations in carbon nanotubes. Excellent agreement was observed between the XFEM and MM calculations. Both XFEM and MM calculations suggested that the glide of dislocations in CNTs becomes energetically favorable as the applied strain is increased above a

certain strain. However, climb of the prismatic dislocation dipole remained energetically unfavorable for all tensile strains.

References

[1] S. Iijima. Helical microtubules of graphitic carbon. *Nature*, 354(6348):56–58, 1991.

[2] M.-F. Yu, O. Lourie, M. J. Dyer, K. Moloni, T. F. Kelly, and R. S. Ruoff. Strength and breaking mechanisms of multiwalled carbon nanotubes under tensile load. *Science*, 287:637–640, 2000.

[3] S. Zhang, S. L. Mielke, R. Khare, D. Troya, R. S. Ruoff, G. C. Schatz, and T. Belytschko. Mechanics of defects in carbon nanotubes: Atomistic and multiscale simulations. *Physical Review B*, 71:115403, 2005.

[4] S. L. Mielke, D. Troya, S. Zhang, J.-L. Li, S. Xiao, R. Car, R. S. Ruoff, G. C. Schatz, and T. Belytschko. The role of vacancy defects and holes in the fracture of carbon nanotubes. *Chemical Physics Letters*, 390(4–6):413–420, 2004.

[5] J. Kong, N. R. Franklin, C. W. Zhou, M. G. Chapline, S. Peng, K. J. Cho, and H. J. Dai. Nanotube molecular wires as chemical sensors. *Science*, 287(5453):622–625, 2000.

[6] J. Chen, M. A. Hamon, H. Hu, Y. S. Chen, A. M. Rao, P. C. Eklund, and R. C. Haddon. Solution properties of single-walled carbon nanotubes. *Science*, 282(5386):95–98, 1998.

[7] S. J. Tans, A. R. M. Verschueren, and C. Dekker. Room-temperature transistor based on a single carbon nanotube. *Nature*, 393(6680):49–52, 1998.

[8] A. Bachtold, P. Hadley, T. Nakanishi, and C. Dekker. Logic circuits with carbon nanotube transistors. *Science*, 294(5545):1317–1320, 2001.

[9] R. Martel, T. Schmidt, H. R. Shea, T. Hertel, and P. Avouris. Single- and multi-wall carbon nanotube field-effect transistors. 73(17):2447–2449, 1998.

[10] S. S. Fan, M. G. Chapline, N. R. Franklin, T. W. Tombler, A. M. Cassell, and H. J. Dai. Self-oriented regular arrays of carbon nanotubes and their field emission properties. *Science*, 283(5401):512–514, 1999.

[11] A. G. Rinzler, J. H. Hafner, P. Nikolaev, L. Lou, S. G. Kim, D. Tomanek, P. Nordlander, D. T. Colbert, and R. E. Smalley. Unraveling nanotubes - field-emission from an atomic wire. *Science*, 269(5230):1550–1553, 1995.

[12] D. Troya, S. L. Mielke, and G. C. Schatz. Carbon nanotube fracture – differences betweeen quantum mechanical mechanisms and those of empirical potentials. *Chemical Physics Letters*, 382(1–2):133–141, 2003.

[13] R. Khare, S. L. Mielke, J. T. Paci, S. L. Zhang, R. Ballarini, G. C. Schatz, and T. Belytschko. Coupled quantum mechanical/molecular mechanical modeling of the fracture of defective carbon nanotubes and graphene sheets. *Physical Review B*, 75(7):075412, 2007.

[14] F. F. Abraham, J. Q. Broughton, N. Bernstein, and E. Kaxiras. Spanning the length scales in dynamic simulation. *Comput. Phys.*, 12(6):538–546, 1998.

[15] R. E. Rudd and J. Q. Broughton. Concurrent coupling of length scales in solid state systems. *Phys. Status Solidi B*, 217:251–291, 2000.

[16] S. P. Xiao and T. Belytschko. A bridging domain method for coupling continua with molecular dynamics. *Computer Methods in Applied Mechanics and Engineering*, 193:1645–1669, 2004.

[17] M. Xu and T. Belytschko. Conservation properties of the bridging domain method for coupled molecular/continuum dynamics. *International Journal for Numerical Methods in Engineering*, in press, 2008.

[18] W. E, B. Engquist, X. T. Li, W. Q. Ren, and E. Vanden-Eijnden. Heterogeneous multiscale methods: A review. *Communications in Computational Physics*, 2(3):367–450, 2007.

[19] G. J. Wagner and W. K. Liu. Coupling of atomistic and continuum simulations using a bridging scale decomposition. *J. Comput. Phys.*, 190(1):249–274, 2003.

[20] H. S. Park, E. G. Karpov, and W. K. Liu. Non-reflecting boundary conditions for atomistic, continuum and coupled atomistic/continuum simulations. *International Journal for Numerical Methods in Engineering*, 64(2):237–259, 2005.

[21] L. E. Shilkrot, R. E. Miller, and W. A. Curtin. Multiscale plasticity modeling: coupled atomistics and discrete dislocation mechanics. *Journal of the Mechanics and Physics of Solids*, 52(4):755–787, 2004.

[22] W. Chen and J Fish. A generalized space-time mathematical homogenization theory for bridging atomistic and continuum scales. *International Journal for Numerical*

Methods in Engineering, 67(2):253–271, 2006.

[23] W. A. Curtin and R. E. Miller. Atomistic/continuum coupling in computational materials science. *Modelling and Simulations in Materials Science and Engineering*, 11(3):R33–R68, 2003.

[24] N. M. Ghoniem, E. P. Busso, N. Kioussis, and H. Huang. Multiscale modelling of nanomechanics and micromechanics: an overview. *Philosophical Magazine*, 83:3475–3528, 2003.

[25] W. K. Liu, E. G. Karpov, S. Zhang, and H. S. Park. An introduction to computational nanomechanics and materials. *Computer Methods in Applied Mechanics and Engineering*, 193(17–20):1529–1732, 2004.

[26] E. B. Tadmor, M. Ortiz, and R. Phillips. Quasicontinuum analysis of defects in solids. *Philos. Mag. A*, 73:1529–1563, 1996.

[27] S. Zhang, R. Khare, T. Belytschko, K. J. Hsia, S. L. Mielke, and G. C. Schatz. Transition states and minimum energy pathways for the collapse of carbon nanotubes. *Physical Review B*, 73(7):075423, 2006.

[28] V. B. Shenoy, R. Miller, E. B. Tadmor, R. Phillips, and M. Ortiz. Quasicontinuum models of interfacial structure and deformation. *Physical Review Letters*, 80(4):742–745, 1998.

[29] U. C. Singh and P. Kollman. A combined ab initio quantum mechanical and molecular mechanical method for carrying out simulations on complex molecular systems: Applications to the CH3Cl + Cl- exchange reaction and gas phase protonation of

polyethers. *Journal of Computational Chemistry*, 7(6):718, 1986.

[30] F. Maseras and K. Morokuma. IMOMM - a new integrated ab-initio plus molecular mechanics geometry optimization scheme of equilibrium structures and transition-states. *Journal of Computational Chemistry*, 16:1170, 1995.

[31] K. P. Eurenius, D. C. Chatfield, B. R. Brooks, and M. Hodoscek. Enzyme mechanisms with hybrid quantum and molecular mechanical potentials .1. Theoretical considerations. *International Journal of Quantum Chemistry*, 60:1189, 1996.

[32] M. Svensson, S. Humbel, D. D. J. Froese, T. Matsubara, and S. Sieber K. Morokuma. ONIOM: A multilayered integrated MO+MM method for geometry optimizations and single point energy predictions. A test for Diels-Alder reactions and Pt(P(t-Bu)(3))(2)+H-2 oxidative addition. 100:19357, 1994.

[33] M. J. Field, P. A. Bash, and M. Karplus. A combined quantum mechanical and molecular mechanical potential for molecular dynamics simulations. *Journal of Computational Chemistry*, 11:700, 1990.

[34] D. Das, K. P. Eurenius, and E. M. Billings. Optimization of quantum mechanical molecular mechanical partitioning schemes: Gaussian delocalization of molecular mechanical charges and the double link atom method. 117(23):10534, 2002.

[35] M. Swart. Addremove: A new link model for use in QM/MM studies. *International Journal of Quantum Chemistry*, 91:177, 2002.

[36] Y. K. Zhang, T. S. Lee, and W. T. Yang. A pseudobond approach to combining quantum mechanical and molecular mechanical methods. *Journal of Chemical*

Physics, 110(1):46–54, 1999.

[37] V. Thery, D. Rinaldi, and J.-L. Rivail. Quantum mechanical computations on very large molecular systems: the local self-consistent field method. *Journal of Computational Chemistry*, 15:269, 1994.

[38] X. Assfeld and J. L. Rivail. Quantum chemical computations on parts of large molecules: The ab initio local self consistent field method. *Chemical Physics Letters*, 263(1-2):100–106, 1996.

[39] J. Gao, P. Amara, C. Alhambra, and M. J. Field. A generalized hybrid orbital (GHO) method for treatment of boundary atoms in combined QM/MM calculations. 102:4714, 1998.

[40] Arianna Fornili, Pierre-Francois Loos, Maurizio Sironi, and Xavier Assfeld. Frozen core orbitals as an alternative to specific frontier bond potential in hybrid quantum mechanics/molecular mechanics methods. *Chemical Physics Letters*, 427(1-3):236–240, 2006.

[41] M. S. Gordon, M. A. Freitag, P. Bandyopadhyay, J. H. Jensen, V. Kairys, and W. J. Stevens. The effective fragment potential method: A qm-based mm approach to modeling environmental effects in chemistry. *J. Phys. Chem. A*, 105(2):293–307, 2001. 1089-5639.

[42] J. Pu, J. Gao, and D. G. Truhlar. Generalized hybrid orbital (gho) method for combining ab initio hartree-fock wave functions with molecular mechanics. *J. Phys. Chem. A*, 108(4):632–650, 2004. 1089-5639.

[43] J. Pu, J. Gao, and D. G. Truhlar. Combining self-consistent-charge density-functional tight-binding (scc-dftb) with molecular mechanics by the generalized hybrid orbital (gho) method. *J. Phys. Chem. A*, 108(25):5454–5463, 2004. 1089-5639.

[44] N. Reuter, A. Dejaegere, B. Maigret, and M. Karplus. Frontier bonds in qm/mm methods: A comparison of different approaches. *J. Phys. Chem. A*, 104(8):1720–1735, 2000. 1089-5639.

[45] T. Belytschko and T. Black. Elastic crack growth in finite elements with minimal remeshing. *International Journal for Numerical Methods in Engineering*, 45(5):601–620, 1999.

[46] T. Belytschko, N. Moes, S. Usui, and C. Parimi. Arbitrary discontinuities in finite elements. *International Journal for Numerical Methods in Engineering*, 50(4):993–1013, 2001.

[47] N. Moes, J. Dolbow, and T. Belytschko. A finite element method for crack growth without remeshing. *International Journal for Numerical Methods in Engineering*, 46(1):131–150, 1999.

[48] J. M. Melenk and I. Babuska. The partition of unity finite element method: Basic theory and applications. *Computer Methods in Applied Mechanics and Engineering*, 139(1-4):289–314, 1996.

[49] J. H. Song, P. M. A. Areias, and T. Belytschko. A method for dynamic crack and shear band propagation with phantom nodes. *International Journal for Numerical Methods in Engineering*, 67(6):868–893, 2006.

[50] J. Chessa and T. Belytschko. An extended finite element method for two-phase fluids. *Journal of Applied Mechanics-Transactions of the Asme*, 70(1):10–17, 2003.

[51] R. J. Amodeo and N. M. Ghoniem. Dislocation dynamics . I. a proposed methodology for deformation micromechanics. *Physical Review B*, 41(10):6958–6967, 1990. Part B.

[52] E. Vandergiessen and A. Needleman. Discrete dislocation plasticity - a simple planar model. *Modelling and Simulation in Materials Science and Engineering*, 3(5):689–735, 1995.

[53] H. M. Zbib, M. Rhee, and J. P. Hirth. On plastic deformation and the dynamics of 3d dislocations. *International Journal of Mechanical Sciences*, 40(2-3):113–127, 1998.

[54] R. Gracie, G. Ventura, and T. Belytschko. A new fast finite element method for dislocations based on interior discontinuities. *International Journal for Numerical Methods in Engineering*, 69(2):423–441, 2007.

[55] T. Belytschko and R. Gracie. On xfem applications to dislocations and interfaces. *International Journal of Plasticity*, 23(10-11):1721–1738, 2007.

[56] R. Gracie, J. Oswald, and T. Belytschko. On a new extended finite element method for dislocations: Core enrichment and nonlinear formulation. *Journal of the Mechanics and Physics of Solids*, In press.

[57] T. Belytschko and S. P. Xiao. Coupling methods for continuum model with molecular model. *International Journal for Multiscale Computational Engineering*,

1(1):115–126, 2003.

[58] H. B. Dhia and G. Rateau. The Arlequin method as a flexible engineering desing tool. *International Journal for Numerical Methods in Engineering*, 62:1442–1462, 2005.

[59] P. H. Mott, A. S. Argon, and U. W. Suter. The atomic strain tensor. 101:140–150, 1992.

[60] D. C. Liu and J. Nocedal. On the limited memory method for large scale optimization. *Mathematical Programming B*, 45(3):503–528, 1989.

[61] C. Farhat and F. X. Roux. A method of finite element tearing and interconnecting and its parallel solution algorithm. *International Journal for Numerical Methods in Engineering*, 32:1205–1227, 1991.

[62] C. Farhat, J. Li, and P. Avery. A FETI-DP method for parallel iterative solution of indefinite and complex-valued solid and shel vibration problems. *International Journal for Numerical Methods in Engineering*, 63(3):398–427, 2005.

[63] T. Belystchko, W. K. Liu, and B. Moran. Nonlinear finite elements for continua and structures. John Wiley & Sons Ltd, 2001.

[64] T. Belytschko, Y. Y. Lu, and L. Gu. Element-free Galerkin methods. *International Journal for Numerical Methods in Engineering*, 37:229–256, 1994.

[65] T. Belytschko, Y. Krongauz, D. Organ, M. Fleming, and P. Krysl. Meshless methods: An overview and recent developments. *Computer Methods in Applied Mechanics and Engineering*, 139(1-4):3–47, 1996.

[66] A. Huerta and S. F. Mendez. Enrichment and coupling of the finite element and meshless methods. *International Journal for Numerical Methods in Engineering*, 48:1615–1636, 2000.

[67] M. Arroyo and T. Belytschko. Finite element methods for the non-linear mechanics of crystalline sheets and nanotubes. *International Journal for Numerical Methods in Engineering*, 59:419–456, 2004.

[68] L. E. Shilkrot, W. A. Curtin, and R. E. Miller. A coupled atomistic/continuum model of defects in solids. *Journal of the Mechanics and Physics of Solids*, 50(10):2085–2106, 2002.

[69] O. A. Shenderova, D. W. Brenner, A. Omeltchenko, X. Su, and L. H. Yang. Atomistic modeling of the fracture of polycrystalline diamond. *Physical Review B*, 61(6):3877–3888, 2000.

[70] M. Arroyo and T. Belytschko. Finite crystal elasticity of carbon nanotubes based on the exponential Cauchy-Born rule. *Physical Review B*, 69(14):115415, 2004.

[71] M. Arroyo and T. Belytschko. A finite deformation membrane based on inter-atomic potentials for the transverse mechanics of nanotubes. *Mechanics of Materials*, 35(3-6):193–215, 2003.

[72] F. Cirak, M. Ortiz, and P. Schroeder. Subdivision surfaces: a new paradigm for thin-shell finite-element analysis. *Computer Methods in Applied Mechanics and Engineering*, 193:1645–1669, 1999.

[73] T. Ozaki, Y. Iwasa, and T. Mitani. Stiffness of single-walled carbon nanotubes under large strain. *Physical Review Letters*, 84(8):1712–1715, 2000.

[74] T. Dumitrica, T. Belytschko, and B. I. Yakobson. Bond–breaking bifurcaion states in carbon nanotube fracture. *J. Chem. Phys.*, 118(21):9485–9488, 2003.

[75] S. Ogata and Y. Shibutani. Ideal tensile strength and band gap of single-walled carbon nanotubes. *Physical Review B*, 68:165409, 2003.

[76] G. Dereli and C. Ozdogan. Structural stability and energetics of single–walled carbon nanotubes under uniaxial strain. *Physical Review B*, 67:035416, 2003.

[77] T. Dumitrica, M. Hua, and B. I. Yakobson. Symmetry-, time-, and temperature-dependent strength of carbon nanotubes. 103(16):6105–6109, 2006.

[78] A. G. Rinzler, J. Liu, H. Dai, P. Nikolaev, C. B. Huffman, F. J. Rodriguez-macias, P. J. Boul, A. H. Lu, D. Heymann, D. T. Colbert, R. S. Lee, J. E. Fischer, A. M. Rao, P. C. Eklund, and R. E. Smalley. Large-scale purification of single-wall carbon nanotubes: process, product, and characterization. *Appl. Phys. A*, 67(1):29–34, 1998.

[79] R. C. Haddon, J. Sippel, A. G. Rinzler, and F. Papadimitrakopoulos. *MRS Bulletin*, 29(4):252–259, 2004.

[80] Y.-Q. Xu, H. Peng, R. H. Hauge, and R. E. Smalley. *Nano Lett.*, 5(1):163–168, 2005.

[81] S. L. Mielke, T. Belytschko, and G. C. Schatz. *Annu. Rev. Phys. Chem*, 58:185, 2007.

[82] H. C. Schniepp, J.-L. Li, M. J. McAllister, H. Sai, M. Herrera-Alonso, D. H. Adamson, R. K. Prud'homme, R. Car, D. A. Saville, and I. A. Aksay. Functionalized single graphene sheets derived from splitting graphite oxide. *J. Phys. Chem. A*, 110:8535–8539, 2006.

[83] T. Belytschko, S. P. Xiao, G. C. Schatz, and R. S. Ruoff. Atomistic simulations of nanotube fracture. *Physical Review B*, 65:235430, 2002.

[84] D. W. Brenner, O. A. Shenderova, J. A. Harrison, S. J. Stuart, B. Ni, and S. B. Sinnott. A second-generation reactive empirical bond order (REBO) potential energy expression for hydrocarbons. *Journal of Physics: Condensed Matter*, 14:783–802, 2002.

[85] R. Thomson, C. Hsieh, and V. Rana. Lattice trapping of fracture cracks. *Journal of Applied Physics*, 42(8):3154–3160, 1971.

[86] J. R. Rice. *Journal of the Mechanics and Physics of Solids*, 26(2):61–78, 1978.

[87] W. A. Curtin. On lattice trapping of cracks. *Journal of Materials Research*, 5(7):1549–1560, 1990.

[88] N. Bernstein and D. W. Hess. Lattice trapping barriers to brittle fracture. *Physical Review Letters*, 91(2):025501, 2003.

[89] J. R. Rice. A path independent integral and approximate analysis of strain concentraion by notches and cracks. *Journal of Applied Mechanics*, 35(2):379–386, 1968.

[90] M. W. Schmidt, K. K. Baldridge, J. A. Boatz, S. T. Elbert, M. S. Gordon, J. H. Jensen, S. Koseki, N. Matsunaga, K. A. Nguyen, S. J. Su, T. L. Windus, M. Dupuis,

and J. A. Montgomery. General atomic and molecular electronic structure system. *Journal of Computational Chemistry*, 14(11):1347–1363, 1993.

[91] D. Sánchez-Portal, P. Ordejón, E. Artacho, and J. M. Soler. Density-functional method for very large systems with lcao basis sets. *International Journal of Quantum Chemistry*, 65:453–461, 1997.

[92] J. M. Soler, E. Artacho, J. D. Gale, A. García, J. Junquera, P. Ordejón, and D. Sánchez-Portal. The siesta method for ab initio order-n materials simulation. *J. Phys.: Condens. Matter*, 14(11):2745–2779, 2002.

[93] N. Troullier and J. L. Martins. Efficient pseudopotentials for plane-wave calculations. *Phys. Rev. B*, 43(3):1993–2006, 1991.

[94] N. Troullier and J. L. Martins. Efficient pseudopotentials for plane-wave calculations .2. operators for fast iterative diagonalization. *Phys. Rev. B*, 43(11):8861–8869, 1991.

[95] J. J. Koval. Variable metric function minimization. *Appl. Stat.–J. Roy. St. C*, 46(4):515–521, 1997.

[96] M. Arroyo and T. Belytschko. An atomistic-based finite deformation membrane for single layer crystalline films. *Journal of the Mechanics and Physics of Solids*, 50(9):1941–1977, 2002.

[97] A. J. Stone and D. J. Wales. Theoretical studies of icosahedral C60 and some related species. *Chemical Physics Letters*, 128(5–6):501–503, 1986.

[98] A. A. Griffith. The phenomena of rupture and flow in solids. *Philos. Trans. R. Soc. London, Ser. A*, 211:163–198, 1920.

[99] T. L. Anderson. *Fracture Mechanics: Fundamentals and Applications*. CRC press, 1991.

[100] D. Vogtenhuber and R. Podloucky. *Physical Review B*, 55(16):10805–10813, 1997.

[101] A. Mattoni, L. Colombo, and F. Cleri. *Physical Review Letters*, 95(11):115501, 2005.

[102] M. Ippolito, A. Mattoni, L. Colombo, and N. Pugno. *Physical Review B*, 73(10):104111, 2006.

[103] J. A. Moriarty, J. F. Belak, R. E. Rudd, P. Soderlind, F. H. Streitz, and L. H. Yang. Quantum-based atomistic simulation of materials properties in transition metals. *Journal of Physics: Condensed Matter*, 14(11):2825–2857, 2002.

[104] A. Mallik, D. E. Taylor, K. Runge, J. W. Dufty, and H. P. Cheng. Procedure for building a consistent embedding at the qm-cm interface. 13(1-3):45–60, 2006.

[105] S. Ogata, E. Lidorikis, F. Shimojo, A. Nakano, P. Vashishta, and R. K. Kalia. Hybrid finite-element/molecular-dynamics/electronic-density-functional approach to materials simulations on parallel computers. 138(2):143–154, 2001.

[106] R. Belkada, T. Igarashi, and S. Ogata. Effects of h2o on si fracture: a hybrid quantum-classical simulation. *Computational Materials Science*, 30:195–201, 2004.

[107] C. L. Rountree, R. K. Kalia, E. Lidorikis, A. Nakano, L. V. Brutzel, and P. Vashishta. Atomistic aspects of crack propagation in brittlematerials: Multimillion atom molecular dynamics simulations. 32:377–400, 2002.

[108] P. M. Ajayan, V. Ravikumar, and J.-C. Charlier. Surface reconstructions and dimensional changes in single-walled carbon nanotubes. *Physical Review Letters*,

81(7):1437–1440, 1998.

[109] A. V. Krasheninnikov, K. Nordlund, M. Sirvio, E. Salonen, and J. Keinonen. Formation of ion-irradiation-induced atomic-scale defects on walls of carbon nanotubes. *Physical Review B*, 63:245405, 2001.

[110] D. Troya, S. L. Mielke, and G. C. Schatz. Unpublished.

[111] H. F. Bettinger. *Organic Letters*, 6(2):731, 2004.

[112] Z. Y. Zhou, M. Steigerwald, M. Hybertsen, L. Brus, and R. A. Friesner. 126(11):3597–3607, 2004.

[113] R. Pérez and P. Gumbsch. *Physical Review Letters*, 84(23):5347–5350, 2000.

[114] H. Gao, B.-H. Ji, I. L. Jager, E. Arzt, and P. Fratzl. Materials become insensitive to flaws at nanoscale: Lessons from nature. *P. Natl. Acad. Sci. USA,*, 100(10):5597–5600, 2003.

[115] R. Ballarini, R. Kayacan, F. J. Ulm, T. Belytschko, and A. H. Heuer. Biological structures mitigate catastrophic fracture through various strategies. *International Journal of Fracture*, 135(1-4):187–197, 2005.

[116] A. Omeltchenko, J. Yu, R. K. Kalia, and P. Vashishta. Crack front propagation and fracture in a graphite sheet: A molecular dynamics study on parallel computers. *Physical Review Letters*, 78(11):2148–2151, 1997.

[117] B. Moran and C. F. Shih. Crack tip and associated domain integrals from momentum and energy balance. *Engineering Fracture Mechanics*, 27(6):615–642, 1987.

[118] K. Nakatani, A. Nakatani, Y. Sugiyama, and H. Kitagawa. *AIAA Journal*, 38(4):695–701, 2000.

[119] Y. Jin and F. G. Yuan. Atomistic simulations of j-integral in 2d graphene nanosystems. 5:2099–2107, 2005.

[120] A. G. Mclellan. Virial theorem generalized. *American Journal of Physics*, 42(3):239–243, 1974.

[121] A. Warshel and M. Levitt. Theoretical studies of enzymic reactions-dielectric, electrostatic and steric stabilization of carbonium-ion in reaction of lysozome. 103(2):227, 1976.

[122] D. E. Hill, Y. Lin, A. M. Rao, L. F. Allard, and Y. P. Sun. Functionalization of carbon nanotubes with polystyrene. *Macromolecules*, 35(25):9466–9471, 2002.

[123] H. Jiang, X.-Q. Feng, Y. Huang, K. C. Hwang, and P. D. Wu. Defect nucleation in carbon nanotubes under tension and torsion: Stonewales transformation. *Comput. Methods Appl. Mech. Eng.*, 193:34193429, 2004.

[124] E.T. Mickelson, C.B. Huffman, A.G. Rinzler, R.E. Smalley, R.H. Hauge, and J.L. Margrave. Fluorination of single-wall carbon nanotubes. *Chem. Phys. Lett.*, 296:188–194, 1998.

[125] T. Ramanathan, F. T. Fisher, R. S. Ruoff, and L. C. Brinson. Amino-functionalized carbon nanotubes for binding to polymers and biological systems. *Chemistry of Materials*, 17(6):1290–1295, 2005.

[126] S. Zhang, R. Khare, Q. Lu, and T. Belytschko. A bridging domain method for coupled atomistc-continuum modeling of solids. *International Journal for Numerical Methods in Engineering*, 70:913–933, 2007.

[127] E. G. Karpov, H. S. Park, and W. K. Liu. A phonon heat bath approach for the atomistic and multiscale simulation of solids. *International Journal for Numerical Methods in Engineering*, 70(3):351–378, 2007.

[128] W. Chen and J. Fish. A generalized space-time mathematical homogenization theory for bridging atomistic and continuum scales. *International Journal for Numerical Methods in Engineering*, 67(2):253–271, 2006.

[129] Fish J., Mohan A., M. A. Nuggehally, M. S. Shephard, C. R. Picud, C. Badia, M. L. Parks, and M. Gunzburger. Concurrent atc coupling based on a blend of the continuum stress and the atomistic force. *Computer Methods in Applied Mechanics and Engineering*, 196:4548–4560, 2007.

[130] P. A. Guidault and T. Belytschko. On the l2 and the h1 couplings for an overlapping domain decomposition method using lagrange multipliers. *International Journal for Numerical Methods in Engineering*, 70(3):322–350, 2007.

[131] C. Berger, Z. M. Song, T. B. Li, X. B. Li, A. Y. Ogbazghi, R. Feng, Z. T. Dai, A. N. Marchenkov, E. H. Conrad, P. N. First, and W. A. de Heer. Ultrathin epitaxial graphite: 2d electron gas properties and a route toward graphene-based nanoelectronics. *J. of Phys. Chem. B*, 108(52):19912–19916, 2004.

[132] K. S. Novoselov, A. K. Geim, S. V. Morozov, D. Jiang, Y. Zhang, S. V. Dubonos, I. V. Grigorieva, and A. A. Firsov. Electric field effect in atomically thin carbon films. *Science*, 306(5696):666–669, 2004.

[133] Y. B. Zhang, Y. W. Tan, H. L. Stormer, and P. Kim. Experimental observation of the quantum hall effect and berry's phase in graphene. *Nature*, 438(7065):201–204, 2005.

[134] W. Lee, J. M. Myoung, Y. H. Yoo, and H. Shin. Effect of elastic anisotropy on the strain fields and band edges in stacked inas/gaas quantum dot nanostructures. *Solid State Communications*, 132(2):135–140, 2004.

[135] M. A. Migliorato, A. G. Cullis, M. Fearn, and J. H. Jefferson. Atomistic simulation of strain relaxation in inxga1-xas/gaas quantum dots with nonuniform composition. *Physical Review B*, 65(11):115316, 2002.

[136] H. Shin, J. B. Kim, Y. H. Yoo, W. Lee, E. Yoon, and Y. M. Yu. Enhanced strain of inas quantum dots by an ingaas ternary layer in a gaas matrix. *Journal of Applied Physics*, 99(2), 2006.

[137] H. Shin, W. Lee, and Y. H. Yoo. Comparison of strain fields in truncated and untruncated quantum dots in stacked inas/gaas nanostructures with varying stacking periods. *Journal of Physics-Condensed Matter*, 15(22):3689–3699, 2003.

[138] H. Shin, W. Lee, and Y. H. Yoo. Effect of the stacking period on the strain field in inas/gaas quantum dots. *Nanotechnology*, 14(7):742–747, 2003.

[139] V.-G. Stoleru, D. Pal, and E. Towe. Self-assembled (in,ga)as/gaas quantum-dot nanostructures: strain distribution and electronic structure. *Physica E Low Dimensional Systems and Nanostructures*, 15(3):131–152, 2002.

[140] Y. H. Yoo, W. Lee, and H. Shin. Effect of wire width on strain distribution and bandgap in laterally aligned ingaas/gaas quantum wire nanostructures. *Semiconductor Science and Technology*, 19(1):93–99, 2004.

[141] D. A. Faux, G. Jones, and E. P. O' Reilly. Calculation of strain relaxation in strained-layer structures: comparison of atomistic and continuum methods. *Modelling and Simulation in Materials Science and Engineering*, 2(1):9–20, 1994.

[142] J. Li. Atomistic calculation of mechanical behavior. In S. Yip, editor, *Handbook of materials modeling*, volume chapter 2.19. Kluwer Academic Publishers, 2005.

[143] Z. Chen, S. Nagase, A. Hirsch, R. C. Haddon, W. Thiel, and P. von R. Schleyer. Sidewall opening of single-walled carbon nanotubes (swcnts) by chemical modification: A critical theoretical study. *Angewandte Chemie-International Edition*, 43(12):1552–1554, 2004.

[144] R. Khare, S. L. Mielke, J. T. Paci, S. Zhang, G. C. Schatz, and T. Belytschko. Two quantum mechanical/molecular mechanical coupling schemes appropriate for fracture mechanics studies. *AIAA 2007*, 2171, 2007.

[145] R. Khare, S. L. Mielke, J. T. Paci, G. C. Schatz, and T. Belytschko. to be submitted.

[146] T. Belytschko, N. Moes, S. Usui, and C. Parimi. Arbitrary discontinuities in finite elements. *International Journal for Numerical Methods in Engineering*, 50(4):993–1013, 2001.

[147] J. J. P. Stewart. *Journal of Computational Chemistry*, 2:209, 1989.

[148] A. H. Barber, R. Andrews, L. S. Schadler, and H. D. Wagner. On the tensile strength distribution of multiwalled carbon nanotubes. *Applied Physics Letters*, 87(20), 2005.

[149] M.-F. Yu, B. S. Files, S. Arepalli, and R. S. Ruoff. Tensile loading of ropes of single wall carbon nanotubes and their mechanical properties. *Physical Review Letters*, 84(24):5552–5555, 2000.

[150] R. Khare, S. L. Mielke, G. C. Schatz, and T. Belytschko. Multiscale coupling schemes spanning the quantum mechanical, atomistic forcefield, and continuum regimes. *Computer Methods in Applied Mechanics and Engineering*, doi:10.1016/j.cma.2007.11.029, 2007.

[151] Y. Hirai, S. Nishimaki, H. Mori, Y. Kimoto, S. Akita, Y. Nakayama, and Y. Tanaka. Molecular dynamics studies on mechanical properties of carbon nanotubes with pinhole defects. *Japanese Journal of Applied Physics*, 42:4120–4123, 2003.

[152] Q. Lu and B. Bhattacharya. Effect of randomly occurring stone-wales defects on mechanical properties of carbon nanotubes using atomistic simulation. *Nanotechnology*, 16(4):555–566, 2005.

[153] J. Y. Huang, S. Chen, Z. Q. Wang, K. Kempa, Y. M. Wang, S. H. Jo, G. Chen, M. S. Dresselhaus, and Z. F. Ren. Superplastic carbon nanotubes - conditions have

been discovered that allow extensive deformation of rigid single-walled nanotubes. *Nature*, 439(7074):281–281, 2006.

[154] J. Y. Huang, S. Chen, Z. F. Ren, Z. Q. Wang, D. Z. Wang, M. Vaziri, Z. Suo, G. Chen, and M. S. Dresselhaus. Kink formation and motion in carbon nanotubes at high temperatures. *Physical Review Letters*, 97(7), 2006.

[155] M. B. Nardelli, B. I. Yakobson, and J. Bernholc. Brittle and ductile behavior in carbon nanotubes. *Physical Review Letters*, 81(21):4656–4659, 1998b.

[156] J. P. Hirth and J. Lothe. Theory of dislocations. Wiley, New York, 1982.

[157] F. Ding, K. Jiao, M. Q. Wu, and B. I. Yakobson. Pseudoclimb and dislocation dynamics in superplastic nanotubes. *Physical Review Letters*, 98(7), 2007.

[158] H. Mori, S. Ogata, J. Li, S. Akita, and Y. Nakayama. Energetics of plastic bending of carbon nanotubes. *Physical Review B*, 74(16), 2006.

[159] S. Zhang and T. Zhu. Atomic geometry and energetics of carbon nanotube necking. *Philosophical Magazine Letters*, 87(8):567–574, 2007.

[160] B. I. Yakobson, C. J. Brabec, and J. Bernholc. Nanomechanics of carbon tubes: Instabilities beyond linear response. *Physical Review Letters*, 76(14):2511–2514, 1996.

[161] C. Q. Ru. Column buckling of multiwalled carbon nanotubes with interlayer radial displacements. *Physical Review B*, 62(24):16962–16967, 2000.

[162] C. Q. Ru. Axially compressed buckling of a doublewalled carbon nanotube embedded in an elastic medium. *Journal of the Mechanics and Physics of Solids*, 49(6):1265–1279, 2001.

[163] G. Ventura, B. Moran, and T. Belytschko. Dislocations by partition of unity. *International Journal for Numerical Methods in Engineering*, 62(11):1463–1487, 2005.

[164] V. Volterra. Sur lquilibre des corps lastiques multiplement connexes. *Annales Scientifiques de lcole Normale*, 24:401–517, 1907.

[165] F. Cirak, M. Ortiz, and P. Schroder. Subdivision surfaces: a new paradigm for thin-shell finite-element analysis. *International Journal for Numerical Methods in Engineering*, 47(12):2039–2072, 2000.

[166] F. Cirak and M. Ortiz. Fully c-1-conforming subdivision elements for finite deformation thin-shell analysis. *International Journal for Numerical Methods in Engineering*, 51(7):813–833, 2001.

[167] J. Tersoff. Empirical interatomic potential for carbon, with applications to amorphous carbon. *Physical Review Letters*, 61(25):2879–2882, 1988.

APPENDIX A

A simple energy-scaling scheme for fine-tuning empirical potentials for use in coupled quantum mechanical/molecular mechanical fracture mechanics studies

Reactive empirical potentials such as the bond-order potentials of Tersoff [167] and Brenner et al. [84] allow fracture processes to be modeled by molecular mechanical (MM) methods. Unfortunately, as we have previously observed in Chapter 3, these potentials do not always predict fracture mechanisms for defected structures with even qualitative accuracy; thus, quantum mechanical (QM) methods are required to obtain accurate results, and the expense associated with QM calculations makes coupled QM/MM approaches necessary for the treatment of large systems. The strategy for such QM/MM calculations, as explained in this thesis, is to treat the subdomains containing defects by QM methods and to treat the rest of the system by MM methods. A crucial presumption of such an approach is that the MM and QM potentials are sufficiently similar, at least in the treatment of undefected regions, that they are compatible. When this presumption does not hold, mismatches between the MM and QM interactions can lead to unphysical behavior [13].

Ideally, when performing multiscale calculations, the empirical potentials would be re-optimized to closely match the QM properties of the system being studied, but this can be a laborious task and is rarely feasible. In the following we present a simple strain-dependent energy-scaling scheme that can be used to tailor the mechanical properties of the MM potential so that they closely match those of the QM interactions. This method will be presented in the context of fracture calculations of a defected graphene sheet.

For the present study we have adopted the two-level ONIOM scheme [32] explained in Chapter 3 and 4 to couple the MM model with the QM model. The total energy E of the system is then given by

$$E = E^{\mathrm{MM}} + E_{\mathrm{F}}^{\mathrm{QM}} - E_{\mathrm{F}}^{\mathrm{MM}}, \tag{A.1}$$

where E^{MM} is the MM energy of the entire system, and $E_{\mathrm{F}}^{\mathrm{QM}}$ and $E_{\mathrm{F}}^{\mathrm{MM}}$ are the QM and MM energies of a special subdomain, or fragment, where more accurate calculations are desired. Spin-unrestricted QM calculations were done using the semi-empirical method PM3 and a second generation modified Tersoff-Brenner potential (MTB-G2) [84, 4, 3] was used for the MM interactions. Except as indicated below, the numerical details of the calculations are the same as in Chapter 3.

Unfortunately, the mechanical properties (i.e., modulus, failure stress, and failure strain) predicted by the empirical MTB-G2 potential are all significantly lower than those

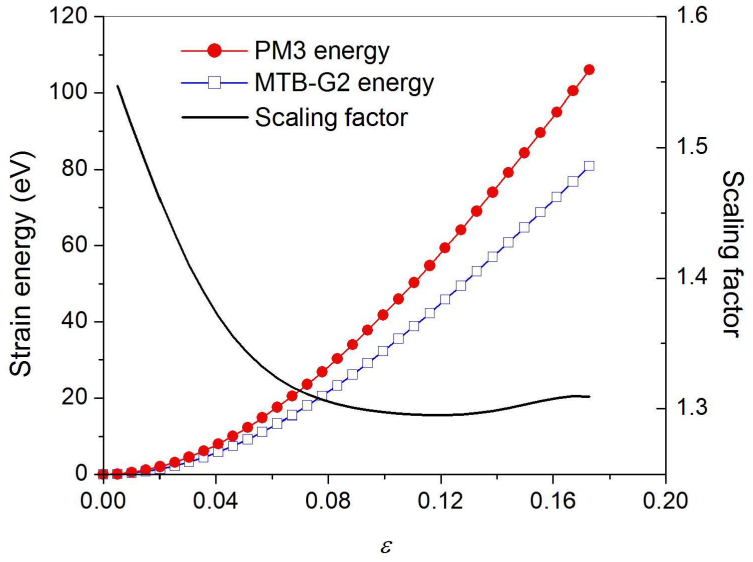

Figure A.1. Strain energy versus strain curves (left axis) obtained for a pristine graphene sheet using PM3 and MTB-G2 and the resulting strain dependent scale factor (right axis).

predicted by the PM3 QM calculations, as shown in Chapter 3. When QM/MM calculations are performed with these two interactions, dramatically unphysical behavior can occur. In particular, we have observed fracture within undefected MM subdomains even when these are coupled to QM subdomains containing significant defects. In Chapter 3, the MTB-G2 potential was scaled by a constant factor to roughly match the strength and stiffness of the material calculated using the QM method. This constant-scaling-factor approach prevents highly spurious behavior, but for a non-linear material such as graphene this approach is still insufficient to accurately match the mechanical properties of the two models in the non-linear regime. Mismatched behavior near the fracture point can result in inaccurate fracture stress and strain when compared to a strictly QM calculation.

We now consider a more general scaling scheme to permit better consistency between the mechanical behavior of the MM and QM methods over the full range of strains occurring in a fracture process. In particular, we take the MM energy to be

$$E^{\mathrm{MM}} = \eta(\varepsilon) E^{\text{MTB-G2}}, \tag{A.2}$$

where η is a strain-dependent scaling factor calculated as

$$\eta(\varepsilon) = \frac{E^{\mathrm{QM}}(\varepsilon)}{E^{\text{MTB-G2}}(\varepsilon)}, \tag{A.3}$$

where ε is the Green strain, and $E^{\mathrm{QM}}(\varepsilon)$ and $E^{\text{MTB-G2}}(\varepsilon)$ are the strain energies of a graphene sheet as a function of strain that are obtained from strictly QM or strictly MM calculations, respectively, of an undefected sample. Note that strain energy of a system is the total energy at any strain minus the energy of the zero strain configuration. Figure A.1 shows $E^{\mathrm{QM}}(\varepsilon)$ and $E^{\text{MTB-G2}}(\varepsilon)$ for a small undefected graphene sheet and also shows the resulting variation of with for a graphene sheet. The sheet was stretched in a direction perpendicular to the zigzag edge with the degrees of freedom in the direction of stretch fixed of the carbon atoms on boundaries perpendicular to the stretching direction.

However, this model requires calculation of a different $\eta(\varepsilon)$ using Eq. (A.3) for a different loading, which may be a tedious task. Here we also propose a simple scheme to calculate the variation of the scaling factor with strains for any type of loading conditions

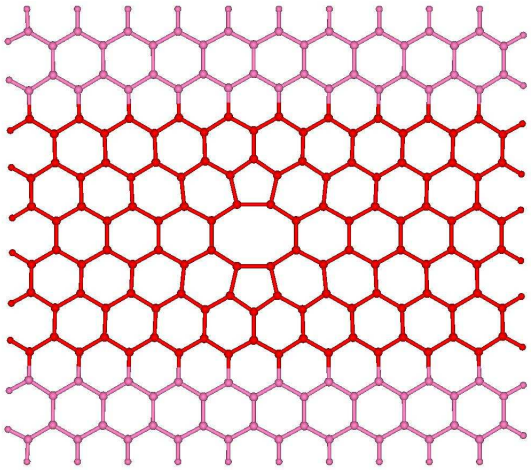

Figure A.2. QM/MM model of a graphene sheet containing a two-atom vacancy defect. The dark red atoms constitute the QM fragment and the light blue atoms form the MM subdomain. The edge atoms are hydrogen atoms and the others are carbon atoms.

based on scaling factors calculated for some simple loadings. Under a given strain condition, we calculate ε_1 and ε_2 in the coordinate system 1-2 using the tensor transformations, where 1 and 2 represent the zigzag and armchair edge, respectively. The scaling factor is then calculated by

$$\eta(\varepsilon_1, \varepsilon_2) = \frac{\eta(\varepsilon_1, 0) E^{\mathrm{MM}}(\varepsilon_1, 0) + \eta(0, \varepsilon_2) E^{\mathrm{MM}}(0, \varepsilon_2)}{E^{\mathrm{MM}}(\varepsilon_1, 0) + E^{\mathrm{MM}}(0, \varepsilon_2)}, \tag{A.4}$$

where $E^{\mathrm{MM}}(\varepsilon_1, 0)$ was calculated by applying strain ε_1 and fixing the degrees of freedom in direction 2 for the carbon atoms in all four boundaries and the degrees of freedom in direction 1 for the carbon atoms on the boundaries perpendicular to direction 1 of a pristine graphene sheet. The QM energy of the same sheet under same loading conditions

was calculated and was divided by $E^{\mathrm{MM}}(\varepsilon_1, 0)$ to obtain $\eta(\varepsilon_1, 0)$. In a similar way, $\eta(0, \varepsilon_2)$ and $E^{\mathrm{MM}}(0, \varepsilon_2)$ were calculated.

One advantage of this scaling scheme is that for the uniaxial loadings, where either ε_1 or ε_2 is 0, Eq. (A.4) reduces to Eq. (A.3) exactly.

To illustrate this energy-scaling scheme we consider the fracture of a graphene sheet containing a two-atom vacancy defect. Calculations were performed for a graphene sheet with dimensions of 27 Å $\times$ 21 Å and containing 248 carbon atoms. The edge carbon atoms were passified with hydrogen atoms and a QM subdomain consisting of the 52 atoms surrounding the defect was chosen. The unstrained structure is shown in Fig. A.2.

For this system we considered a strictly QM calculation, a QM/MM calculation with $\eta(\varepsilon)$ calculated using Eq. (A.3) (shown in Fig. A.1), a QM/MM calculation with a constant scaling chosen to exactly match the Young's modulus of the MM and QM methods, i.e., $\eta(\varepsilon) = 1.47$, and a QM/MM calculation where the MM energy is unscaled or $\eta(\varepsilon) = 1.0$. The stress vs. strain behavior for these four calculations is displayed in Fig. A.3.

The QM/MM calculations with $\eta(\varepsilon) = 1.47$ scaling overestimate the stress at all strains. Although this scaling ensures that the Young's moduli of the MM and the QM models match, the stiffness of the MM model is overestimated at higher strains due to non-linearity. Consequently, the QM/MM fracture stress is higher than the QM fracture stress (88.5 GPa versus 80.7 GPa). In a similar way, when no scaling factor is used the fracture stresses are underestimated (72.9 GPa). If instead, constant-scaling factors of

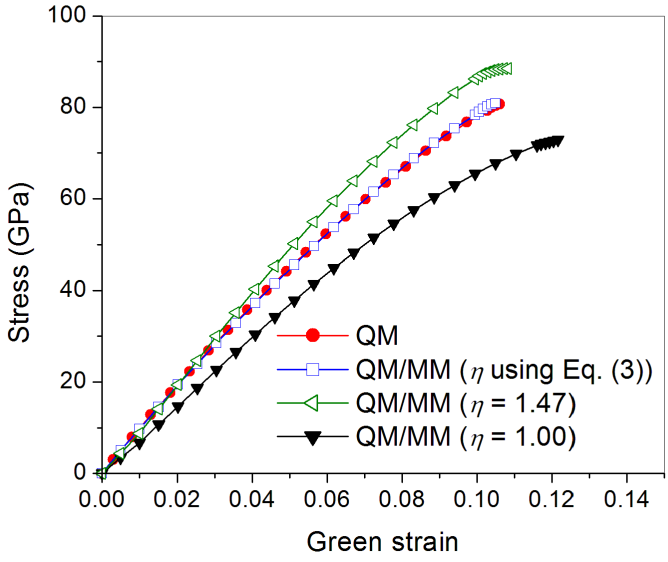

Figure A.3. Stress versus strain curves obtained for the graphene sheet shown in Fig. A.2, strained in a direction perpendicular to the zigzag edge, calculated using the QM method and the QM/MM method using constant and strain-dependent scaling factors

1.20 or 1.60 are used the predicted QM/MM fracture stresses are 79.2 GPa and 93.4 GPa, respectively; thus, the fracture stress depends strongly on the choice of the constant scaling factor.

When the strain-dependent $\eta(\varepsilon)$ is used for the QM/MM calculations the stresses match well with those of the strictly QM calculations over the entire range of strains. Moreover, the fracture stress calculated by the QM/MM method is very close to the QM fracture stress (80.9 GPa versus 80.7 GPa).

Next we used Eq. (A.4) to calculate the scaling factor for a biaxial strain loading such that $\varepsilon_1 = \varepsilon_2$ and calculated energy versus strain curve for the sheet shown in Fig. A.2

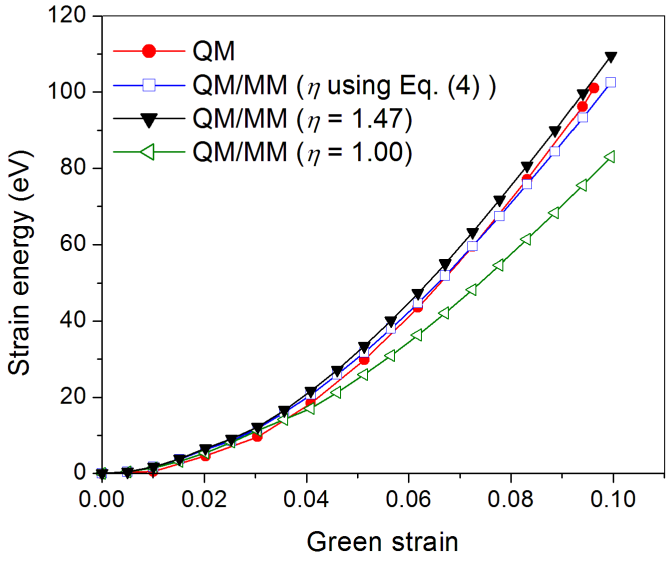

Figure A.4. Energy versus strain curve for graphene sheet shown in Fig. A.2, strained biaxially, calculated using QM/MM and QM methods.

using the QM/MM calculations. These results are compared to strictly QM calculations in Fig. A.4, which shows good agreement between the two energies.

In summary, we have shown that a simple strain-dependent energy-scaling factor obtained from affordable calculations on an undefected sample can be used to significantly improve the consistency of empirical MM potentials with QM interactions over a wide range of strains. Coupled QM/MM calculations using this scaling method show excellent agreement with strictly QM calculations. We also proposed a simple scheme to calculate the scaling factors for any type of loading based on some simple loading conditions which showed good agreement with the QM calculations.